UNIVERSITÀ DEGLI STUDI DI BERGAMO
Facoltà di Ingegneria
Dipartimento di Ingegneria Industriale

DOTTORATO DI RICERCA
IN
TECNOLOGIE PER L'ENERGIA E L'AMBIENTE
XXIII ciclo
anno 2011

SUPERHYDROPHOBICITY AS A STRATEGY AGAINST ICING

Analysis of the water/surface dynamic interaction for icing mitigation

Tesi di dottorato di:
Carlo Antonini

C. Antonini - **Superhydrophobicity as a strategy against icing**

9788897413004

UNIVERSITÀ DEGLI STUDI DI BERGAMO
Facoltà di Ingegneria
Dipartimento di Ingegneria Industriale

DOTTORATO DI RICERCA
IN
TECNOLOGIE PER L'ENERGIA E L'AMBIENTE

XXIII ciclo

anno 2011

SUPERHYDROPHOBICITY AS A STRATEGY AGAINST ICING

Analysis of the water/surface dynamic interaction for icing mitigation

Tesi di Dottorato di:
Carlo Antonini

Supervisori:
Prof. Marco Marengo
Prof. Alidad Amirfazli (University of Alberta)

Blow a soap bubble and observe it.
You may study it all your life...

— Lord Kelvin

Well, I don't really think you have to *work* hard.
I think you have to *play* hard.

— Oliver Smithies, Nobel Laureate in Physiology or Medicine, 2007,
discussing about *Being a scientist.*

Here is the essence of the thesis:
for the last three years I have been playing with drops
(as fascinating as soap bubbles),
and I really hope to go on for a while more.

Abstract

The present thesis is the result of a three year research study, aimed at understanding the potential of superhydrophobicity for combating icing accretion on aircrafts. The project was performed in the framework of a collaboration between University of Bergamo, University of Alberta and Alenia Aermacchi, an Italian aeronautic company.

The thesis illustrates the efforts made to proof how water repellent surfaces can help reducing ice accretion in icing conditions: tests performed in an icing wind tunnel showed that application of superhydrophobic coatings allow considerable savings in supplied heating power, necessary to keep an aerodynamic wing clean from ice, and reduce runback ice, which often forms in unprotected areas.

A considerable part of the work has been devoted to understanding the dynamic interaction between the liquid and the solid surface through single drop impact experiments. Performing drop impact studies allowed explaining the role of different parameters, e.g. impact Weber number and surface wettability, during drop impact on a solid surface and identifying the mechanisms that promote water shedding from the surface. Water drop impact tests performed in isothermal conditions allowed to understand in which conditions surface wettability has an effect on drop dynamics, and also to evaluate characteristic times related to drop impact (e.g. spreading time and rebound time). Water drop impact in freezing conditions, i.e. on surfaces below 0°C, showed that surface temperature does not affect drop dynamics, unless frost is present on the surface.

Contents

Chapter 1

Introduction

> "Strange as it may seem, a very light coating of snow or ice, light enough to be hardly visible, will have a tremendous effect on reducing the performance of a modern aeroplane."
>
> — Jerome "Jerry" F. Lederer, founder of Flight Safety Foundation (FSF) during a lecture on aviation safety (1942).

Icing is defined as the condition when supercooled water drops impact and freeze on a solid structure. Icing can form on a structure when there is visible moisture and a temperature of the surface below freezing.

Ice accretion is a particularly critical event in aeronautics. The presence of ice on unprotected aircraft components can lead to a number of aerodynamic penalties and may even lead to serious safety problems. The most severe penalties encountered by an aircraft are decreased lift, increased drag, decreased stall angle, changes in the pressure distribution, vibrations, early boundary layer transition, and reduced controllability. Test data on ice effects indicate that the presence of ice on an unprotected wing may increase drag by as much as 40% and reduce lift by 30% [1][1]. The en-

---

[1] Ref. [1] is a book, which is available online. Although the book is incomplete, useful information on icing phenomena can be found.

gine damage (bending of fan blades) suffered by an airline in a single icing incident can be as high as 2 million US dollars [2].

Several aircraft accidents from the past have been traced back to icing. Just to cite the most recent tragic events, 50 people died in an aircraft accident (Continental Connection Flight 3407) in the area of Buffalo in February 2009: the aircraft stalled and crashed, after flying in severe icing conditions. In June 2009, Air France Flight 447 from Rio de Janeiro to Paris crashed into the Atlantic Ocean, killing all 216 passengers and 12 crew members. Icing probably caused failure of Pitot tube, leading as a consequence to incorrect speed measurement, automatic speed reduction, stall and aircraft altitude loss.

Therefore, it is of the utmost importance to control or prevent ice formation, especially on the most critical area, such as wind leading edges, control surfaces and engine inlets. Two different philosophy of in-flight ice protection are widely used: **de-icing** and **anti-icing systems**. The de-icing systems work periodically, allowing some small amount of ice to accrete before removing it. The anti-icing systems are designed to completely avoid ice accretion, by continuous functioning from the beginning of any icing event. A de-icing system can be implemented, where a partial deposit of ice can be acceptable, without risks for safety and controllability; on the other hand, anti-icing systems are required in the most critical area, as the wing leading edge, where it is necessary to prevent and avoid impinging water freezing; however, anti-icing systems are more energy consuming because of their continuous functioning. Although it would be sufficient to keep the drop collection areas just above the freezing point to avoid ice accretions on protected areas, most of the anti-icing systems are designed to evaporate a large part of the liquid water caught by wings to avoid liquid runback flow and ice accretion in downstream unprotected areas: this is a well-known phenomenon, called runback ice. The major drawback is that evaporative systems are highly energy demanding: in the case of an evaporative anti-icing system, more than 70% of the energy is used to evaporate water[2].

---

[2] data come from personal communication with anti-icing system designers.

Although currently available techniques for ice removal are generally effective, they require the continuous supply of hot air, chemicals, or electrical power. Little attention has been paid so far to coating strategies, perhaps since such an approach may not be a standalone solution to icing. Nevertheless, the integration of suitable coatings on aerodynamic and structural surfaces can either enhance the effectiveness of standard anti/deicing system requirements, or lead to substantial reduction of the energy consumption of present systems. The present research has been inspired by the idea of following a new strategy: the so called **icing mitigation** strategy. Icing mitigation is a passive techniques which makes use of special properties of some coatings to reduce water and ice adhesion to the surface. In particular, the proposed research work focuses on superhydrophobicity, i.e. extreme water repellency, as a way to promote liquid water shedding from the surface, before water can freeze on it.

In this thesis, we present results and analysis from a three year investigation, aimed at proofing the potentiality of superhydrophobicity as a strategy against icing.

Part I serves as an introduction to the problem of icing. In Chapter 2 a brief overview of the characteristics of icing is provided, with particular attention to aeronautic conditions. Chapter 3 illustrates standard ice protection systems and introduces the concept of icing mitigation, providing details on the state-of-the-art of coating strategies for combating icing.

Part II focuses on water/surface interaction study. After a preparatory chapter (Chapter 4), in which surface wettability is defined and discussed, details of experimental apparatus used for tests and surface preparation is given Chapter 5. Results from drop impact studies are presented in Chapter 6 (drop impacts in isothermal conditions) and Chapter 7 (drop impacts in freezing conditions). Chapter 8 tackles the scaling of results obtained with millimetric drop to micron and sub-millimetric drops.

In Part III the assessment of coating performance in icing conditions is presented. Chapter 9 described the icing wind tunnel facility, test article and test conditions. In Chapter 10 the results are presented and discussed. Finally, conclusions and future perspectives are drawn in 11.

Supplementary material can be found in the Appendices. Appendix A reports FAR related to icing certification. Appendix B includes additional information on the adhesion force of a sessile drop (or bubble) sitting on a surface, due to capillary effects, and describes a methodology for its evaluations. Appendix C describes additional information on high speed drop impacts, performed using a special drop generator developed at Darmstadt University.

Part I

Atmospheric icing: knowledge and technology

Chapter 2

A brief introduction to Aircraft Icing

This chapter is intended to provide the reader a general overview of aircraft icing. In particular, it illustrates the key concepts on icing physics and ice formation mechanisms, aeronautical regulations, numerical modeling and experimental techniques. Most of the information reported here can found, together with additional information, in [1, 3, 4].

2.1 Icing formation mechanism

To understand the origin of ice formation, it is appropriate to mention water particle process in the atmosphere. One of the most important is the condensation of water vapor into liquid. The mass concentration of water vapor may range from near zero in desert regions to as high as 4% in tropical regions. Saturation may occur when water vapor is added to the air or when the air is cooled: when saturation occurs, water condensate, changing its phase from vapor to liquid. This is the typical way, how clouds form.

When temperature in the cloud is below the freezing temperature (i.e.

0°C), water drops may transform into ice crystal by deposition process. In fact, experimental observations show that cloud drops do not freeze until they reach temperatures far below the freezing point. For temperatures within the range −40 to 0°C, drops that stay liquid are called **supercooled drops**. The reason why small drops do not freeze is because their molecules fail to line up in the proper order to form ice crystal. Supercooled drops are is a metastable stable, which means that they may rapidly change from liquid to ice whenever their stability is perturbed, e.g. when drops impact on a solid surface. When temperature approaches -40°C, drops freeze rapidly and transform to ice crystals. The presence of ice crystals alone does not cause icing problems, since they do not stick to cold aircraft surfaces. However, ice crystals should be considered for engines [1].

When atmospheric supercooled drops impact on a structure, two types of ice deposit can be observed (see Figure 2.1):

rime ice is a rough, milky, opaque ice formed by the instantaneous freezing of small, supercooled drops as they strike a solid surface (see Figure 2.1a). Rime ice normally occurs at low temperatures, below −15°C, low liquid water content, LWC, below $0.4 \mathrm{g/m^3}$ (see definition in Section 2.2), and low airspeed.

glaze ice is clear and smooth. Glaze ice results from supercooled drops striking a surface but not freezing rapidly on contact. It is denser, harder, and sometimes more transparent than rime ice. Glaze ice normally occurs at warmer water temperature (between −5 and 0°C) and higher LWC (up to $1.2 \mathrm{g/m^3}$): these factors enhance glaze formation, as they favor slow dissipation of the latent heat of fusion. In glaze icing conditions, water may flow downstream and create ice shapes including “horns”, protruding from unprotected leading edge surfaces (see Figure 2.1b).

For intermediate temperatures, between −15 and −5°C, a mixed ice condition, where both rime and glaze ice coexist, can be observed.

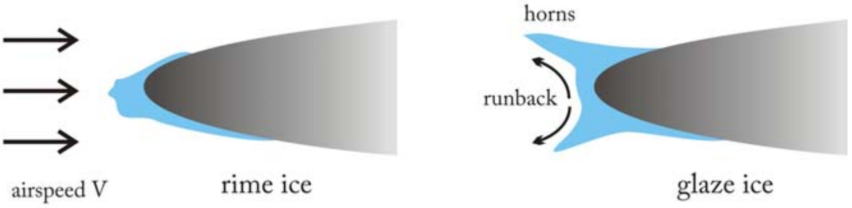

Figure 2.1: Rime and glaze ice accretion (airfoil side view).

2.2 Icing physics and important parameters

The amount and accretion rate of icing depend on a number of meteorological and aerodynamic conditions, such as liquid water content, temperature, drop diameter, collection efficiency, and airspeed. All these parameters have to be taken into account and correctly estimated for the correct modeling and numerical simulation of the process.

Liquid water content is defined as the amount of total mass of liquid water contained in a given unit volume of cloud. For a given drop size distribution, at high LWC a higher number of supercooled drops will impact, i.e. icing is potentially increased. LWC will be higher at temperatures just below freezing and will diminish for lower temperatures, as ice crystals will form at the expenses of liquid drops.

Temperature influences the LWC and the type of ice that will form: rime ice for low temperatures, and glaze ice for temperatures close to zero.

Drop diameter : a distribution of drops diameter has to be given to identify the drop size. The drop size distribution is usually described by a synthetic parameter: the medium volume drop diameter (MVD), defined as the diameter dividing the total water volume in half, where half the volume is in larger drops and half the volume in smaller drops. Note that MVD is an important and useful parameter, but it is in general not sufficient to completely define the cloud: the cloud is completely defined only providing the drop size distribution on the entire spectrum. The drop size influences the icing accretion rate because of the increase of collection efficiency (see below) and the change of the upper and lower impingements limits which move further downstream: smaller drops will likely follow streamlines and have a lower probability to impact the surface, while larger drops will more probably impact. MVD from 10 to 50 μm are common in icing conditions (see [5] and also FAR reported in Appendix A).

Collection efficiency is defined as the ratio of the mass of drops impinging on an obstacle (such as wing or airfoil) in unit time to the mass of drops which would impinges if the drops were following a straight line trajectories. In simpler words, collection efficiency is the percentage of drops on the aircraft path that really impinge on the surface, as they are not deviated by aerodynamic forces. There are two collection efficiencies: a global one, E, and local one, β. The **global collection efficiency**, E, is defined through the equation [1]:

$$\dot{m}_{\text{impinging}} = E \, \text{LWC} \, V A_{\text{front}} \tag{2.1}$$

where $\dot{m}_{\text{impinging}}$ is the water mass flow, impinging on the surface, V is the relative airspeed (see below) and A_{front} is the object frontal area. The *local collection efficiency*, β, is needed in the prediction of ice shapes in numerical methods, as it gives the impinging water mass in each area.

Airspeed : a high airspeed has two effects: the first is an increase of the collection efficiency, due to the streamline modification (more water drops - the big ones - will not have the time to deviate and will impact on the surface); the second is the formation of glaze ice with horns.

A scale of icing intensity allows to classify an icing event as: *a*) trace, *b*) light, *c*) moderate and *d*) severe . This is a general qualitative definition, mainly used by pilots, and depends both on meteorological and operational conditions, but also on the performance of icing protection systems installed on the aircraft. Approximate values of the corresponding LWC (g/m^3) for the different icing events are: *a*) < 0.07, *b*) < 0.5, *c*) < 1.0 and *d*) > 1.0 .

2.2.1 FAA regulation for icing

Certification for aircraft, aircraft engines, or propellers, or an aircraft component must adhere to ice protection regulations, defined by the FAA (Federal Aviation Administration). Transport aircrafts must be able to operate safely in icing conditions indicated in 14 CFR part 25, Appendix C (usually referred to simply as *Appendix C*) to be certificated for flight.

Regulations define continuous and intermittent maximum atmospheric icing conditions, which represent a combination of meteorological icing conditions that may affect aircraft flight. The envelopes are defined on different diagrams as function of LWC, drop mean volume diameter, temperature and pressure. For the reader's convenience, the most significant paragraphs and figures from Appendix C have been reported in Appendix A of this thesis, including regulations specific for engine protection.

Besides regulations, FAA has also created so far a long list of Advisory Circulars (AC), such as AC 20-73A [6]. The AC C 20-73A is not mandatory and does not constitute a regulation. However, it can be a valuable instrument for system designing and how to comply with the ice protection requirements. In particular, it provides guidelines for gaining FAA approval of aircraft ice protection equipments and systems, for determining two-engine airplane airworthiness in icing conditions during extended range operation, and for evaluating aircraft airworthiness following deicing and anti-icing before takeoff.

2.3 Ice accretion model

Numerical simulations represent a powerful tool for prediction of icing accretion and eventual design of systems for protecting structures against icing. Simulation of icing is a complex multidisciplinary problem and several issues are still far from being well represented. However, recent developments of computational fluid dynamics, together with high costs of experimental tests, make make numerical simulations more and more essential for analyzing icing phenomena.

The scheme for ice accretion simulation is generally based on the following steps [1, 5]:

1. flow field calculation;
2. drop trajectory calculation;
3. thermodynamic analysis;
4. ice accretion calculation or anti-/de-icing system design.

The procedure is iterative, as ice deposit grows with time and modifies the geometry of the airfoil continuously, i.e. the flow field streamlines and drop trajectories. As shown in the list above, the last step can be an evaluation of ice deposit shape and accretion rate, used to predict aerodynamic performance degradation, or the design of an ice protection system, to evaluate its performances. Here below a brief description of the different steps.

2.3.1 Flow field calculation

The first step, the flow field calculation, can be performed with a complete Navier-Stokes solver or simpler models (e.g. a panel method). In the first case the calculation may eventually provide not only the streamlines, but also the drop trajectory (output from step 2). Although the Navier-Stokes solver is the most complete solver, it is highly time consuming and adds no accuracy if compared to an inviscid model, coupled with a viscous model for the boundary layer region. Depending on the available computation resources, different flow field solvers may be used.

2.3.2 Drop trajectory calculation

To investigate the drop trajectory, the reference mathematical formulation, which has been widely implemented, was first developed by Langmuir *et*

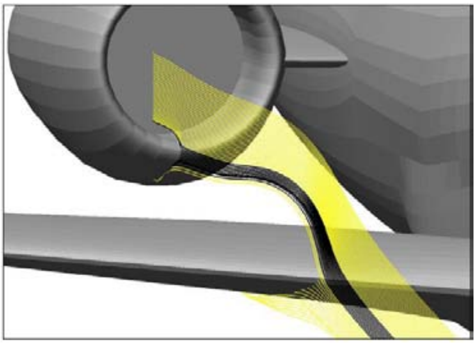

Figure 2.2: Visualization of drop trajectory simulation. Courtesy of Alenia Aermacchi.

al. [7] in 1946. This model uses a lagrangian approach: drops are released upstream of the wing and followed until the impact (see Figure 2.2). The equation of motion takes into account as driving forces drag, buoyancy and gravitational forces. From the experimental point of view, Bragg [8] developed a model for similarity analysis which simplifies the model scaling through the definition of a single scaling factor. Whatever approach is used, the outputs of this step are the local and total collection efficiencies.

2.3.3 Thermodynamic analysis

Different models have been proposed in literature for the thermodynamic analysis of the wing in icing conditions; all models are based on mass and energy conservation, as first proposed by Messinger [9]. Further developments were later proposed, the most important being from MacArthur [10], Al-Khalil *et al.* [5, 11, 12], Louchez *et al.* [13], and Fortin *et al.* [14]. On of the most famous numerical code for icing simulations is LEWICE, developed by NASA Lewis Research Center, first for predicting ice accretion and evaluating anti-icing system and subsequently improved for evaluating anti-icing systems functioning.

When water drops impinge on a cold surface, three different configurations are possible: film, rivulets and beads (see Figure 2.3). In the

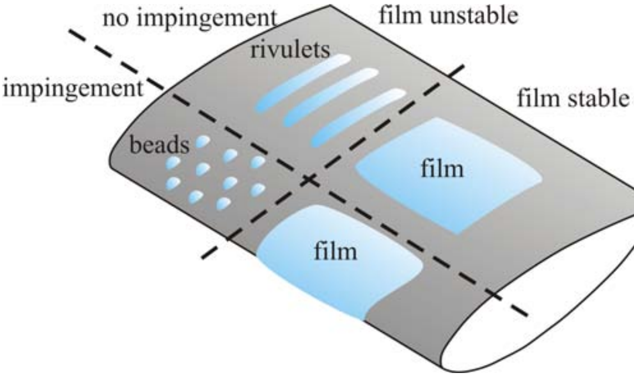

Figure 2.3: Different configurations for liquid water after impingement on an airfoil surface: film, beads, rivulets.

impingement zone, the surface water forms a film when its height is greater than the minimum film height [15], otherwise beads are formed. Outside of the impingement zone, water can form either a film or rivulets, which make the surface wavy and rough.

For rime ice grown at cold temperatures, when heat transfer is high, the impinging water drops freeze on impact, without flowing downstream, and beads are formed. For glaze ice, liquid water does not freeze at the point of impact, but flows downstream due to aerodynamic forces and can freeze away from the impingement zone. If we define a freezing fraction, f, as the fraction of liquid water that freezes upon impact in each area, its value is close to unity in rime ice conditions, whereas it takes a value $0 < f < 1$ in glaze ice conditions.

Rime ice condition is relatively easy to implement, as it is assumed that drops freeze instantaneously and water does not flow downstream (dry-regime, freezing fraction $f = 1$). Glaze ice condition is much more critical, as a correct model for runback flow has to be defined (wet-regime).

Without entering into details, which can be found in the above mentioned references [1, 3, 4], the thermodynamic analysis is based on mass conservation and heat balance. The mass balance takes into account the

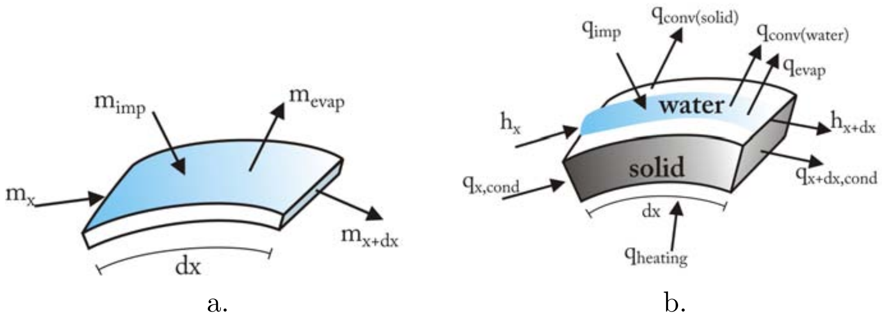

a. b.

Figure 2.4: a. Mass balance on a differential control volume for the runback water; b. energy balance on a differential control volume for the metal skin (wing/inlet surface) and the runback water (from [5]).

mass flow rate of the impinging water, the mass flow rate of water flowing into the control volume (runback water from the previous control volume), the mass flow rate of water flowing out of the control volume (runback water to the next control volume), the mass flow rate due to evaporation or sublimation and the mass flow rate of the freezing water (see Figure 2.4a).

The energy balance (see Figure 2.4b) will take into account the convective heat losses, the enthalpy associated with impinging water and runback water entering the control volume, the enthalpy associated with evaporation or running back to neighboring control volumes and finally the internal energy, calculated in relation to a given reference state depending on the type of surface involved, which depends on the ambient temperature. If a thermal icing protection system is active, heat input is considered, too (see next section). In glaze ice conditions, the surface is almost entirely wet. For rime ice conditions the wing surface is mostly or entirely dry. The procedure is started from the stagnation point, it is repeated for the adjacent downstream control volumes and continued along the entire wing. Good references for further details are [1] and the studies of Al-Khalil *et al.* [5, 11, 12].

2.3.4 Ice accretion calculation or ice protection system design

The thermodynamic analysis allows one to calculate ice accretion at each time step and the updated geometry with the new ice shapes is used as the new input for the flow field solver at the following time step.

In case the functioning of anti-icing system, e.g. a hot-air one, is tested, the contribute of supplied energy has to be considered, too (see Figure 2.4b). Since heat is not directly provided at the external surface but at the internal one, the model has to contain an equation for the solid wall (or more equations are needed if it is made of different layers), as well as appropriate boundary conditions for each interface. Al-Khalil [5] highlighted that heat transfer coefficients are among the most critical parameters for the evaluation of an anti-icing system performance. The need for reliable empirical correlation underlines why experimental campaigns, despite being very expensive, are an essential instrument for anti-icing systems development and evaluation, as they are complementary and so far not totally replaceable by numerical calculations. Nonetheless, efforts are continuously undertaken to extend the validity of ice numerical simulations, with the aim of removing the dependence of models from empirical data (see e.g. [16] for developments of ice roughness models).

2.3.5 The effects of supercooled large drops (SLD)

Aircraft operating outside the FAA certification envelope, described by part 25, Appendix C, may encounter icing conditions, where supercooled large drops (SLD) are present and ice build-up in regions which exceed the active part of ice protection systems. SLD are defined as drops, whose the diameter exceeds $50\mu m$. The effects of SLD have been investigated only recently, in the last decade, and are still under investigation. SLD have a significant effect on impingements limits, collection efficiency and ice shape. On June 2010, FAA has released a notice of proposed rulemaking for addressing supercooled large drop icing conditions, to amend the airworthiness standards applicable to transport category airplanes.

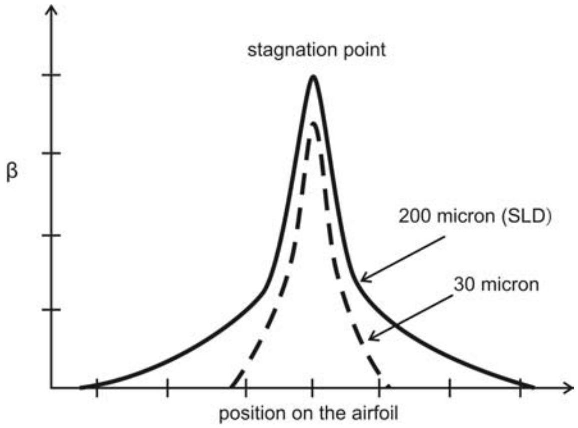

Figure 2.5: Qualitative effect of drop diameter on local collection efficiency distribution, β, along the curvilinear coordinate of an airfoil. Maximum collection efficiency is found at stagnation point.

SLD drops typically form when a vertical air current is present, as drops take more time to fall: as a result, the number of small drops captured is enhanced and drops can grow much more than in still air. From the modeling point of view, SLD simulation differs from smaller drop one, as for large drops the effect of buoyancy may not be neglected and the effect of falling velocity has to be considered.

Results from drop impingement simulations show that for different drop diameters with the same LWC, the impingement limits move downstream with increasing drop size, as shown qualitatively in Figure 2.5. Furthermore, local collection efficiency β increases with drops size, as large drops are more likely to impact on the airfoil while small drops are deviated. The global collection efficiency, E, is increased, too. The consequences is that ice may formed beyond ice protection system, which may make it impossible to melt or shed it, with great risk for flight safety.

2.4 Experimental simulation of icing phenomena

If numerical simulations are a valuable tool for predicting ice accretion and eventually designing systems to avoid ice accretion, experimental tests play a fundamental role for testing numerical results and for the certification process, for which experimental proof of the de- or anti-icing system effectiveness is compulsory. Here we show the most significant scaling parameters, then a brief description of different test options is reported. The interested reader may find a detailed and complete discussion in [17], which is a comprehensive review on both experimental and numerical techniques, where most of the here presented information was found.

2.4.1 Similarity requirements

In rime icing conditions (cold air, low LWC), in which the freezing fraction $f \approx 1$, ice accretion process is relatively simple, because the impacting drops freeze at (or close to) the impact point. For experiments, it is necessary to correctly simulate drop trajectories and to ensure that the temperature of the accreting ice remains below 0℃. Rime ice deposits are relatively simple in shape.

However, when the freezing fraction is less than unity, glaze icing conditions prevail. Glaze icing is much more complex than rime icing because of the unfrozen water, which is present in the impingement zone. As water runs back and freezes downstream, complex shapes develop, often with large horns in two-dimensional cases (see Figure 2.1) and complex three-dimensional “lobster tails” shapes on swept surfaces (with wing sweep angle greater than 15°). In particular, ice accretion is influenced by rivulets behavior.

These considerations suggest that glaze icing condition is a complex phenomenon, in which an important role is played by different parameters, as surface tension, splashing, roughness, aerodynamic pressure forces and shear forces, which depend on the liquid viscosity. Thus, a correct scaling is necessary to reproduce the physics of the problem correctly.

2.4.2 Scaling parameters

A routine dimensional analysis based on Buckingham's theorem leads to the definition of 18 non-dimensional parameters to be considered during icing tests[17]. A substantial number of them are ratios of properties, that are easily matched if full-scale substances, i.e. water and air, are used: indeed, water and air appear to be the only practicable substances to be used in model icing tests.

Kind *et al.* [17] suggest that the following conditions should be satisfied for model tests relating to fixed-wing aircraft flying at incompressible Mach number for *rime icing* cases:

1. **flow-field similarity**, i.e. Re equivalence. Compressibility effects are normally neglected (no need for Ma equivalence), as well as gravity forces (as the Froude number $F = V^2/Lg \approx 100$);

2. **drop scaling-law**. Different models have been proposed in literature, but the most widely used is Bragg's one [8]. According to this model a modified inertia parameter $\overline{K}$ has to be matched, so that:

$$\overline{K}_m = \overline{K}_f \tag{2.2}$$

where the subscript m and f stand for model and full-scale, respectively. The modified inertia parameter is given by:

$$\overline{K} = \frac{K}{Re^{\beta}} \tag{2.3}$$

where β is another parameter to be found graphically as a function of Re (not to be confused with local collection parameter) and K is the traditional inertia parameter (i.e. the ratio of inertial and viscous forces acting on the drop):

$$K = \frac{\rho_D \delta^2 V}{18 c \mu} \tag{2.4}$$

where ρ_D is the water drop density, δ the drop diameter, c the airfoil chord, and μ air viscosity;

3. **accumulation parameter**, which can be regarded as a time-scaling equation and represents the correct scaling of the impinging water volume. Impingement distribution will be correctly scaled if the following relation is satisfied everywhere on the bodies:

$$(\text{impingement volume}/L^3)_m = (\text{impingement volume}/L^3)_f \tag{2.5}$$

that is:

$$\left(\frac{\text{LWC } L^2 V \beta t}{\rho_i L^3}\right)_m = \left(\frac{\text{LWC } L^2 V \beta t}{\rho_i L^3}\right)_f \tag{2.6}$$

As the density of ice, ρ_i, is the same on both sides and assuming that the local collection efficiency β is the same, due to the drop trajectory scaling, the equation can then be simplified to

$$\left(\frac{\text{LWC } V t}{L}\right)_m = \left(\frac{\text{LWC } V t}{L}\right)_f \tag{2.7}$$

One must also ensure that test conditions cause the freezing factor to be unity everywhere, too. In addition to the above listed parameters, for *glaze icing* tests the following conditions apply:

4. match the **"convective/latent heat ratio" B**, defined as:

$$B = \frac{(1 + q_e/q_c) h_c (T_s - T_\infty)}{\text{LWC } V h_{ls}} \tag{2.8}$$

throughout the ice accretion region. The meaning of the variables is: q_e/q_c is the ratio between evaporative loss rate and convective heat transfer rate; h_c is the convective heat transfer coefficient; T_s and

T_∞ are the temperature of the surface and of the ambient air; h_{ls} is the latent heat of fusion. The parameter B is derived from the heat balance equation and has the physical significance of representing the ratio between convective heat loss and latent heat release. $B \approx 1$ would represent the approximate boundary between glaze and rime icing, glaze icing being expected for $B < 1$;

5. if possible, match the **"relative heat factor" b**, defined as:

$$b = \frac{\text{LWC } V \beta c_w}{h_c} \tag{2.9}$$

where c_w is the specific heat of water. This term comes from the heat balance equation, as B, but has a smaller influence than B, to which priority must be given;

6. a set of parameters, as the contact angle for the liquid on the surface, the Weber number and the ratio between viscous forces to surface tension forces, i.e.:

$$\left(\theta, \frac{\rho V^2 D}{\sigma}, \frac{\mu_w V}{\sigma}\right)_m = \left(\theta, \frac{\rho V^2 D}{\sigma}, \frac{\mu_w V}{\sigma}\right)_f \tag{2.10}$$

These requirements represent the correct scaling of surface tension phenomena, so that surface drop and rivulet formation are correctly scaled. In particular, the aim is to simulate the development of the full-scale roughness as closely as possible: indeed, the convection coefficient h_c can be very sensitive to it and it appears that ice accretion in glaze conditions is strongly influenced by roughness effects.

The first three requirements are relatively easy to match, while the other three are difficult to satisfy at reduced scale; as such, scaling of rime ice is easier to perform than glaze ice. Another problem, as underlined by Anderson [18], is that there is no definition of how closely ice shapes need to match to claim successful scaling. In [18], adequate scaling was assumed if scaled shapes agreed with reference shapes within their repeatability. However, in the absence of either a quantitative description or the identification of critical features of ice shapes, assessment of scaling methods will be based on subjective judgment.

2.5 Experimental techniques

Experimental techniques can be divided into three classes:

1. **dry air tests**, where ice shape is simulated artificially using detailed replicas (e.g. made of silicone and epoxy resins). They are aimed at measuring aerodynamic coefficients and determining the characteristics of the flow field, as the formation of laminar separation bubbles. Surface roughness reproduction is the most critical feature;
2. **two-phase flow tests** are used to study water drop trajectories, local impingement distributions, drop splashing, surface run back water, thermal effects, etc., and include the presence of the liquid film that is deposited on the surface. The temperatures are above the freezing point, since the experiments are aimed at understanding the role played by liquid water and are mainly applicable to glaze ice accretion cases;
3. **complete simulations** aim at complete similarity of all existing physical phenomena, maintaining air temperature below freezing and including clouds of supercooled drops. Two subgroups can be identified: the first has the main objective of translating results to full scale; the second subgroup is more research oriented and the test measurements, for various input variables, are the desired result.

From the facility point of view, a second classification is possible:

A. **Ground-based techniques**, i.e. wind tunnels or icing wind tunnel (IWT). Two examples are NASA's Icing Research Tunnel (IRT) and CIRA (Italian Center for Aerospace Research) IWT.

B. **In-flight test techniques**, either in natural or artificially reproduced icing conditions, by use of water spray tankers.

If certification for flight in icing conditions is desired, the airworthiness regulations require tests in natural icing conditions to demonstrate that the aircraft is able to operate safely in all operational conditions within the FAR icing envelopes. However, in-flight tests are expensive and an improvement of the correlation between numerical simulations and icing tests results is highly desirable, as it would significantly reduce dependence on flying aircraft in natural icing conditions and would thus reduce the cost of aircraft certification.

Chapter 3

Ice protection strategies

3.1 Introduction

In the development of ice protection systems for aeronautics, but also wind turbines or telecommunication antennas, traditional strategies are represented by de-icing and anti-icing systems. In the present chapter, an overview on state-of-the-art ice protection systems is proposed. Some traditional strategies will be presented.

The concept of icing mitigation, a protection strategy based on application of special coatings, will be introduced. Attention will be also given to the attempts made in development and application of special coatings as alternative or complementary approach for reducing ice accretion.

Additional information on ice protection systems can be found in [19].

3.2 Need for ice protection systems

Aircrafts may encounter atmospheric conditions that cause the ice formation during flight or while on the ground. Ice can accrete on wings and on other surfaces, e.g. stabilizers, rudder, ailerons, engine inlets, propellers, rotors, and fuselage. Accumulated ice, if not removed, can al-

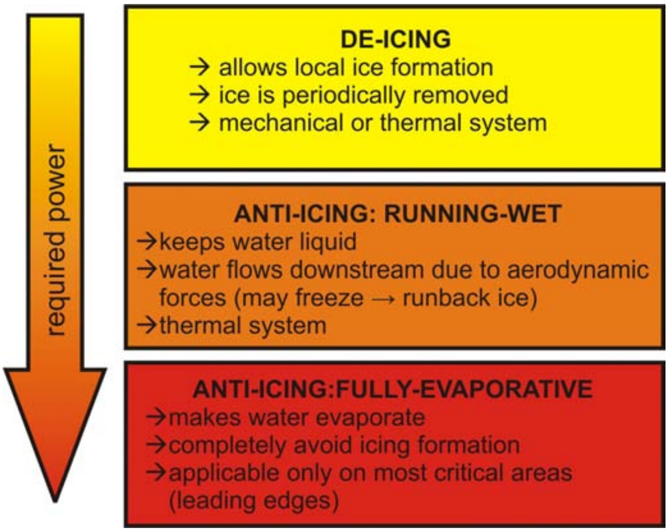

Figure 3.1: Characteristics of principal ice protection systems, ordered by increasing required power.

ter the aircraft aerodynamics, causing undesirable and/or dangerous flying conditions. However, available ice protections systems have usually been reserved for large aircraft because expense and added weight have made them impractical for general aviation single engine and light twin airplanes and helicopters.

Several approaches have been developed so far to provide ice protection systems of modern aircrafts, either anti-icing or de-icing systems. Mechanical, chemical or thermal are typical examples of active ice protection systems.

3.3 De-Icing systems

De-icing systems work periodically, waiting for some small amount of ice to accrete before removing it (see Figure 3.1). A de-icing system can be implemented, where a partial deposit of ice can be acceptable without risks

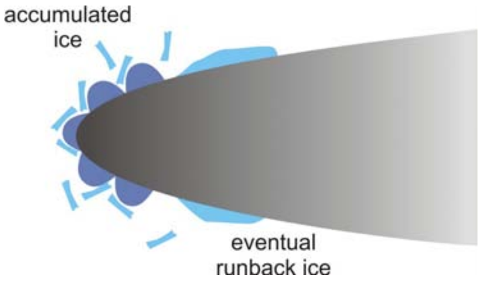

Figure 3.2: Example of de-icing system: pneumatic boots.

for safety and controllability. One commonly used system for de-icing is the mechanical removal of ice with pneumatic boots (see Figure 3.2). In this system, the leading edge zone of wing or aircraft component is covered with a plurality of expandable boots that are inflatable with a pressurized fluid, such as air. When inflated, the boots expand and crack the accumulated ice which is then dispersed into the air stream. A drawback of pneumatic boots is that, if ice forms where boots are not installed, not all the ice can be removed. Although pneumatic boots have been used on commercial aircraft and some light twin or small jet aircraft, the system, which requires an air compressor and vacuum system, is expensive and adds appreciable weight to light aircraft.

Another mechanical system for removing ice is the electro-impulse de-icing system. Flat-wound coils inside the leading edge induce eddy currents in the metal skin, resulting in a deformation of skin and ice layers.

A more recent de-icing solution is represented by Shape Memory Alloys (SMA), based on NiTi-alloys, which exhibit a large temperature induced dimensional change over a relatively narrow temperature range. Suppling heat to the material induces a shape change, which creates an ice breaking action.

3.4 Anti-Icing systems

Anti-icing systems are icing protection systems designed to avoid ice accretion on the structure. The functioning of such systems is continuous, from the start of any icing event. Anti-icing systems can be divided into two groups: *running wet* and *fully evaporative* (see Figure 3.1). Running wet systems keep water liquid in the protected areas; liquid water is generally removed by aerodynamic forces, which make the liquid flow downstream; the main limitation running wet systems is that liquid may freeze downstream in the unprotected areas, forming the so called runback ice. For this reason, many systems in the most critical areas have to be designed as fully evaporative, making water evaporate to avoid potential icing formation even in unprotected areas. Fully evaporative system are high energy demanding (more than 70% of the energy is used to evaporate the water) and are thus applicable only in the most critical areas, e.g. leading edges.

The typical anti-icing system is a thermal system which supply heat to the area that needs to be protected. One such system, limited to aircraft with jet engine, diverts hot air from one of the compressor stages to heat leading edges of wings or inlets. Figure 3.3 schematically illustrates the functioning of a hot air system using a so called **piccolo tube**, which distributes hot air in the inner side of a wing leading edge. Figure 3.3 also shows an additional source of inefficiency for anti-icing systems: the formation of rivulets. In the impingement zone, all heat is provided to the liquid, which wets the surface as a film. Outside the impingement zone, water only partially wets the surface and most of the heat is wasted heating up air, rather than water.

Other thermal systems employ electrically conducting resistances as heating elements; an example are heating pads bonded to the leading edges of the aircraft or on the propeller or rotor blades, or those incorporated into the structural members of the aircraft. Heating pads of this type usually consist of an electrically conductive material in contact with wire or other metal heating elements dispersed throughout the conductive layer, which is sandwiched between two layers of insulation. Electrical energy for the heating elements is derived from a generating source driven by one or more

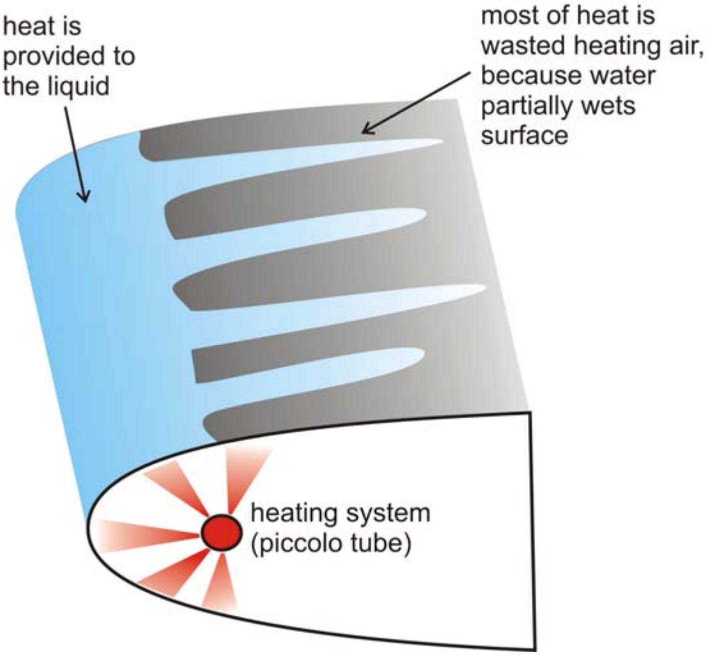

Figure 3.3: Example of anti-icing system with piccolo tube. Heating of the leading edge is provided by a hot air system. In the drop impingement zone heat is provided to water; if rivulets form, most of heat is wasted heating up air, instead of the liquid.

of the aircraft engines.

Another common approach involves the application of a chemical, such as alcohol, to reduce adhesion forces associated with ice accumulation and/-or depress the freezing point of water collecting on the surfaces. Such systems may be used while the aircraft is on the ground or in flight. Drawbacks of such on-board chemical systems include their cost and the necessity to rely on a finite supply of the chemical during flight.

3.5 Icing mitigation

Although currently available techniques for ice removal are generally effective, they require the continuous supply of hot air, chemicals, or electrical power. Little attention, however, has been paid to coating strategies, perhaps since such an approach cannot be a standalone solution to the icing.

Two approaches related to coating strategies can be found in the literature. Most of the studies concentrate on the so-called *icephobic coatings* [20, 21, 22], on which ice adhesion is low. Use of such coatings can help reducing the shear forces needed to remove the ice from a structure. According to this line of work, a small amount of ice is allowed to form on the surface; subsequently ice can be shed, taking advantage of external forces, such as gravity or aerodynamic forces, to overcome ice-surface adhesion forces. An alternative approach, which is proposed in the present study, focuses on *superhydrophobic coatings*, i.e. water repellent surfaces, on which liquid water adhesion is low. The idea of using superhydrophobic coatings is to take advantage of water-repellency and low adhesion of drops in liquid state to such coatings, in order to reduce or to eliminate water accumulation on the surface before water freezes. Indeed, some material with superhydrophobic characteristics may also show weak ice-adhesion [21], and thus have an additional benefit. In literature to date, however, no particular distinction between two strategies (i.e. 1-application of icephobic coatings, and 2-application of superhydrophobic coatings) has been made. Some recent studies [23, 24] have presented qualitative results to prove the effectiveness of different coatings in icing conditions [23] and with supercooled liquid water flow [24]. However, the mechanism of water/surface interaction in icing conditions has not been clearly investigated yet and thus has been addressed in the present study.

One of the earliest studies on ice adhesion, designed for potential aeronautical applications, was performed by Loughborough and Haas [25] in 1946. Adhesion of ice to metals and polymers was studied. The first study on icephobic coatings was performed by the U.S. Navy in the sixties [26, 27]. A survey of literature showed that in the 60's there were no coatings available which were effective over extended periods of time [26]. On the basis of the ice adhesion strength of the various coatings, in [27] it was concluded that the potential of coatings did not appear to be sufficient to warrant further research then. The interested reader can see [28] for a more complete list of references for ice-adhesion tests for applications in different fields.

The interest in low ice-adhesion coatings were resumed in recent years [20] (1997). The studies in [20] were preliminary and involved simple qualitative evaluations of the ease of removing impact ice (i.e. ice formed after impact of liquid water drops on a surface) from various surfaces. Also, in [20] methods to estimate ice adhesion force on coated and uncoated surfaces subjected to atmospheric icing were examined. Results from icing wind tunnel tests showed that *ice accretion were dependent solely on tunnel and cloud conditions, and not on the surface on which the ice accreted.* It was shown that, as soon as a thin layer of ice formed on the surface, coating was no longer effective, since impacting drops accumulated on an already iced surface. Furthermore, static ice-shear tests confirmed that tested coatings did not provide substantial reduction of ice adhesion in order to promote ice shedding, compared to uncoated aluminum samples.

More recent tests were performed by Laforte *et al.* [21] to determine experimentally the adhesion reduction of seven icephobic coatings. From their observations on unheated surfaces, it was concluded that the presence of an icephobic coating under simulated icing conditions at an intensity rate of 6 mm/hr did not reduce the amount of ice accumulated on a surface. Secondly, among the seven icephobic coatings studied, the most efficient coating was found to be a compacted powder, which reduced adhesion by 37% compared to uncoated aluminum. This performance was proved not to be sufficient to allow for natural ice release through the effects of gravity and/or wind. Moreover, the icephobic coating was not deemed to be a permanent solution, because of the gradual degradation of the surface caused by successive de-icing operations. The study concluded that icephobic coatings may not be used as a stand alone technique to solve the icing problem.

Studies in [29] were performed with the aim of finding a coating material that would reduce ice formation and/or ice adhesion to the substrate materials at cryogenic temperatures (-112℃), characteristic of the brackets that secure the liquid oxygen feed line to the external tank on the NASA space shuttle. The strategy was still based on identification of an icephobic coating with low ice-adhesion. Several formulations of a coating, the SILC (Shuttle Ice Liberation Coating), were tested to evaluate the ice adhesion in [29]. Coatings used for tests were different combinations of binder, such as Braycote and Rain-X®, together with fillers, such as MP-55 and UF-8TA, with varying filler/binder proportion. Contact angles (i.e. the angle a sessile drop forms when placed on a surface - see Chapter 4 for definitions and details) ranged from 81° to 143° for the surfaces used. Static ice-shear tests identified that the coating made of a mixture of Rain-X and MP-55 results in low ice adhesion, when compared to bare metals. However, it was not clear whether this reduction was sufficient to promote ice shedding from surfaces in operating conditions (e.g., taking advantage of aerodynamic drag forces).

In 2007 Kimura et al. [23] tested a coating for prevention of icing on airfoils, named Advanced Icephobic Surface (AIS). The AIS is a mixture of urethane and PTFE (polytetrafluoroethylene) particles. The coating is reported to be water repellent (contact angle 150°), transparent (though it has a mild cream color) and characterized by hardness 2H (pencil hardness). Tests were performed on two airfoils in an icing wind tunnel (IWT): one airfoil was coated with AIS, the other airfoil was coated with polyurethane. An electrical heater was inserted in the airfoils to simulate an anti-icing system. Results were the following: (i) when heater was kept off, no significant difference between the AIS coated and the polyurethane coated airfoils was present; both samples showed a similar ice accumulation; (ii) when the heater was activated, it was observed that, *in the same icing conditions, less ice accumulated on AIS coated airfoil compared to the polyurethane coated airfoil*; (iii) the effect of AIS coating was even more evident in glaze icing conditions, since runback ice observed on the polyurethane coated airfoil was not seen on the AIS coated airfoil. However, in this work a mechanistic explanation for coating effectiveness was missing: it was not clear whether the icing reduction should be explained by means of coating icephobic properties (as the name of the coating, AIS, suggests) or because of superhydrophobicity (as the contact angle suggests) or both. Also no clear criteria was given to objectively compare results for differently coated airfoils, e.g. the required power to keep the area close to the leading edge free from ice. Such a criterion is necessary to quantitatively evaluate the benefit of surface coating in terms of energy consumption.

In 2009, Cao *et al.* [24] reported qualitative tests in which supercooled liquid water was manually poured on inclined plates with different wettabilities (contact angles in the range $143° < \theta < 158°$). It was shown that *water freezes very close to the impact point on untreated aluminum, whereas on a superhydrophobic surface water flows downhill after impact and freezes at the bottom of the plate.* A theory was also proposed to relate length scale of hydrophobic particles, present in the coating, and the probability to see ice formation. Results from this study highlights that wettability can affect the icing of a surface, but further studies have to be performed in realistic and controlled icing conditions, in order to quantitatively estimate the effectiveness of superhydrophobic surfaces.

Studies on ice/hydrophobic surfaces have also been investigated for a variety of applications, aside from aeronautics, such as power lines and antennas. In 1998 Laforte *et al.* [30] reviewed various techniques for combating icing on power lines. *Ice adhesion force on tested icephobic coatings remained 20 to 40 greater than the available aerodynamic or gravity forces.* It is mentioned that hydrophobic substances can provide limited effectiveness and worked only in wet snow conditions. In 2001 Nakajima *et al.* [31] reported that application of superhydrophobic films was successful in reducing the disruption of communication by the adherence of snow to an antenna. This results showed that hydrophobic coating can be a useful standalone passive technique in wet snow conditions. Once again, results are only qualitative and are not provided together with a mechanistic explanation of the coating effectiveness.

Kraj and Bibeau [32] performed some preliminary tests on airfoils coated with hydrophobic and icephobic coatings in an IWT. The objective of tests was to evaluate the ice adhesion force and ice accumulation using different strategies. As a general trend, it was qualitatively observed that *hydrophobic coating can be more effective in glaze icing conditions, whereas the icephobic coatings can be more effective in rime ice conditions.* No details were given as how hydrophobicity and icephobicity were defined. Differences of ice formation on the airfoil were generically attributed to the physical properties of the coatings: however, a clear distinction between different icing mitigation strategies was not provided; neither quantitative measures of coating effects nor detailed explanations for the observed phenomena were provided. As such, general conclusions for the conditions to use low-adhesion coatings was not given, nor the working principle identified.

Some outdoor tests were also performed in [33], where wind turbine blades were coated with a black colored hydrophobic coating, StaClean™, to combine the effect of water repellency and of heating by solar radiation. It was reported that the StaClean coating was qualitatively effective in light icing condition, whereas in severe icing condition the only option to protect blades was to use a blade heating system. No technical data were available for such tests and hence it is not possible to quantify how much the coating was effective, e.g. in terms of decreased ice accretion, and which physical mechanisms made the coating effective.

In summary, *in the literature there are evidences that low adhesion coatings may be effective in mitigating icing. However, results are mostly only qualitative, not indicating a clear trend, and different coatings are shown to be useful only for limited icing conditions.* Furthermore, no explanation on the physics of ice accumulation for the low adhesion coatings has been provided yet. As such, a physical understanding of the phenomena is lacking in regards to the different mitigation strategies. Most of the works [22, 23, 26, 27, 29] generally try to attribute ice accretion reduction to low ice adhesion. However, some studies [21, 30] pointed out that, even if ice adhesion can be reduced by icephobic coatings, compared to metal surfaces, such reduction is not sufficient to shed ice by means of an external force, e.g. gravity or aerodynamic forces. Hydrophobicity is also often evoked to explain the working principle of icing mitigation, providing a correlation between contact angles and the strength of ice adhesion. Nevertheless, no quantitative correlation has been proposed between hydrophobicity and ice accretion, thus far. Also, only the value of static contact angle is normally reported to define surface wettability, and the contact angle hysteresis, that is an important parameter to determine liquid shedding from a coating (see next Chapter) is often neglected.

Part II

Basic research: Water/surface interaction

Chapter 4

Understanding wettability

The control of surface wettability is a key element of a coating strategy for icing mitigation. In the present chapter, the physics of liquid/surface interaction is explained and critically discussed, on the basis of the literature up-to-date. Particular attention is paid to water as liquid, due to the interest in icing applications. In particular, attention is focused on the two classical approaches for investigating the physics of liquid/surface interaction: a static (or quasi-static) approach, using sessile drop, and a dynamic approach, by means of drop impact studies.

4.1 Sessile drop on a solid surface

4.1.1 Contact angle(s) to measure wettability

The wettability of a solid surface can be described by observing the shape of a liquid (in the present case, water) drop deposited on the surface (water drop in the present study). A surface having a high wettability (hydrophilic) tends to allow the drop to spread over a relatively wide area of the surface, thereby wetting the surface (see Figure 4.1a). This is the case of the hydrophilic surfaces. For a surface with low wettability (hydropho-

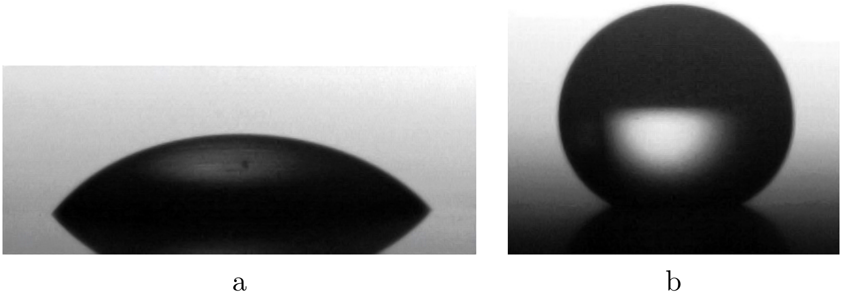

Figure 4.1: Sessile water drop on a hydrophilic surface (a) and a superhydrophobic surface (b). Drops have the same volume, equal to 11.5µl (corresponding to a spherical drop with diameter 2.8mm).

bic), the liquid tends to retain a spherical shape (see Figure see Figure 4.1b) and drops can usually shed from the surface with a slight disturbance, e.g. surface vibration or by tilting the surface (especially for a SHS, SuperHydrophobic Surface) [34].

The typical parameter used to characterize a solid surface wettability is the contact angle, which is the angle formed between the liquid/solid and the liquid/vapor interface (see Figure 4.2). A basic relation for the contact angle, attributed to Young (see his pioneering study [35]), can be derived by balancing surface tensions, σ_{ij}, acting at each ij interface (liquid/vapor, liquid/solid, and vapor/solid):

$$\cos\theta_{eq} = \frac{\sigma_{SV} - \sigma_{SL}}{\sigma_{LV}} \tag{4.1}$$

where θ_{eq} is the *equilibrium* contact angle, and subscripts indicate the corresponding interfaces (note that liquid/vapor surface tension is equivalently indicated in literature as σ_{LV} or simply as σ). The drop shape can be approximated as a truncated sphere [34], if the drop size is smaller than the capillary length:

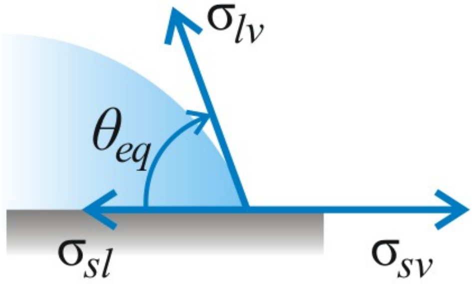

Figure 4.2: Surface tension balance at the triple line, where solid, liquid and vapor meet, determines the value of the contact angle, as prescribed by Equation 4.1.

$$l_{cap} = (\sigma/\rho g)^{1/2} \approx 2.7mm \quad \text{[for water]} \tag{4.2}$$

where ρ is water density, and g is acceleration due to gravity. If the assumption of truncated sphere holds, the radius, R, of the circular contact area between water and the solid is a function of the drop volume, V, and of the contact angle, θ [34]:

$$R = 4^{1/3} \frac{\sin\theta}{(2+\cos\theta)^{1/3}(1-\cos\theta)^{2/3}} R_0 \tag{4.3}$$

where R_0 is the radius of a spherical drop with the same volume, V, as the truncated sphere (i.e. $V = 4/3\pi R_0^3$). The contact area tends to infinity for $\theta \to 0°$ (perfectly wettable surface), i.e. a film forms, whereas contact area vanishes as $\theta \to 180°$ (perfectly non-wettable surface).

Equation (4.1), often referred to as Young equation, is only valid for a sessile drop placed on an ideal, homogeneous and smooth surface. When a surface is rough, two wetting states, Wenzel state [36] and Cassie-Baxter state [37], can be observed. In the Wenzel state, the liquid penetrates the surface grooves and wets the surface completely (see Figure 4.3b). The contact angle observed in this condition is given by Wenzel's equation [36]:

$$\cos\theta^{W} = r\cos\theta_{eq} \tag{4.4}$$

where the roughness factor, r (with $r > 1$), is the ratio between surface area of the solid, in contact with the liquid, and its horizontal projection. In the Cassie-Baxter state, the liquid bridges across the tops of surface features (see Figure 4.3c); the drop sits upon a composite surface of solid and vapor pockets. The contact angle is given by:

$$\cos\theta^{CB} = f_S\cos\theta_{eq} - (1 - f_S) \tag{4.5}$$

where f (with $f < 1$) is the fraction of the area, where the liquid is in direct contact with the surface; $1 - f$ is the fraction of the area, where liquid is in contact with vapor pockets. A combined state, in which liquid partially penetrates surface grooves, is also possible (see Figure 4.3d).

Equation 4.5 is useful to understand how a superhydrophobic state can be achieved. Firstly, the coating material should be intrinsically water repellent, i.e. showing a contact angle higher than 90° on a smooth surface; however, it is known that the contact angle on a flat smooth surface cannot exceed 120° [34]. To further increase the contact angle, the surface must have suitable roughness: for example, if the smooth surface has a contact angle $\theta_{eq} = 110°$, a Cassie-Baxter state with $\theta^{CB} = 150°$ can be achieved if $\varphi_s \approx 0.20$. Typical range of surface roughness structure is from microns down to tens of nanometers.

Cassie-Baxter and Wenzel equations are a simple and useful equations to predict mainly the equilibrium contact angle on a rough surface. However, surfaces can present both physical and chemical heterogeneities (e.g. roughness is normally randomly distributed on a surface). As such, when a drop is placed on a surface, not only a single value, but multiple values of the contact angle can be observed: this phenomenon is referred to as contact angle hysteresis, $\Delta\theta$. Contact angle hysteresis is usually quantified as the difference between the advancing and receding contact angles, θ_A and θ_R, which are measured for an expanding and withdrawing drop, respectively, on a level surface through a quasi-static measurement [38]. Thus, due to experimental difficulties in measuring the equilibrium contact angle

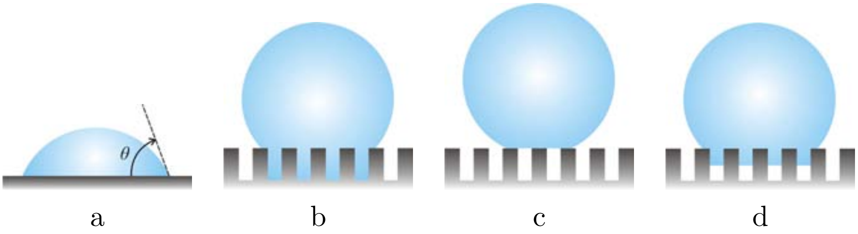

Figure 4.3: Schematic of wetting states of a sessile drop placed on a surface: a. drop on a smooth surface (measure of the contact angle is illustrated); b. Wenzel state, c. Cassie-Baxter state, d. combined state.

(which is only one of the possible values of θ that can be observed for a sessile drop), it is preferable to characterize a surface reporting the range of observable contact angles, providing two parameters, e.g. θ_A and $\Delta\theta$ (or, equivalently, θ_A and θ_R). The necessity to provide the range value for the contact angles, rather than a single value, has been recently stressed by Gao and McCarthy in [39], in a paper containing a deliberately provocative statement in the title: “Teflon is hydrophilic”.

To sum up, information on contact angle are fundamental to predict drop interaction with the solid surface: the equilibrium (or alternatively advancing) contact angle is a measure of surface *repellency*, whereas contact angle hysteresis is a measure of drop *mobility* [38]. The drop/surface adhesion force is controlled by surface tension and drop shape. In the past low adhesion (i.e. high mobility) was often associated with repellency, and surfaces were categorized using only the equilibrium/advancing contact angle as hydrophilic ($\theta < 90°$), hydrophobic ($90° < \theta < 150°$) or superhydrophobic ($\theta > 150°$). Presently, a surface is usually labeled superhydrophobic when θ is high (larger than 150°) and $\Delta\theta$ is low (less than 10°).

With respect to drop shedding, recent studies on shedding by gravity on tilted surfaces [38] and by airflow [40] have pointed that for such cases the traditional definition of $\Delta\theta$ is not suitable, and the difference ($\theta_{\max} - \theta_{\min}$) should be used instead; the maximum contact angle, $\theta_{\max}$, is the angle observed downhill/downstream, and minimum contact angle, $\theta_{\min}$, is the angle observed uphill/upstream, for the cases of gravity/airflow shedding, respectively.

In Appendix B we report the results, published in [41], from a general methodology for evaluating the adhesion force between a drop and a solid surface. The correct formulation for evaluating the adhesion force is proposed, together with a methodology for reconstructing the drop shape and thus adhesion force from drop multiple images. Correct evaluation of adhesion force is a necessary step for developing new models that can predict the value of the adhesion force for any generic liquid/surface system and thus indicate in which conditions drop shedding from a surface may occur.

4.2 Background of drop impact studies

Drop impact studies are a useful tool for studying the dynamic interaction of a liquid during an impact with a surface, which can be either liquid or solid. Understanding the governing physics of drop impacts is not only a challenging multiphysics problems, but is also important for a myriad of engineering applications, where sprays (which consists of dispersed drops) are involved: some typical examples, beyond icing, are internal combustion engines [42], spray paint technology, pesticide application [43] and drug coating for medical applications.

With respect to drop impact studies, a wide number of works in literature is dedicated to the investigation of single and multiple drop impact on solid surfaces (see [44] for a comprehensive review). Majority of studies, either experimental [45, 46, 47], numerical [48, 49] or theoretical [50, 51], mainly refer to surfaces with high wettability (referred to as hydrophilic, when liquid is water), for which the contact angle (CA or θ) at the three phase line is lower than 90°. Only a small part of studies investigates contact angles higher than 120° [52, 53, 54, 55, 56, 57].

The following sections provide an introduction to the physics of drop impact, with a particular stress on the importance of surface wettability.

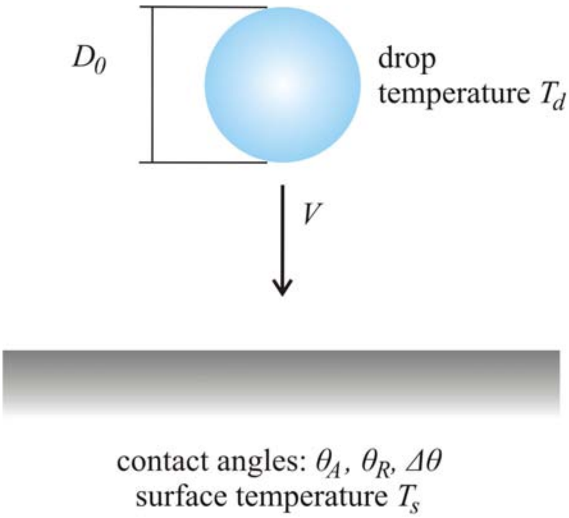

Figure 4.4: Physical parameters involved in a drop impact on a solid surface.

4.2.1 Fluid dynamics non-dimensional numbers

First of all, it is necessary to define the characteristic non-dimensional numbers, typical of drop impact phenomena (see Figure 4.4). The three most commonly used non-dimensional numbers are: the Weber number, We, the Ohnesorge number, Oh, and the Reynolds number, Re. The Weber number is defined as:

$$We = \frac{\rho V^2 D_0}{\sigma} \tag{4.6}$$

where ρ is the fluid density, V the impact speed, D_0 the diameter of the spherical drop before impact (or an equivalent length for a non-spherical drop). The Weber number can be interpreted as the ratio between inertial forces and capillary forces, which act at the drop interface. The Ohnesorge number is defined as:

Table 4.1: Water properties of interest for drop impact studies at 20°C and 0°C and ice properties at 0°C. Thermal effusivity defined in Equation 4.22.

	water		ice
property	$T = 20$°C	$T = 0$°C	$T = 0$°C
density ρ [kg/m^3]	998	1000	917
surface tension σ [N/m]	73×10^{-3}	76×10^{-3}	-
dynamic viscosity μ[Pa s]	1.00×10^{-3}	1.79×10^{-3}	-
thermal conductivity k[W/mK]	0.58		2.18
specific heat capacity c [J/kgK]	4183	4210	2108
thermal effusivity [Ws$^{0.5}$/m^{2}K]	1556	1562	2053
latent heat [kJ/kg]	-	314	

$$Oh = \frac{\mu}{\sqrt{\rho \sigma D_0}} \tag{4.7}$$

where μ is the dynamic viscosity of the liquid. The Ohnesorge relates viscous forces (numerator) to capillary forces (denominator). Finally, Reynolds number relates inertial to viscous forces and is defined as:

$$Re = \frac{\rho V D_0}{\mu} \tag{4.8}$$

The three parameters are not mutually independent; the relationship between them is:

$$Re = \frac{\sqrt{We}}{Oh} \tag{4.9}$$

For drop impact studies the couple (We, Oh) is typically used for convenience, because Oh does not depend on impact speed, V. However, some authors prefer to express results in terms of (We, Re) or (Oh, Re). All the approach are of course equivalent.

4.2.2 Wettability in drop impact studies

Wettability is an important parameter that influences the interaction between a surface and an impacting drop. The influence of wettability was first highlighted in [58], in which it was shown the role of wettability in achieving drop rebound after impact of water drops onto leaves. The authors [58] proposed an energy balance approach for the spreading lamella in which they accounted for wettability through the value of a static contact angle. A phenomenological approach to drop impact on SHS was recently given in [57]. Four different outcomes were identified: deposition, rebound, sticking or fragmentation. Accordingly, a drop impact regime map was proposed [57]. It was observed that, for the analyzed impacts (water drops on superhydrophobic polypropylene surface), the transition from rebound to fragmentation was governed by Weber number (being the limit $We = 60$). For the deposition-rebound limit, it was observed that this also depends on a critical We number, but this is no more constant. It was proposed that critical Weber can be expressed as a function of two parameters: the average contact angle, defined as the average between advancing, θ_A, and receding, θ_R, contact angles, and the contact angle hysteresis, $\Delta\theta$ (see previous section for contact angle definitions).

Drop rebound time (i.e. time between impact and rebound instants) on SHS was studied by Quéré and co-workers [53, 54, 56]. It was found that, in the investigated We range ($0.3 < We < 37$ in [53]), drop rebound time on a SHS does not depend on impact speed, but only scales with drop mass, m: drop rebound time was found to be proportional to $m^{1/2}$ (or equivalently $D_0^{3/2}$, where D_0 is the drop diameter of the impacting drop). The proposed equation for drop rebound time is [53]:

$$t_{rebound} = 2.65 \left(\frac{\rho D_0^3}{8\sigma} \right)^{1/2} \tag{4.10}$$

Bartolo *et al.* [55] focused on the retraction dynamics of water drops on Parafilm®, which has a receding contact angle equal to 80° (as such, coating is weakly hydrophobic). They identified two different regimes (capillary-inertial and capillary-viscous) for drop retraction dynamics. Threshold between two regimes was found to be $Oh = 0.02$ for the specific tested surface. Li *et al.* [59] investigated the effect of surface texturing on the receding phase and thus drop contact time. Tests performed on textured silicon surfaces decorated by square arrays of pillars with different geometries showed that surface texture has a direct effect on receding contact angle and thus modifies retraction dynamics and, in case of rebound, drop rebound time.

4.2.3 Maximum spreading of an impacting drop

One of the most important parameters used to describe drop impact on a surface is the drop maximum spreading, expressed by a non-dimensional number, i.e. the maximum spread factor, $\xi_{max} = D_{max}/D_0$ (ratio between the contact diameter at maximum spreading, D_{max}, and drop diameter before impact, D_0). Many correlations have been proposed in literature to estimate ξ_{max}: in the present study we discuss the most widely used [45, 51, 52, 54, 60] and compare them with our experimental results. Also, 1D analytical models have been developed to provide time evolution of spread factor $\xi(t) = D(t)/D_0$, where $D(t)$ is the diameter at the liquid-surface interface, as function of time, t. Among the several analytical models in literature, three of them [61, 62, 63] have been tested against experimental results in the present study.

In a recent review [64], we classified and compared most common correlations and models used to predict drop spreading. In the present section we briefly discuss them; the more interested reader can eventually refer to [64] for a more complete discussion.

Two of the five correlations for ξ_{max} [45, 51] were formulated investigating drop impacts on hydrophilic surfaces, using water as liquid, and glass or metal as impact surfaces. One is the correlation proposed by Scheller and Bousfield [45] is:

$$\xi_{max} = 0.61(We/Oh)^{0.166} \tag{4.11}$$

and the second, a more recent semi-empirical correlation by Roisman [51], based on a combination of theoretical results and experimental data fitting, is:

$$\xi_{max} = 0.87Re^{1/5} - 0.40Re^{2/5}We^{-1/2} \tag{4.12}$$

In [54], Clanet *et al.* performed test on a SHS, with a static contact angle of 170° (details on static contact angle measurement, contact angle hysteresis and composition of the surface are not provided in [54]). It is claimed that the experimental data on maximum spreading are well fit by the correlation:

$$\xi_{max} = 0.9We^{1/4} \tag{4.13}$$

for Weber numbers in the range $3 < We < 300$ (see Figure 2 in [54]). In the same study [54], the authors also claim that correlation in Equation 4.13 fits also well their experimental data for water impacting on a plastic hydrophilic surface, and experimental data obtained by Stow and Hadfield [65] for water impacting a smooth aluminum plate, and by Marmanis and Thoroddsen [66] for water impacting thick linen paper, with Weber numbers in the range $3 < We < 3000$ (see Figure 8 in [54]). As such, the authors claim the surface wettability does not play a role in the drop maximum spreading, not even for low We.

Two other studies in literature [60, 52] proposed a correlation for ξ_{max}, based on a energy balance approach between the moment of impact and the moment of maximum spreading. In both studies, effect of surface wettability is taken into account. In Pasandideh-Fard *et al.* study [60], ξ_{max} an explicit equation for ξ_{max} is given:

$$\xi_{max} = \sqrt{\frac{We + 12}{3(1 - \cos\theta_A) + 4\left(\frac{We}{\sqrt{Re}}\right)}} \tag{4.14}$$

In Mao *et al.* study [52], ξ_{max} can be found as the real root of the following cubic equation:

$$\left[\frac{1}{4}(1 - cos\theta) + 0.2\frac{We^{0.83}}{Re^{0.33}}\right]\xi_{max}^3 - \left(\frac{We}{12} + 1\right)\xi_{max} + \frac{2}{3} = 0 \tag{4.15}$$

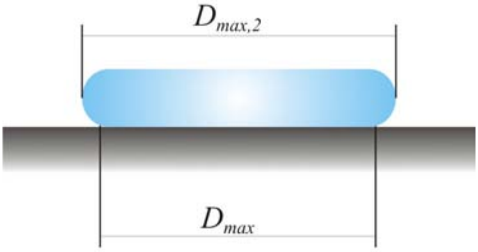

Figure 4.5: Schematic of a drop at maximum spreading. Image illustrates two possible definitions for drop maximum spreading, either as D_{max} (at liquid-solid interface, as typical in literature) or $D_{max,2}$ (as drop maximum width).

In the present work, the value of the advancing contact angle, θ_A, is used instead of the static contact angle, θ, as in the original work [52], for the reasons explained in the previous section.

Many open questions arise from the comparison of the five above mentioned correlations. First of all, the definition of maximum diameter: in literature, D_{max} is typically defined as the maximum *contact* diameter, measured at the liquid-surface (indicated as D_{max} in Figure 4.5). It is not clear from [54] if the same definition for maximum diameter is used, or maximum diameter is defined as maximum width of the drop (indicated as $D_{max,2}$ in Figure 4.5), not necessarily measured at the liquid-surface interface, as the image sequence in [54] (Figure 1, Subfigure 3) suggests. For a drop impacting on a SHS, the difference between the two values is 8% at $We = 27$ and 4% at $We = 92$ (being always $D_{max,2} \geq D_{max}$, by definition) and becomes negligible at higher We numbers; difference between $D_{max,2}$ and D_{max} are even smaller for drop impacting on more hydrophilic surfaces and thus can be neglected. Nonetheless, the difference between two maximum diameter definitions will be taken into account when discussing results.

Second, all correlations agree that the maximum spread factor, ξ_{max}, increases with velocity following a power law $\xi_{max} \propto V^{\alpha}$. However, different correlations disagree on the value of the exponent α. In high Weber and Reynolds number regime, i.e. when the effect of wettability are secondary compared to inertial effects, Scheller and Bousfield [45] predict an exponent $\alpha = 0.33$. Pasandideh-Fard *et al.* [49] $0.23 < \alpha < 0.38$ ($0° < \theta < 180°$), and Clanet *et al.* [54] $\alpha = 0.50$. For Roisman [51] correlation, slope is not constant: the value $\alpha = 0.31$ is found when fitting data in the proximity $We = 650$ and $Re = 12000$ (highest limit of We and Re for the present experimental study). Using Mao *et al.* [52] correlation, the exponent is $0.32 < \alpha < 0.45$ for $0° < \theta < 180°$.

Third, Clanet *et al.* [54], from their results, claim that viscosity and surface wettability do not affect the maximum spreading, not even at low-moderate Weber numbers (We in the order of unities or tens): the correlation reported in Equation 4.13 [54] show that maximum spreading is only a function of We. This result, which in [54] is claimed to be valid not only for superhydrophobic, but also hydrophilic surfaces, differs with other correlations reported above. All other four correlations [45, 51, 52, 60] include viscosity (through the Reynolds number, $Re = \rho V D_0/\mu$, or the Ohnesorge number, $Oh = \mu/\sqrt{\rho\sigma D_0}$) and two correlations [52, 60] include the effect of surface wettability, through the contact angle. As such, one of the main objectives of the present study is to make clear which correlation best fits experimental data.

Three 1D analytical models were also implemented and tested against experimental data: 1) Delplanque and Rangel model (DR model) [62]; 2) Kim and Chun model (KC model) [61]; 3) Attané *et al.* model (AGM model) [63]. Models are all derived using an energy balance approach. Restrictive assumptions are made on the drop shape (spherical cap or cylindrical) and on the flow field inside the drop, in order to model the problem with an ordinary derivative equation (ODE) to predict time evolution of contact diameter, $D(t)$ (or equivalently contact radius, $r(t)$, or drop height $h(t)$). Having a second order ODE, two initial conditions have to be given, based on impact conditions. As an example, the ODE from Attané *et al.* [63] is reported here, written for the non-dimensional contact diameter, $\xi = \xi(\tau)$, as a function of the non-dimensional time ($\tau = tV/(D_0\sqrt{We})$):

$$\frac{1}{12}\frac{d}{d\tau}\left\{\left[\frac{2}{3}+\frac{1}{45}\frac{1}{\xi^6}\right]\left(\frac{d\xi}{d\tau}\right)^2\right\}+\frac{d}{d\tau}\left[\xi^2\left(1-\cos\theta_e\right)+\frac{1}{3\xi}\right]+ \\ 4Oh\left[3\xi^4+\frac{2}{3\xi^2}+s\xi\right]\left(\frac{d\xi}{d\tau}\right)^2=0 \qquad (4.16)$$

where s is an adjustable parameter to account for viscous dissipation and is calculated to best fit experimental data. Indeed, although all the models are analytical, meaning that are derived using energy conservation, they all include one or more parameter (especially for the dissipative term) to best fit experimental data. The related initial conditions are:

$$1=\left[\xi_0^2\left(1-\cos\theta_e\right)+\frac{1}{3\xi_0}\right]\Bigg|_{\theta_e<109^\circ} \qquad (4.17)$$

for the initial contact radius, ξ_0 (note that the equation is valid only if $\theta_e < 109^\circ$, otherwise initial condition $\xi_0 = 0.39$ is used), and:

$$\dot{\xi}_0=\left.\frac{d\xi}{d\tau}\right|_0=\sqrt{We}\left[\frac{2}{3}+\frac{1}{45}\frac{1}{\xi_0^6}\right]^{-1/2} \qquad (4.18)$$

for the initial contact radius derivative, $\dot{\xi}_0 = \dot{\xi}(\tau = 0)$ (corresponding to non-dimensional contact line speed). Note that KC and AGM models originally make use of the equilibrium contact angle, θ_e, as shown in Equation 4.16 from [63]. In the present study, the value of the advancing contact angle, θ_A, is used instead (see discussion in previous section). Note that, for KC model [61], a corrected version of the model was used as suggested in [63]. With respect to the model proposed in the original paper [61], the fitting coefficient $F_d = 30$ was used for the dissipation factor (see Table 3 in [61]). As suggested in [63], the value was mistakenly derived reproducing an error from a previous paper; the correct value for the fitting coefficient is $F_d = 15$, and this value was used as input for KC model.

It is also important to remark that KC and AGM model are very similar, with the main difference being the evaluation of dissipative term, which models the viscous effects. DR model [62] differentiate from the other two models for three main characteristics: it models only drop spreading phase (until maximum spreading), but not recoiling; it does not account for surface wettability; the model originally included also modeling for drop solidification: in the present study, we implemented the complete model as proposed in [62], but applied condition of isothermal impact (by imposing solidification parameter $K = 0$, see definition in Equation 28 in [62]).

Finally, performing a sensitivity analysis with AGM model, which is the most recent analytical model, we found that AGM predicts:

$$\xi_{max} = 0.6We^{1/6}Oh^{1/6} \tag{4.19}$$

for a very hydrophilic surface ($\theta_A = 20°$), which is very similar to the experimental correlation proposed in [45] and reported here in Equation 4.11. The AGM models also predicts that:

$$\xi_{max} = 0.34\frac{We^{1/4}}{Oh^{1/6}} \tag{4.20}$$

for a perfectly non-wettable surface ($\theta_A = 180°$). Equation 4.20 can be compared to correlation in Equation 4.13, proposed by Clanet *et al.* [54]. Equation agrees for the exponent of We; also, for a millimetric water drop (as in our case $D_0 = 2.86mm$, $Oh = 0.002$), equation 4.20 becomes $We = 0.96We^{1/4}$, showing a relatively good agreement between estimated prefactor (equal to 0.9 in 4.13, 6% difference). However, Equation 4.20 include the effect of viscosity through the Oh number, an effect that was neglected in [54].

4.2.4 Drop impact with solidification

Few studies in literature report results of non-isothermal drop impacts: two examples are [67] (molten wax drops) and [68] (molten metal drops). No single drop impact studies have been found in literature dealing with water drop impact in freezing conditions.

The important parameter that are expected to play a role in non-isothermal impact conditions are drop temperature, T_d, and surface temperature, T_s, as indicated in Figure 4.4. Other parameters are liquid freezing temperature, T_f (equal to 0°C for water) and liquid solidification latent heat, h_{ls}. A further interesting parameter is the contact temperature, T_{con}, which is the temperature measured at the interface when two bodies (in our case, the drop and the solid surface) with different temperatures are put in contact. The contact temperature is calculated as the average temperature, weighted by thermal effusivities, ϵ:

$$T_{\mathrm{con}} = \frac{\epsilon_d T_d + \epsilon_s T_s}{\epsilon_d + \epsilon_s} \tag{4.21}$$

where thermal effusivity is determined as the square root of the product of the material thermal conductivity and its volumetric heat capacity:

$$\epsilon = \sqrt{k \rho c_p} \tag{4.22}$$

.

4.3 Potentiality of SHS in icing conditions

Consider the case of a surface with a temperature below the freezing point, on which liquid drops impact. Two different mechanisms can be identified that can aid with icing mitigation: (i) partial or complete rebound of drop upon impact, with drop entrainment in a prevailing airflow; (ii) shedding of sessile drop, which is possible when liquid-surfaces adhesion forces are overcome by external forces (aerodynamic forces or gravity) [40]. Consider the first mechanism: a drop impinging on a hydrophilic surface spreads on the surface and does not recoil (or only partially recoils, i.e. the drop/solid contact area only partially reduces) after the spreading phase. In this case the drop remains on the surface and can freeze. But, a drop impinging on a superhydrophobic surface can recoil and a partial or complete drop rebound is observed. In this latter case, the drop can rebound after impact and detach from the surface prior to freezing. Shedding of a drop by an external force (the second mechanism), is also very useful for icing mitigation. On a hydrophilic surface, relatively high external forces are needed to overcome adhesion forces [38, 40]. For this reason, on hydrophilic surfaces drops stay attached to the surface or move slowly in the direction of the external force, and the drop can have enough time to freeze. A typical example of this type of ice formation is runback ice; runback ice is caused by liquid water flowing downstream, due to aerodynamic shear forces, and then freezing in the unheated areas, where anti-icing devices are not installed. On a superhydrophobic surface, the external force needed to overcome drop adhesion force is considerably less than on a hydrophilic surface: e.g. the critical air velocity for incipient motion for a 2µl drop is 20m/s on PMMA, and only 5m/s on a superhydrophobic surface [40] (meaning that the ratio between corresponding critical dynamic pressures is 1/16). Thus, water can be shed away by the external force in a shorter time on superhydrophobic surface (e.g. drop rebound time is approximately 110µs for a 100µm drop [53]) than on a hydrophilic surface; if shedding time is short enough, water can be removed before freezing occurs, and consequently ice formation can be decreased or inhibited.

4.4 Objectives of drop impact studies

On the basis of the illustrated state-of-the-art in drop impact phenomena, aim of the present study is to better understand the effect of wettability during the impact of a water drop on a surface, with particular attention to application in icing conditions.

As widely explained in a recent review [64], and discussed in the Section 4.2.3, correlations in literature disagree on different issues: among all, the relation between drop maximum spreading and impact speed, and the role played by surface wettability in the different phases after drop impact. For this reason, we decided to investigate drop impact on surface using a wide range of wettabilities, trying to understand the role played by each single parameter, such as advancing and receding contact angles, θ_A and θ_R, respectively, or roughness during the different drop impact phases. The problem of investigating the influence of a single parameter is not trivial, since surface properties are mostly interdependent and one property cannot be easily changed without affecting the others. In the present drop impact study ten different surfaces were used, of which three superhydrophobic, not only to cover a wide range of contact angles, but also to compare surfaces with similar characteristics: e.g. some surfaces have similar advancing contact angle, but different receding contact angles, or vice versa, or similar contact angle hysteresis (defined as difference between advancing and receding contact angle) but different advancing contact angle.

Tests were first performed in isothermal conditions, for two reasons: the first is methodological, and is due to the necessity of investigating the effect of each single parameter, e.g. surface wettability, independently from changes of other parameters. The second reason is related to the application of the coating strategy, which is a mitigation strategy; as such, coating strategy is not proposed as an alternative to anti-icing, but a complementary solution, used to improve the efficiency of existing systems. For this reason, we expect that heating of the wing will be necessary in the drop impingement areas on the aerodynamic surfaces, so that drop will impact on surfaces kept above the freezing temperature.

Results from isothermal drop impact studies are presented in Chapter 6. The second series of tests are performed in freezing conditions, by making the drop impacting on cold surfaces, kept at temperature below the freezing point. Results from this part of the work are illstrated in Chapter 7.

Chapter 5

Experimental apparatus for drop impact and surface preparation

The present chapter provides a description of the experimental test rig, which has been designed and built to study drop impact phenomena, and some details on the preparation of different surfaces.

5.1 Drop impact test rig

In order to study drop impact on a solid surface in both isothermal and freezing conditions, an *ad hoc* experimental apparatus has been designed and built. The general structure of the test rig is that typical of drop impact studies, and thus is similar to others test rigs reported in literature, and to two other test rigs already present at the Thermal Physics Laboratory of the University of Bergamo, which had been previously built to study drop impact on hot surfaces or on liquid films (see for example [69]). The core of the experimental apparatus is a high-speed camera, which allows to record all the phases of drop impact at a high frame rate. With respect to the two existing apparatus, the new one presents the following peculiarities: (i) a specifically designed cooling system, to achieve sub-zero temperatures at

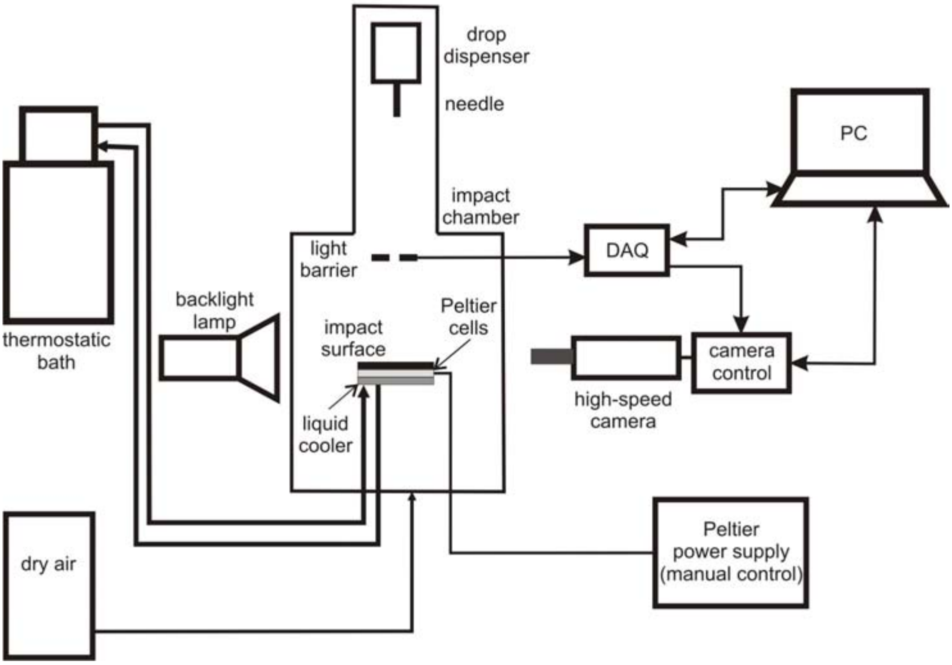

Figure 5.1: Schematic of the drop impact experimental apparatus.

the impact surface; (ii) the possibility to study both normal and oblique impacts.

Figure 5.1 illustrates a schematic of the experimental apparatus and Figure 5.2 shows two views of the assembled apparatus. The main components are: the drop generator, the impact surface and its support, the cooling system, and the high speed camera camera equipment.

The water drop is generated at the needle tip. When the drop detaches from the needle, it accelerates under gravity effect and impacts on the target surface, which can be cooled down to temperatures below the freezing point, thanks to a specifically designed cooling system.

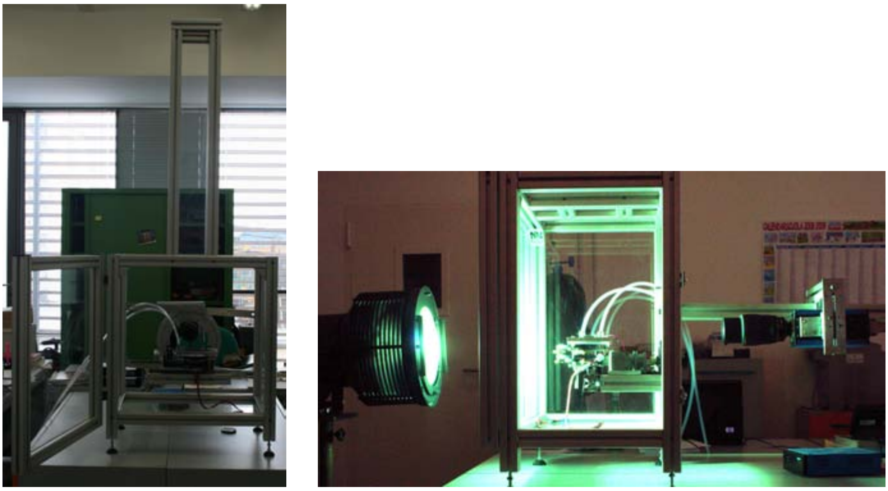

a. b.

Figure 5.2: Front and side view of the experimental apparatus.

The drop impact is recorded using a high speed 10 bit CMOS camera, model *pco.1200 hs*, whose frame rate is 486fps (frame per second) at full frame (1280x1024). The use of the high speed camera allows a phenomenological study of the drop impact dynamics.

The target surface can be tilted, so that impacts at different impact angles can be observed. The surface can also translate in one direction, so that the same surface can be used for several impacts each time, before cleaning is required.

In the following sections a description of the following systems is given: (i) the apparatus structure, consisting of impact tower, target surface support and movement system; (ii) the drop generation system; (iii) the impact surface cooling system; (iv) the drop impact recording system.

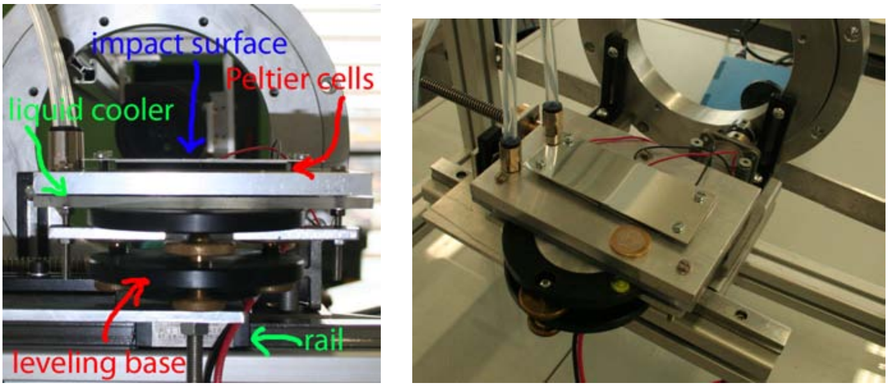

a. b.

Figure 5.3: Close-up view of the experimental apparatus on the drop impact area.

5.1.1 Apparatus structure

The apparatus structure consists of the so called “fall tower” and the support and movement system for the impact surface.

The impact tower was built using ITEM® bars, which can be flexibly assembled and combined. The height of the tower has an influence on the maximum drop impact velocities, since the drops is accelerated through gravity. For a free falling drop, if drag is neglected, the impact velocity, V, is equal to $\sqrt{2gh}$, where g is acceleration due to gravity and h is the fall height; in fact, the formula overpredicts the real drop impact velocity, since drag forces act as decelerating forces. Ideally, the maximum fall height has to be chosen according to the required maximum impact velocity. However, practical limitations exist. If the height is excessive, even small perturbation to the drop path may cause the drop to fall far away from the expected impact point; thus, the impact may be out of the camera focus plane or even outside the camera observation window. Experience in previous tests has shown that the maximum height should not be greater than 1m, leading to maximum drop impact speed of approximately 4m/s. Therefore, this is the maximum possible height for this experimental apparatus. Similar test

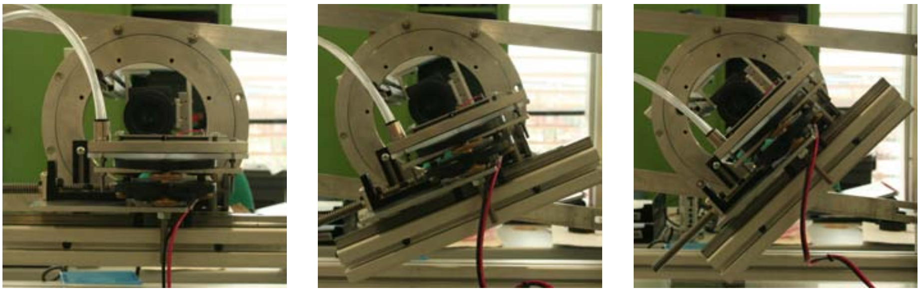

a. b. c.

Figure 5.4: Rotation of the surface to different tilt angles: a. normal impact; b. and c. oblique impact.

rigs in literature present the same maximum impact velocity.

Transparent Plexiglass® panels are mounted on the tower walls for two reasons: to avoid disturbance from the fluctuations of the surrounding air, and to create a close dry air environment inside the impact tower, in order to avoid condensation of vapor on the impact surface, which is kept below 0℃ for drop impact tests in freezing conditions. A small flow of dry air maintains a slight positive pressure inside the chamber while experiments are conducted, preventing humid air from seeping in.

The surface support and movement system is shown in Figure 5.3. A specifically designed aluminum ball bearing is used to hold the impact surface, together with its linear movement system and the cooling system. The support allows to tilt the surface at different angles, in order to vary the impact angles within a range from 90°(normal impact) to almost 0°(see Figure 5.4). The camera is also mounted on the same ball bearing, so that the camera movement is integral with that of the impact surface. The surface can translate on a rail, which is moved be a worm. The position of the surface can be manually controlled from outside the chamber. After each impact, the surface is moved in order to change the position of the impact point: this strategy allows to perform several tests on the same surface, with no need for cleaning it after each impact. The support system also includes a leveling base (from Manfrotto™) to obtain an accurate leveling of the impact surface (see Figure 5.3a).

5.1.2 Drop generation

The drop generation system consists of a drop reservoir and a needle (see Figure 5.5). For isothermal drop impacts, water temperature is kept at room temperature, approximately 22°C. For drop impacts in freezing conditions, temperature of water in the reservoir is kept at 0°C using a mixture of water and ice. Ideally, test should be performed using supercooled drops, i.e. drops below the freezing temperatures, as this is the condition of atmospheric water drops in icing conditions. However, it is not easy to maintain water supercooled, because the state is metastable: small perturbations will cause drop freezing. As such, water for tests was kept at the freezing temperature, which is the lowest temperature at which water remains stable at ambient pressure.

Drops are generated at the tip of the needle and detach by gravity: the drop is grown slowly, quasi-statically, and it detaches when gravity force overcomes adhesion force. Typical drop size is $2.6 - 3$mm.

5.1.3 Impact surface cooling system

The impact surface cooling system was specifically designed to reach temperature far below the freezing points. It is divided into two subsystems: the Peltier cells system and the liquid cooling system (see Figure 5.6).

Peltier cells are compact devices whose functioning is based on the Peltier effect, i.e. the thermo-electric effect that allows the conversion of electrical voltage into temperature differences. A Peltier cell is a solid-state active heat pump which transfers heat from one side of the device to the other side against the temperature gradient (from cold to hot), with consumption of electrical energy. In other words, when current is applied to a Peltier cell, a temperature gradient is produced between the two Peltier sides. The temperature gradient intensity of the gradients depend both on the supplied electrical power and on the operating boundary conditions.

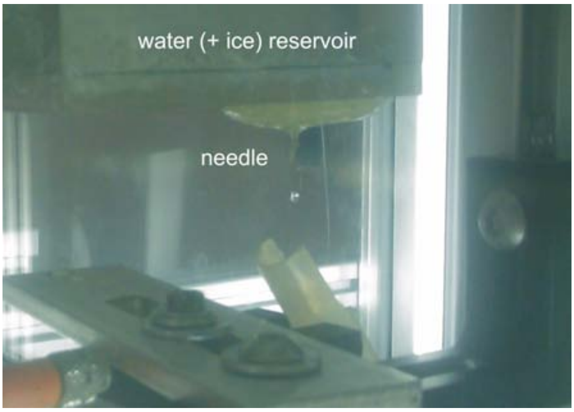

Figure 5.5: Drop generation system: water reservoir and needle. Ice is added in the water reservoir for drop impacts in freezing conditions maintain temperature at 0℃.

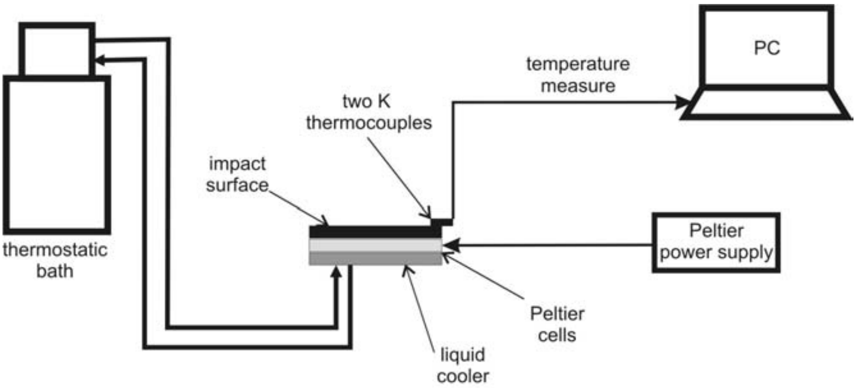

Figure 5.6: Schematic of the cooling system.

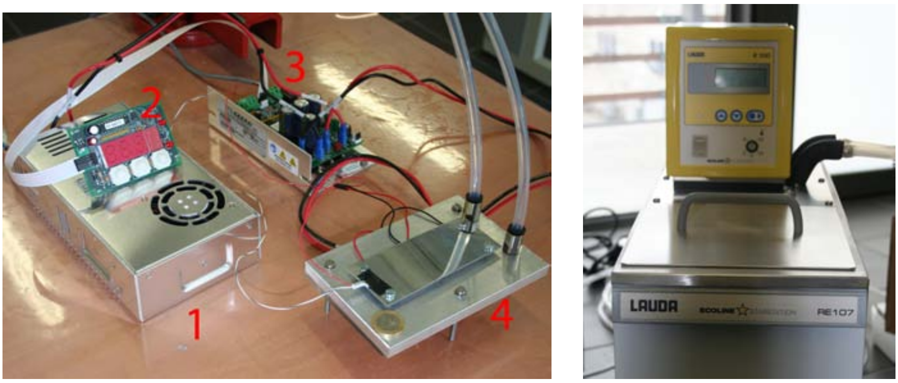

a. b.

Figure 5.7: Cooling system. a. Components: 1. Peltier power supply; 2. Peltier controller display; 3. Peltier controller; 4. Peltier devices and liquid cooler mounted below the impact surface. b. LAUDA RE107 thermostatic bath.

Peltier cells are very practical for small applications, where energy loads are not high, in the order of watts.

The Peltier cooling system can be controlled both manually and automatically. In the manual mode, power supply is provided using a GWInstek PSH-6006A power supply, which allows a direct control of the supplied power. Surface temperature, which is measured by two K-type thermocouples, is monitored on the PC and power supply is regulated manually to achieve impact surface set temperature. Using the automatic control mode, power supply to Peltier cells is controlled by a PID (proportional-integral-derivative) controller unit (TC-36-25-RS232), which regulates power from a 24V power supply (PS-24-12.5) (see Figure 5.7a). In this mode, temperature measurements are used as feedback data by the controller by means of a closed-loop control. Two Peltier cells, either single-stage (TE-127-1.4-2.5) or multi-stage (TE-2-127-127-1.15), are mounted beside the impact surface. All components, but power supply for manual control, are produced by TETechnology, Inc., US[1].

---

[1] TETechnology components where chosen, since the controller unit TC-36-25-RS232

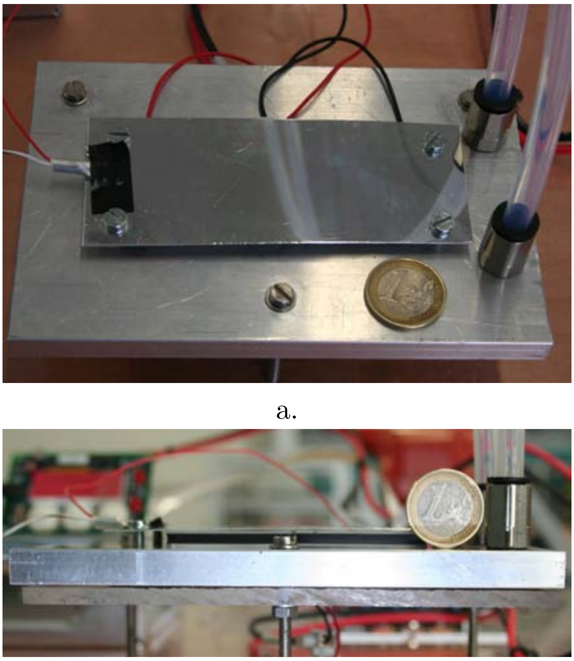
a.

b.

Figure 5.8: Cooling system: top (a.) and side (b.) views of the cooling system mounted below the impact surface.

The two Peltier cells (size 40x40mm^2) are mounted side by side (see Figure 5.8), to give a total cooled area of 80x40mm^2. A secondary temperature sensor can be placed on the other side of the Peltier, to check eventual device overheating on the hot side. Preliminary surface temperature measurement on the impact surface showed that temperature distribution on the impact surface is homogeneous, with difference from minimum and maximum temperature equal to ±1°C.

The key point for an efficient functioning of the cell is the heat removal

---

was the only one that could operate down to -40°C. Standard controllers from other producers operate only down to -20°C.

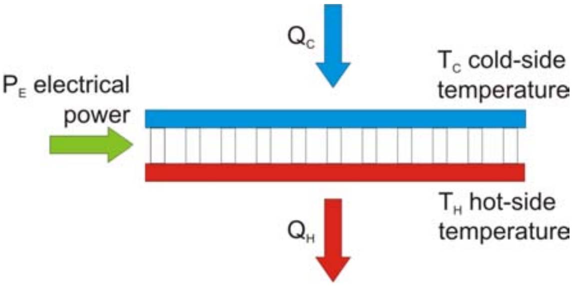

Figure 5.9: Schematic of a Peltier cell functioning.

from the hot side. From a simple energy balance, it can be observed that:

$$\dot{Q}_H = \dot{Q}_C + P_E \tag{5.1}$$

where P_E is the electrical power and Q_C and Q_H are the heat loads on the cold and the hot side, respectively (see Figure 5.9). The Peltier cell efficiency is defined as the ratio between the heat removed from the cold side and the electrical consumption, $\dot{Q}_C/P_E$. If removal of Q_H is not adequate, the temperature on the hot side, T_H, will increase. Thus, the temperature on the cold side, T_C, will increase, too, with the effect of reducing Q_C and the efficiency of the device.

For this reason, it was necessary to integrate a supplementary cooling for heat removal from the Peltier hot side. Different solutions have been considered, such as forced air cooling, heat pipes and liquid cooling. The liquid cooling was chosen as the most appropriate for this specific application due to its flexibility. The liquid cooling system consists of a thermostatic bath, PFTE (polytetrafluoroethylene) pipes and a liquid exchanger (see Figure 5.6). The thermostatic bath (LAUDA RE107, see Figure 5.7b) is a 6l bath with a temperature range between -35 and 150℃. The bath liquid is water mixed with glycol to work also at temperatures below 0℃. The bath is also equipped with a circulating pump, with a prevalence of 0.4bar. The cooling liquid circulates in the external cooling system to the liquid exchanger, which is in direct contact with the Peltier hot side and removes the required

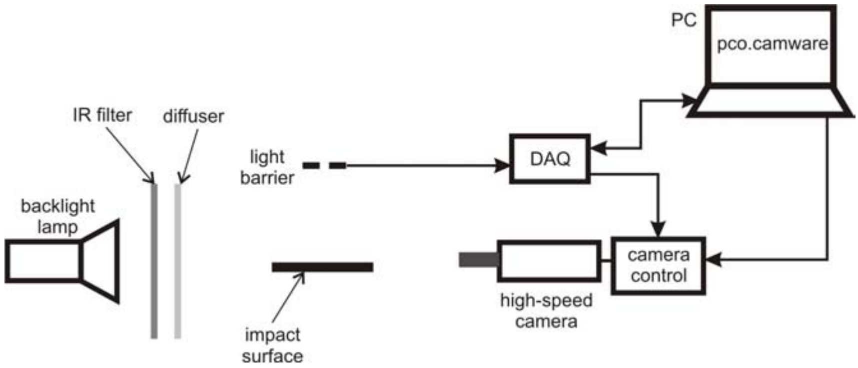

Figure 5.10: Schematic of the high speed camera system.

heat. For an adequate cooling of the hot side, the cooling liquid is kept at approximately 5°C.

The liquid cooling system could have been used even as stand-alone system for the impact surface cooling. This option was at first considered, but later rejected for two main reasons: the thermostatic bath is limited by the lower temperature that can be achieved (-35°C), a limit that can be easily lowered by combined use of thermostatic bath and Peltier cells; the liquid cooling system has a high inertia and it is more difficult to precisely control the temperature than with Peltier cells. Therefore, the combination of a liquid cooling system together with Peltier cells represents a much more appropriate solution.

5.1.4 High speed camera and image analysis

A schematic of the high speed camera system is reported in Figure 5.10. A high speed camera (pco.1200hs - see Figure 5.11), already available at the Thermal Physics Laboratory, was used to record the drop impact dynamics. As a drop falls towards the surface, it passes through a fork sensor (model GLS10, STM), which can detect the drop passage. The drop detection signal is used to activate the image acquisition with the camera. A dedicated hardware controls the delay time between sensor detection and the

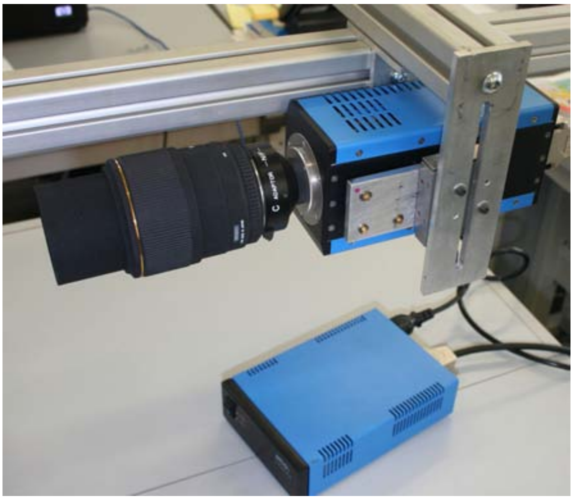

Figure 5.11: High speed camera and camera controller. The camera is installed on micrometers to allow precise positioning and orientation.

beginning of image acquisition, and also the duration of image acquisition.

The camera frame rate and exposure time can be set according to the requirements. The maximum frame rate is 486fps at full frame (1280x1024), but it can also be increased if the observation window is reduced: the camera was used at maximum speed of 21300fps, with a window of $1280x20$ pixels. The camera parameters and the record window are controlled through a specific software, supplied with the camera, *pco.camware*. Previous tests on drop impact on hot surface or liquid layers showed that the exposure time should be approximately $20-30$µs to freeze the drop deformation. A Sigma macro lens (MACRO 105mm F2.8 EX DG) was used during tests. Since the maximum lens magnification is 1x, the best spatial resolution that can be achieved is equal to the pixel size, i.e. 12µm, which is sufficient to observe the deformation of a millimetric drop. A 1KW backlight lamp is required to provide a sufficient illumination with such a reduced exposure time. Due to the high heat radiation produced by the lamp and to avoid undesired heating of the impact surface, an infrared (IR) filter was positioned between the lamp and the impact chamber. Tests with a black surface showed that the IR filter is able to stop 90% of the total power irradiated by the lamp. Also, to provide a more regular illumination of the impact area, a second glass filter was used to diffuse lamp light (see Figure 5.10).

Figure 5.12 illustrates two image sequences for a drop impacting on PMMA and SHS-Teflon ($D = 2.8mm$, $V = 2.0m/s$). Majority of images were recorded from side (horizontal camera positioning); for those tests, where presence of secondary drops disturbed observation from side (typically on SHS at high We numbers), images were recorded mounting the camera with a tilt angle of 19°. Images were automatically analyzed using a code, developed in MatLab® environment; the image analysis code provided the following information (see also schematic in Figure 5.13): (1) time evolution of contact diameter, $D(t)$, and spread factor $\xi(t) = D(t)/D_0$; (2) maximum spread factor, $\xi_{max} = D_{max}/D_0$; (3) drop final spread factor; (4) spreading time, t_s, and time to maximum spreading, $t_{\xi_{max}}$; (5) time at maximum spreading, $\Delta t_{\xi_{max}}$, i.e. the time delay between the moment drop stops spreading and the moment drop starts receding; and eventually (6) drop rebound time, $t_{rebound}$, if drop rebounds. In order to calculate $t_{\xi_{max}}$ and $\Delta t_{\xi_{max}}$, the image analysis code calculates two characteristic times, t_s and t_r, which correspond to the time instants when drop stops spreading and when drop starts receding, respectively (see Figure 5.13). The two instants are evaluated as the two times when spread factor, ξ, crosses the threshold $0.99\xi_{max}$; $t_{\xi_{max}}$ is calculated as the average of t_s and t_r, and $\Delta t_{\xi_{max}}$ as their difference (see Figure 5.13).

5.2 Surface preparation for drop impact tests

Drop impact tests in isothermal conditions were performed on the following surfaces: (i) untreated smooth glass; (ii) PMMA (polymethylmethacrylate); (iii) Teflon; (iv) SHS-Teflon; (v) OTSa; (vi) OTSb; (vii) OTSc; (viii) OTSd, (ix) SHS-Zonyl-a (x) SHS-Zonyl-b. Substrates used for coating application was aluminum for surfaces (ii), (iii), (iv), (ix), (x) and smooth microscope

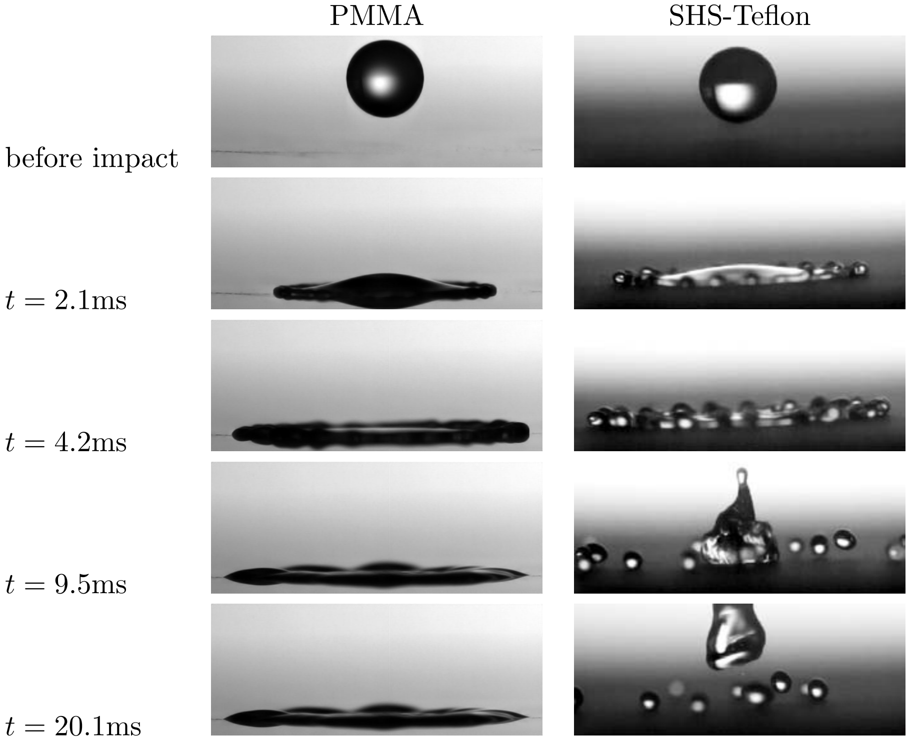

Figure 5.12: Image sequence of water drop impacting on a dry surface ($D = 2.8mm$, $V = 2.0m/s$, $We = 150$, $t_{conv} = D/V = 1.4ms$). Surfaces are PMMA (left column) and SHS-Teflon (right column). Water drop rebound can be observed on SHS-Teflon surface.

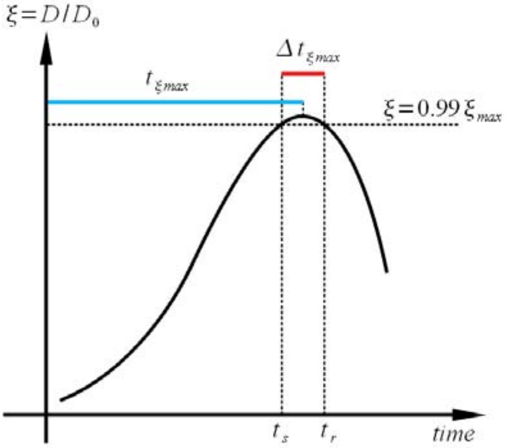

Figure 5.13: Schematic of spread factor evolution in time. Image analysis automatic code first detects t_s and t_r, identified as time instants when $\xi = 0.99\xi_{max}$; $t_{\xi_{max}}$ and $\Delta t_{\xi_{max}}$ are calculated as their average and the difference, respectively. Axes are not scaled.

glass for surfaces (v) to (viii). Surface (ii) was spray coated, depositing a thin layer of PMMA (a solution 1% w/w PMMA dissolved in dry toluene was used). Sample (iii) and (iv) were both spray coated, depositing a thin layer of Teflon over the surface; for sample (iii), Teflon was directly applied onto smooth aluminum sheet; sample (iv) was first etched in acid solution, to achieve the desired surface roughness, and then sprayed with Teflon. To etch aluminum, a 36% v/v solution of hydrochloric (HCl) acid in deionized water was prepared. The aluminum sheet was immersed into the acid solution for 1.5 minutes, allowing optimal surface texture to develop. The Teflon coating used for samples (iii) and (iv) was obtained with a 10:1 v/v solution of FC-75 and Teflon AF® from DuPont™. Once solution was applied, samples were placed in a vacuum oven (34 mbar) at 120℃ for one hour. Surfaces (v) to (viii) were grafted with octadecyltrichlorosilane (OTS, $C_{18}H_{37}Cl_3Si$) following the procedure described in details in [70]; each sample was exposed to UV for different times to modify the contact angles (maximum exposure time was 4 minutes for surface (viii)). Surfaces (ix) and (x) were spray coated using a method similar to what proposed by [71], where the authors developed an orgonoclay nanocomposite film, which is claimed to be highly durable and abrasion resistant. The original coating from [71] was partly modified to substitute the original bio-adhesive, which is a proprietary component, with a commercially available adhesive. The final list of components and corresponding concentrations (by weight) of the spray used for coating surfaces (ix) and (x) is: a fluorinated product, Zonyl 8740® from DuPont™(50%), nano clay (7%), solvents for dispersing the nano particles, ethanol (30%) and DMSO (dymethil sulfoxide, 9%), and an adhesive component (4%), which is 3M™ Scotch-Weld™ Threadlocker TL62 for surface (ix) and Permabond® MM115 Pure™ for surface (x). More details for surfaces (ix) and (x) can be found in [72].

All surfaces were characterized by measuring advancing and receding contact angles using the sessile drop method, and measuring both surface mean roughness, R_a, and rms roughness, R_q (roughmeter Diavite DH-5). Results form measurement are reported in Table 5.1. Use of ten different surfaces allows to cover a wide range of advancing and receding contact angles ($46° < \theta_A < 168°$, $5° < \theta_R < 155°$) and contact angle hysteresis

Table 5.1: Characteristics of surfaces used for drop impact tests in isothermal conditions: advancing (θ_A) and receding (θ_R) contact angles, surface mean roughness, R_a, and rms roughness, R_q, for tested surfaces in isothermal drop impact tests. Standard deviation is ±2°.

	surface	θ_A [°]	θ_R [°]	R_a µm	R_q µm
i)	glass	46	< 5	0.04 ± 0.01	0.05 ± 0.01
ii)	PMMA	88	39	0.50 ± 0.10	0.75 ± 0.15
iii)	Teflon	123	100	0.50 ± 0.15	0.60 ± 0.20
iv)	OTSa	110	93	0.04 ± 0.01	0.04 ± 0.01
v)	OTSb	97	81	0.04 ± 0.01	0.04 ± 0.01
vi)	OTSc	55	< 10	0.04 ± 0.01	0.04 ± 0.01
vii)	OTSd	68	36	0.04 ± 0.01	0.04 ± 0.01
viii)	SHS-Teflon	162	154	2.7 ± 0.5	3.4 ± 0.5
ix)	SHS-Zonyl-a	168	155	2.4 ± 0.6	3.0 ± 0.7
x)	SHS-Zonyl-b	158	145	11 ± 2.0	15 ± 2.0

Table 5.2: Characteristics of surfaces used for drop impact tests in freezing conditions: advancing (θ_A) and receding (θ_R) contact angles, surface mean roughness, R_a, and rms roughness, R_q. Standard deviation is ±2°.

surface	θ_A [°]	θ_R [°]	R_a [µm]	R_q [µm]	$\epsilon = \sqrt{k\rho c_p}$ [m^2/s]
glass	46	< 5	0.04 ± 0.01	0.05 ± 0.01	1516
PMMA	88	39	0.50 ± 0.10	0.75 ± 0.15	-
Teflon	123	100	0.17 ± 0.04	0.22 ± 0.07	-
SHS-Teflon	162	154	2.7 ± 0.5	3.4 ± 0.5	-
Copper	92	48	0.05 ± 0.02	0.07 ± 0.02	37063
Aluminum	79	< 10	0.05 ± 0.02	0.07 ± 0.02	20507

($8^\circ < \Delta\theta_R < 50^\circ$). Note that surface can be grouped using different parameters: for example, OTSa and Teflon have the same advancing contact angle, but different receding contact angles. Surface roughness is another important parameter that differentiates SHS, which have similar advancing and receding contact angles ($158^\circ < \theta_A < 168^\circ$, $145^\circ < \theta_R < 155^\circ$).

For drop impacts in freezing conditions, tests were performed with six surfaces, whose characteristics are reported in Table 5.2. Three surface were the same as for isothermal drop impacts: glass, pmma, and SHS-Teflon. The Teflon surface was produced by depositing a Teflon coating on glass, instead of aluminum, as for surface used in isothermal impact test: contact angles are the same, but roughness is lower on glass substrate (compare values in Table 5.1 and 5.2). Copper and aluminum surface were included as test surfaces because of the high values of thermal effusivity (defined in (4.22)) for metallic materials, compared to other materials, such as glass (see Table 5.2). Both copper and aluminum were manually polished with polishing paper to obtain a smooth surface. As an example, consider that surface temperature is $T_s = -15$°C. Since water drops impact on the surface at $T_d = 0$°C and with thermal effusivity $\epsilon_d = 1562$ [$\mathrm{Ws}^{0.5}/\mathrm{m}^2\mathrm{K}$], the contact temperature at the drop/solid interface is (see Equation 4.21):

- $T_s \approx -7$°C on glass;
- $T_s \approx -14$°C on aluminum;
- $T_s \approx -14$°C on copper;

Chapter 6

Isothermal drop impact on a solid surface: effect of surface wettability

6.1 Experimental conditions

Drop impact test were performed at moderate and high We, in the range $30 < We < 680$, with the primary objective of evaluating in which conditions and how surface wettability influences the drop impact outcome. Drop diameter was kept constant (2.86mm$\pm$1%), velocity was varied from 0.90 to 4.2m/s ($\pm$0.6%), to give a constant Ohnesorge number ($Oh = 0.020 \pm 0.5\%$) and Weber numbers in the range $30 < We < 680$ ($\pm$2.2%). Drop, air and surface temperature are equal to room temperature, ≈ 22℃.

6.2 Drop shape evolution after impact

Figure 6.1 shows the temporal evolution of the spread factor, $\xi(t)$, on three surfaces: glass (hydrophilic), OTSa (hydrophobic) and SHS-Teflon (superhydrophobic) at $We = 30$ (moderate Weber regime, as shown later). It is clear from Figure 6.1 that a variation of the advancing and receding contact angles significantly influences drop deformation during spreading and

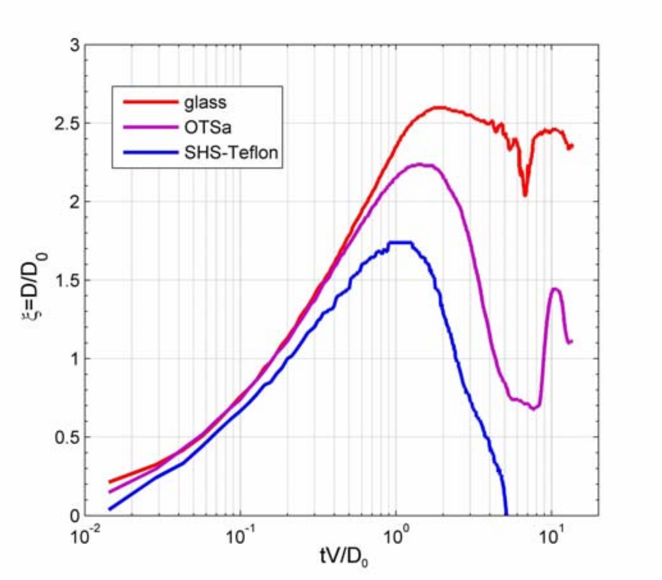

Figure 6.1: Spread factor, $\xi = D/D_0$, vs. non-dimensional time for drop impact on surfaces with different wettability ($We = 30$, $Oh = 0.002$). Drop rebounds from surface on SHS-Teflon (when $\xi = 0$, at $tV/D_0 \approx 5$), whereas contact diameter D oscillates on glass and OTSa, until steady state is reached.

receding phases, respectively. During the spreading phase, the higher the advancing contact angle, the lower the spreading and the spreading time (see Table 5.1 for wettability data). Spreading on surfaces with different advancing contact angles is similar in the first instants after impact (up to $tV/D_0 \approx 0.1$), when the inertial forces are dominating; thereafter, contact diameter evolve differently on the three surfaces. Differences on maximum spread factor, ξ_{max}, are approximately 30% between hydrophilic and most hydrophobic surfaces (glass and SHS-Teflon in Figure 6.1). Drop spreading time is also influenced by variation of the advancing contact angle: spreading time is approximately equal to one convective time (tV/D_0) on SHS-Teflon, whereas spreading time doubles on glass.

When drop reaches maximum spreading, time is needed before recoiling starts, due to contact angle hysteresis. For a SHS, contact angle hysteresis is significantly lower (8°) than on a hydrophilic surface ($\approx 40°$ for glass) and drop recoiling starts earlier. Finally, significant differences are observed in the recoiling phase. On SHS-Teflon, which has the highest receding contact angle, recoil is fast and drop rebound is observed after receding phase (when $\xi = 0$ in Figure 6.1), whereas drop contact diameter oscillates on the two other surfaces, until steady state is reached. Note that in general the final diameter depends on surface contact angles (for this reason, final diameter is higher on glass than on OTSa, which is hydrophobic), but also on impact conditions (e.g. We).

Figure 6.2 shows a comparison between experimental data for drop spread factor, $\xi(t)$, and predictions from analytical models for impact on glass, with We numbers in the range $30 < We < 683$. DR model [62] (see Figure 6.2a) does not predict spreading correctly, neither qualitatively nor quantitatively. As an example, the maximum spread factor is significantly overpredicted; also, the model predicts that spreading time increases with increasing We, whereas experimental data show the opposite trend. KC and AGM model (see Figure 6.2b and c) are substantially more accurate than DR model in predicting the maximum spread factor, ξ_{max}, and the time at maximum spreading, $t_{\xi_{max}}$: deviations between models and experimental data can be observed, but trends are captured correctly. Nevertheless, the major limitations of the model can be seen in the first

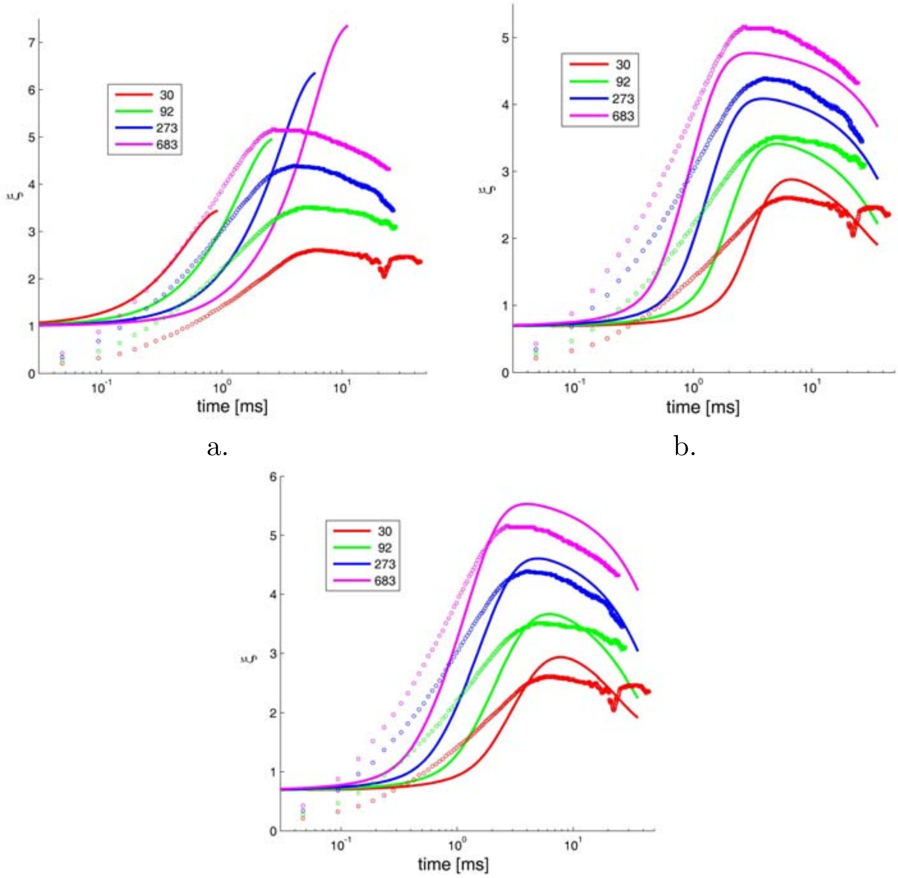

a.

b.

c.

Figure 6.2: Time evolution of drop spread factor, $\xi(t)$, on glass: comparison between experimental data and 1D analytical models. Circles are experimental data, continuous lines models. Legends report the corresponding Weber number. a. comparison with DR model by Delplanque & Rangel [62]; b. comparison with KC model by Kim & Chun [61]; c. comparison with AGM model by Attané *et al.* [63]; d. percentage error between model predictions and experimental data for $\xi(t)$ at $We = 683$.

instants after drop impact: drop contact diameter and its derivative (i.e., contact line speed) are not predicted accurately. The reason for that are the simplifications invoked in the models, since both KC and AGM model assume cylindrical shape for the spreading drop. This assumption holds in the proximity of drop maximum deformation, when $\xi \approx \xi_{max}$ (see Figure 5.12 at $t = 4.2ms$), but not in the initial one, when drop is formed by hemisphere and a spreading rim (see Figure 5.12 at $t = 2.1ms$). Also, another limitation of the analytical models is the choice of a constant contact angle, during the period the drop spreads (see Equation 4.16). First, the contact angle is not constant but changes with contact line speed. Second, dynamic contact angles are lower in the recoiling phase, when compared to spreading phase. To account for that, Attané *et al.* [63] proposed in the final part of their work [63] that a possible solutions is to use the advancing contact angle as reference contact angle during the spreading phase (mathematically, when $\dot{D}_{max} > 0$), and the receding contact angle in the recoiling phase ($\dot{D}_{max} > 0$). However, such a solution causes sudden changes in values of surface energy (which is defined as a function of the contact angle) during drop diameter oscillations, which can lead to non-physical drop diameter evolution.

Figure 6.3a shows a comparison between experimentally measured values of $\xi(t)$ and predictions by AGM model for impact on OTSa, in the range $30 < We < 530$. The agreement between experimental data and AGM is good and is even more accurate than in the case of drop impact on glass (see Figure 6.2). With regards to other analytical models (not illustrated for brevity) DR model showed poor agreement with experimental data as for glass, whereas results with KC model are similar to AGM model results.

In Figure 6.3b the comparison between experimental data for $\xi(t)$ and results from AGM model for drop impacting on SHS-Teflon is illustrated. Note that for SHS-Teflon the range of We was reduced to $30 < We < 276$, because at higher Weber numbers splash and drop fragmentation occur, and the presence of secondary drops does not allow automatic analysis of impact. For SHS-Teflon, drop rebound occurs in the entire analyzed We range: by *drop rebound* we mean entire drop rebound or rebound of a substantial part of liquid mass, referred to as drop core, in case of splash or

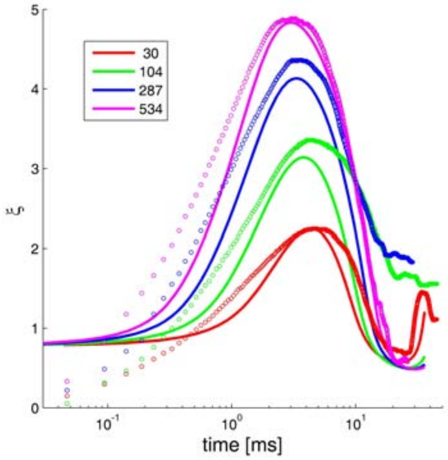

a.

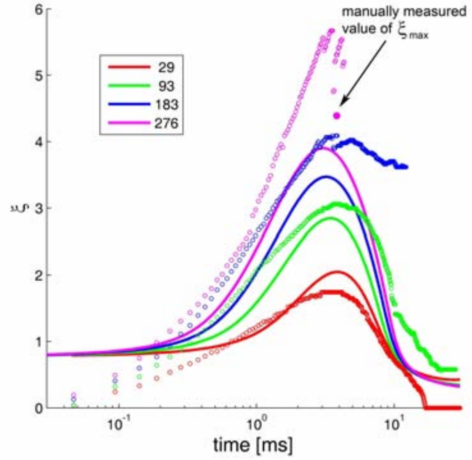

b.

Figure 6.3: Time evolution of drop spread factor, $\xi(t)$, on (a) OTSa and (b) SHS-Teflon. Figures show a comparison between experimental data (circle) and AGM model, from Attané *et al.* [63].

drop fragmentation (e.g. see image sequence Figure 5.12). Rebound on SHS-Teflon even at high We suggests that drop always remain in the so called Cassie-Baxter state and there is no transition to Wenzel state, which occurs when liquid penetrates vapor cavities at the liquid-solid interface (see [34] for a complete discussion on the two wetting states). Analyzing experimental data, it is apparent that complete drop rebound occurs at $We = 30$ (at time corresponding to $\xi = 0$). Rebound also occurs at higher We numbers, but automatic image analysis and contact diameter measurements are complicated by receding break-up [73] (at $We = 93$ and $We = 183$) and drop splashing (at $We = 276$). As an example, at $We = 276$, splashing occurs at $t = 1ms$ and small satellite drops are ejected from the rim. Only for first instants ($t < 1ms$) drop remains united and the rim can be detected by the image analysis automatic code, to allow measurement of $\xi(t)$. At $t = 1ms$, when rim starts decelerating, drop break-up occurs and a secondary drop is ejected at high speed from the rim, as shown by the sudden change in drop spread factor derivative. At $We = 276$, maximum spread factor, ξ_{max}, was measured manually and was reported in Figure 6.3b for reference.

Comparing experimental data from SHS-Teflon to AGM model (see Figure 6.3b), one can see that agreement is not as good as for drop impact on OTSa (see Figure 6.3a). Maximum spread factor, ξ_{max}, is overestimated at lower We numbers ($\sim +11\%$ at $We = 30$) and is underestimated at higher We numbers ($\sim -5\%$ at $We = 276$). Principal model limitations are the following:

- first, neither of the models predict a constant spreading time, as observed by experimental data (KC model clearly predicts decreasing spreading time with incresing We, whereas for AGM model the decrease with We is not as prominent);

- second, analytical models are not able to take into account drop fragmentation, due to splashing or receding break-up, leading to incorrect evaluation of surface energy (when drop is fragmented, interface surface increases, and so does surface energy);

- third, all models include an adjustable parameter (s in Equation 4.16 for AGM model) in the dissipative term that has to be determined by best fitting of experimental data and is not necessarily the same for each liquid-surface combination (in particular, fluid slip at liquid-solid interface may occur on a SHS [74, 75]);

- forth, models are not able to predict drop rebound: spread factor decreases down to $\xi \approx 0.4$ according to AGM model, but it does not vanish.

Nevertheless, it is valuable that time at which ξ reaches the local minimum, at the end of recoiling phase, is approximately constant for all We and is very close to experimentally measured rebound time, suggesting that drop oscillation time is captured correctly.

6.3 Maximum spread factor

Figure 6.4a illustrates maximum spread factor, ξ_{max}, as function of We for different surface wettabilities. Two regimes can be clearly identified: for moderate We number ($25 < We < 280$), drop maximum spreading is influenced by surface wettability; for high We number ($We > 280$) wettability plays minor role and all curves converge. Data for surfaces SHS-Zonyl-a and SHS-Zonyl-b overlap well with data for SHS-Teflon (they have not been reported in Figure 6.4a for graphical clarity).

The best fitting of experimental data was searched, using a correlation in the form:

$$\xi_{max} = k_1 \sqrt{\frac{We^{4/3}}{3(1-\cos\theta_A) + k_2 Oh^{1/3} We}} \tag{6.1}$$

The correlation has a similar form to equation 4.14, but present a different scaling for the dissipative term. Indeed, the proposed correlation corresponds to Equation 4.11 in the limiting case of perfectly hydrophilic surface (i.e. $\theta_A = 0°$). A fixed exponent, 1/6 ($\sqrt{1/3}$), was used for Oh,

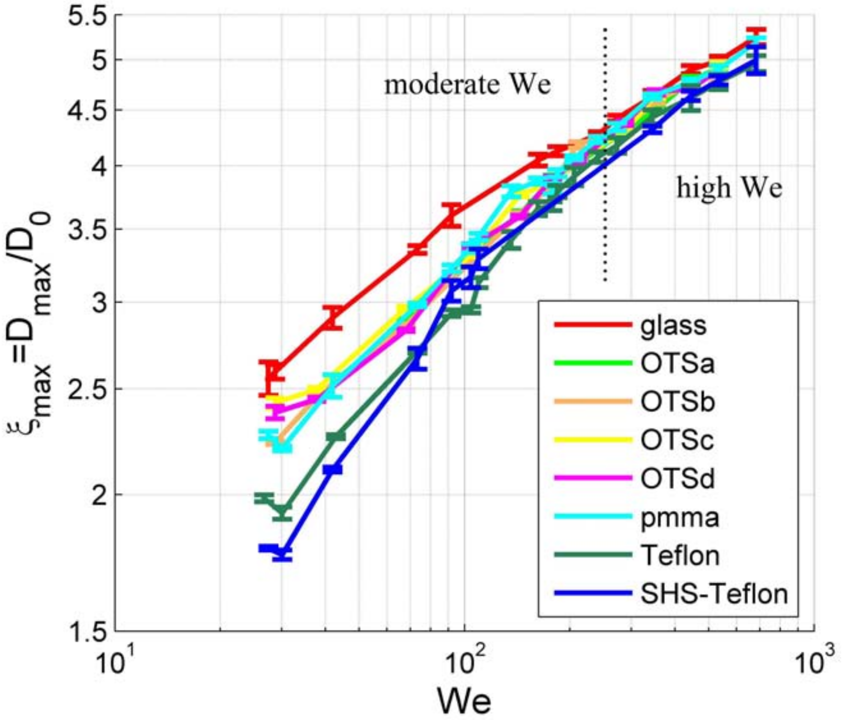

Figure 6.4: Experimental data for maximum spread factor, ξ_{max}, versus We for drop impacts on surfaces with different wettability. Lines for SHS-Zonyl-a and SHS-Zonyl-b overlap well with SHS-Teflon line, but were not inserted for graphical clarity. Lines between experimental points are to guide the eyes.

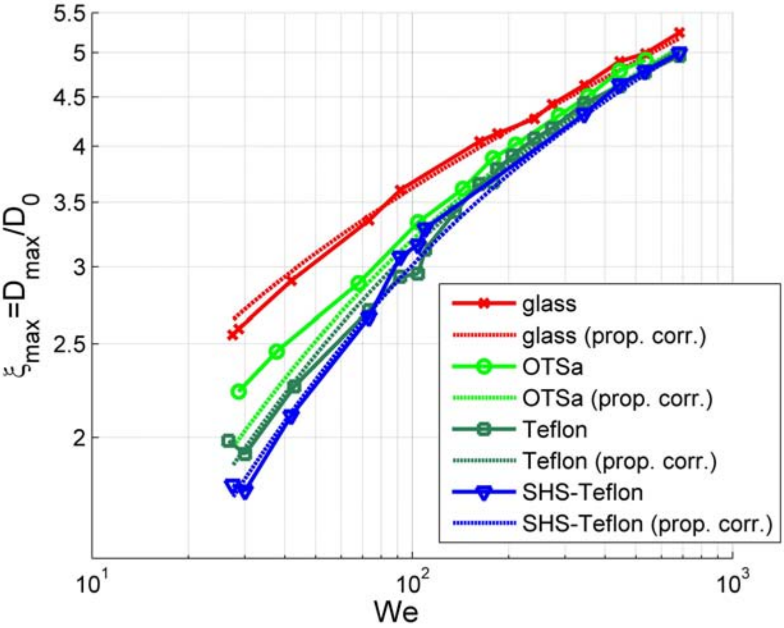

Figure 6.5: Comparison between experimental data for maximum spread factor, ξ_{max}, vs. We and predictions from Equation (6.2). Lines between experimental points are to guide the eyes.

Table 6.1: Comparison between experimentally measured values of maximum spread factor, ξ_{max}, empirical correlations [45, 51, 54, 60, 52] and 1D analytical models [62, 61, 63] for water drop impact on glass.

		correlations					models			
We	exp. value ξ_{max}	Sch. Bou. [45]	Roi. [51]	Cla. [54]	Pas.-Fard [60]	Mao [52]	DR [62]	KC [61]	AGM [63]	Eq. 6.2
30	2.6	+16%	-4%	-19%	+39%	+21%	+32%	+9%	+10%	-1%
70	3.3	+5%	-1%	-21%	+20%	+8%	+37%	-2%	+3%	0%
200	4.2	-2%	-1%	-19%	+7%	+1%	+40%	-8%	+1%	-2%
600	5.1	-3%	-2%	-13%	+2%	0%	+39%	-9%	+5%	-1%

since we did not change it in our experiments: the choice was consistent with Equation 4.11 [45] and results from AGM model [63] for both hydrophilic surface and SHS (see Equation 4.19 and 4.20, respectively). Only two fitting parameters are used in the proposed correlation, k_1 and k_2: k_1 is simply a pre-factor for the power law, and k_2 scales the dissipative term (this term is present in all models, including analytical models). The best fit of experimental results is:

$$\xi_{max} = 0.56\sqrt{\frac{We^{4/3}}{3(1-\cos\theta_A) + 0.81 Oh^{1/3} We}} \quad (R^2 = 0.992) \tag{6.2}$$

showing a very high correlation coefficient. Figure 6.5 illustrates a comparison between experimental data and predicted values by (6.2) for maximum spreading. For the limiting case of $\theta_A = 0°$, Equation (6.2) reduces to $\xi_{max} = 0.62(We/Oh)^{1/6}$, which corresponds to Equation 4.11 not only for the power form, but also for the pre-factor.

Tables 6.1, 6.2 and 6.3 report a comparison between experimentally measured values of ξ_{max} with correlations and 1D analytical models for water drop impacts on glass, OTSa, and SHS-Teflon, respectively. Comparison are done at four values of We: 30, 70, 200, 600.

Table 6.2: Comparison between experimentally measured values of maximum spread factor, ξ_{max}, empirical correlations [45, 51, 54, 60, 52] and 1D analytical models [62, 61, 63] for water drop impact on OTSa.

		correlations					models			
We	exp. value ξ_{max}	Sch. Bou. [45]	Roi. [51]	Cla. [54]	Pas.- Fard [60]	Mao [52]	DR [62]	KC [61]	AGM [63]	Eq. 6.2
30	2.3	+31%	+9%	-8%	+11%	0%	+49%	+1%	-2%	-13%
70	2.9	+19%	+13%	-10%	+8%	-1%	+56%	-6%	-3%	-2%
200	3.9	+6%	+6%	-13%	+1%	-4%	+51%	-9%	-4%	-1%
600	5.1	-3%	-2%	-13%	-4%	-6%	+39%	-13%	-3%	-3%

Table 6.3: Comparison between experimentally measured values of maximum spread factor, ξ_{max}, empirical correlations [45, 51, 54, 60, 52] and 1D analytical models [62, 61, 63] for water drop impact on SHS-Teflon.

		correlations					models			
We	exp. value ξ_{max}	Sch. Bou. [45]	Roi. [51]	Cla. [54]	Pas.- Fard [60]	Mao [52]	DR [62]	KC [61]	AGM [63]	Eq. 6.2
30	1.9	+62%	+34%	+13%	+22%	+11%	+84%	+16%	+11%	-3%
70	2.6	+33%	+26%	+0%	+9%	+2%	+74%	+3%	+1%	+2%
200	3.7	+12%	+12%	-9%	+1%	-4%	+59%	-7%	-4%	+1%
600	4.9	+1%	+2%	-9%	-4%	-5%	+45%	-11%	-2%	-1%

For drop impact on glass (see Table 6.1) the correlation from literature that best fits the experimental data is the one proposed by Roisman [51]. Correlation from Scheller and Bousfield [45], Pasandideh-Fard *et al.*, and Mao *et al.* [52] fits also well the data in the high We regime, but overestimates maximum spreading at moderate We numbers. Correlation from Clanet *et al.* [54] underestimates the value of maximum spreading by approximately 20% on the entire range. Among analytical models, DR model [62] does not fit well the experimental data (as was also seen in Figure 6.2a), and AGM model is moderately better than KC model; AGM fits the experimental data well, except for the lowest We (error of 10%). The proposed correlation (Equation 6.2) is the correlation that best fits the experimental data over the entire range of analyzed We.

For drop impact on OTSa (see Table 6.2), best fitting correlation is the one proposed by Mao *et al.* [52] over the entire We range. Correlations by Roisman [51] and by Scheller and Bousfield [45], developed for impacts on hydrophilic surfaces, fit well the experimental data at high We (where effect of wettability in maximum spreading is low), but overestimate the spreading at moderate We, where effect of advancing contact angle ($\theta_A = 112°$ for OTSa) is to reduce maximum spreading by approximately 10% in the moderate Weber regime ($We < 280$, see Figure 6.4). Correlation from Clanet *et al.* [54] underestimates ξ_{max} by approximately 10% over the entire range. Among analytical models, AGM model gives the best results; ξ_{max} is very well predicted for all We. The proposed correlation (Equation 6.2) fits experimental data very well, but for $We = 30$: this is the only case when error in prediction is higher than the standard deviation for the data.

For drop impact on SHS (see Table 6.3), correlations from literature derived to predict ξ_{max} on hydrophilic surfaces ([45, 51]) are all inaccurate and the best correlation is given by Mao *et al.* [52], which accounts for surface wettability. With regards to correlation by Clanet *et al.* [54], fitting of experimental data is poor. Nevertheless, it was not clear from [54] if the authors measured the maximum diameter at liquid solid interface or at drop maximum width (D_{max} and $D_{max,2}$, respectively, see Figure 4.5 and see discussion in Section 4.2). In any case, for high We, where $D_{max,2} \approx D_{max}$, correlation fits experimental data with less accuracy, i.e. the error is

$\sim 10\%$. The only correlation that fits the data well over the entire We range analyzed is the correlation proposed in Equation 6.2; it also reproduces well the variation in slope of the curve, shown in Figure 6.4.

Since the form of Equation 6.2 allows to fit well the experimental data, two important conclusion can be drawn. First, the data fitting confirms that $\xi_{max} \propto V^{1/3}$ (fitting of experimental data gives as exponent $0.35 \approx 1/3$). Second, Equation 6.2 allows to identify the impact conditions in which surface wettability has an effect on maximum drop diameter. The difference between a perfectly hydrophilic surface ($\theta_A = 0°$) and a perfect SHS ($\theta_A = 180°$) is higher than 10% if:

$$We < \frac{35}{Oh^{1/3}} \tag{6.3}$$

For the present case, when $Oh = 0.002$, the corresponding limit between moderate and high We numbers is $We = 280$, which is the limit indicated also in Figure 6.4. We are aware that Equation 6.2 (from which inequality 6.3 is derived) was derived by fitting data at constant Oh; nonetheless, Equation 6.2 was derived as a generalization of Equation 4.11, which was tested for a wide range of Oh numbers. Also, all the model and correlations reported above show minor differences on the dependence from the Oh number, being the exponent for Oh in a narrow range, between 1/6 and 1/4.

6.4 Drop impact scaling times

Significant outcomes are related to drop impact characteristic times, which are of particular interest in process where heat transfer processes (e.g. drop solidification) are involved. In the present section the time scaling for drop impact onto the most hydrophilic (glass) and one superhydrophobic surface (SHS-Teflon) is analyzed. In the following two sections, a comparison between spreading time and time at maximum spreading for all surfaces is presented.

Figure 6.6 illustrates the time evolution of the drop diameter, made non-dimensional with maximum contact diameter, $D(t)/D_{max}$, on glass

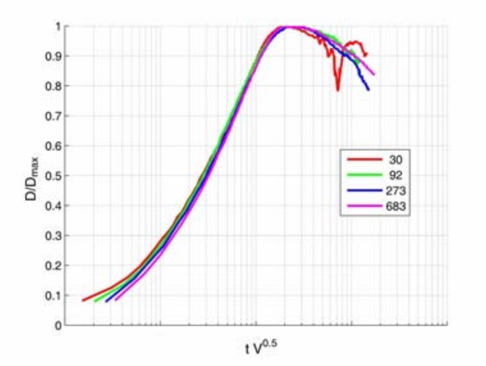

a.

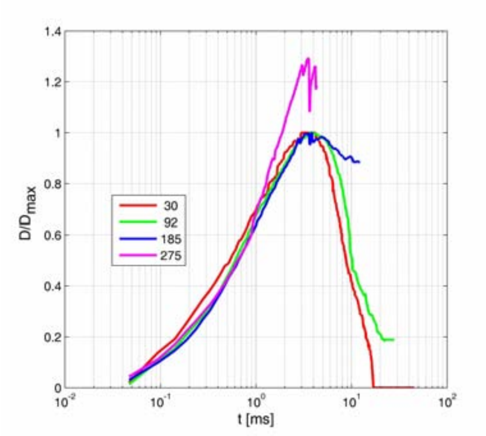

b.

Figure 6.6: Time evolution of drop contact diameter scaled by maximum contact diameter, $D(t)/D_{max}$, on glass (a) and on SHS-Teflon (b) at different We numbers (indicated in the legend). In (a) time is scaled by $V^{-0.5}$ (values of x-axis is not given because quantity t/$V^{-0.5}$ has no physical meaning); in (b) time is in ms. Note that automatic image analysis was not possible for $We > 275$ on SHS-Teflon due to secondary drop ejection (see also 6.3b).

(Figure 6.6a) and SHS-Teflon (see Figure 6.6b). Drop spreading evolution at different We is reported. For glass (see Figure 6.6a) all curves in the investigated range ($30 < We < 683$) collapse on a single curve if time is scaled with V^a, where a is between -0.4 and -0.5 (time scaling with value $V^{-0.5}$ is shown in Figure 6.6a) suggesting that drop characteristic times likely scales with $We^{a/2}$. Note that all curves overlap well not only in the spreading, but also in the recoiling phase. Differently, on the SHS-Teflon (Figure 6.6b) all curves collapse onto a single curve without scaling time, i.e. drop spreading time does not depend on impact speed in the investigated range ($30 < We < 275$). Curve overlap quite well even in the receding phase, although this may not be apparent directly from Figure 6.6b: automatic image analysis was complicated during the receding phase by receding break-up (see section 6.2). Nevertheless, manual image analysis showed that drop evolution during receding phase is similar, as confirmed by the fact that drop rebound time is constant, as shown below.

The two scalings highlight that dynamic interaction between water on a SHS is qualitatively different from the interaction on a hydrophilic surface. On a SHS, drop behaves almost as a mass-spring system: as shown in Equation 4.10, drop rebound time is associated to the oscillation time, which is proportional to the square root of the ratio between mass, m, and surface tension, σ. Thus, drop dynamic times are determined only by these two properties (m and σ) and do not depend on impact speed.

On a hydrophilic surfaces, the trend is different. For a drop impacting on a hydrophilic surface, results show that drop spreading deviates from the elastic response, which is typical of SHS, as observed on SHS-Teflon. The difference has likely to be attributed to the combined effect of capillary forces (which tend to enhance the spreading) and the strong damping mainly associated to viscous dissipation in the lamella boundary layer: as on a oscillating mass-spring system the oscillation time is modified by a damper, damping due to viscous dissipation on a hydrophilic surface increases the oscillation time (or equivalently, decreases frequency). Analytical models, e.g. [76, 63], show that a drop impacting on a surface can be modeled by a second order model ODE, as a mass-spring system with damping, the only difference being the presence of non-linear terms for

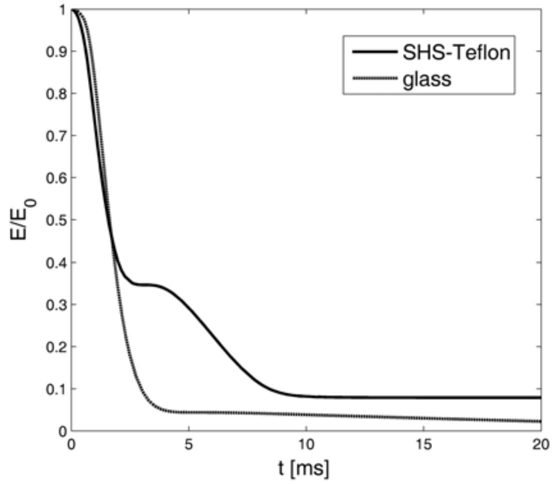

Figure 6.7: Time evolution of drop total mechanical energy, E (sum of surface energy and kinetic energy), made non-dimensional by initial value, E_0, at $t = 0$, corresponding to the moment of impact. Impact conditions are $D = 2.86mm$, $V = 2m/s$, $We = 150$.

ODE modeling drop impact. Indeed, for a drop impacting on a hydrophilic surface, since boundary layer shape and velocities strongly depend on impact conditions, in particular Re [50], drop characteristic time are affected by impact speed.

To confirm this intuition, deduced from experiments, analytical models can be used to evaluate the variation of the total mechanical energy after drop impact. Figure 6.7 illustrates the temporal evolution of mechanical energy, made non-dimensional with its initial value, E/E_0, for a water drop impacting on glass and on SHS-Teflon (impact conditions $D = 2.86mm$, $V = 2m/s$, $We = 150$); AGM model was used to evaluate mechanical energy. In the first stages, for $t < 2ms$, the inertial effects are dominating and the difference between the energy evolutions for drop impacting on the two surfaces is low. However, when drop is at maximum spreading (at $t = 4ms$, see also Figure 5.12, in which images of impact on PMMA and SHS-Teflon at $We = 150$ are shown) there is a clear difference in the remaining total mechanical energy: 33% for impact on SHS-Teflon, only 5% impact for glass. It is also possible that residual mechanical energy on SHS-Teflon is even higher than predicted by the analytical model, since no-slip condition at the liquid-surface interface may not necessarily apply for impacts on a SHS [74, 75], and viscous disspitation is probably lower than indicated by AGM model. This means that on a SHS, most of the mechanical energy is dissipated during the spreading phase, but at least 1/3 of the initial energy is still available, allowing the drop to recoil and rebound at $t = 20ms$ (rebound is not predicted by the analytical models, neither KC nor AGM, but was observed during experiments, as shown in Figure 5.12).

6.5 Spreading time

The change of drop spreading time, t_s, with We is illustrated in Figure 6.8a. For moderate We numbers, surface wettability has an effect on spreading time: at $We = 30$, spreading time varies from $3.5ms$ for SHS-Teflon and $9ms$ for glass. On one hand, on most hydrophilic surface, like glass, spreading time show a $We^{-1/4}$ trend, similar to the spreading time trend at higher We numbers. On the other hand, on hydrophobic and superhydrophobic surfaces (i.e. OTSa, OTSb, Teflon, SHS-Teflon, SHS-Zonyl-a and SHS-Zonyl-b), spreading time appears to be almost constant (note that SHS-Zonyl-a and SHS-Zonyl-b are not reported for graphical clarity). For high We numbers ($We > 280$), spreading time mainly depends on impact We number and influence of wettability is reduced: curves from different surfaces tend to converge to a single line at higher We, the slope is $We^{-1/4}$. The only curve that is somewhat separated from others is the SHS-Teflon curve: differences are most likely attributable to significant drop break-up occurring at the end of spreading phase, causing alteration of drop spreading (a part of the rim breaks up in small secondary drops, which do not recoil towards the impact point) and also making identification of spreading time more difficult (tilted view over the horizontal view was used and

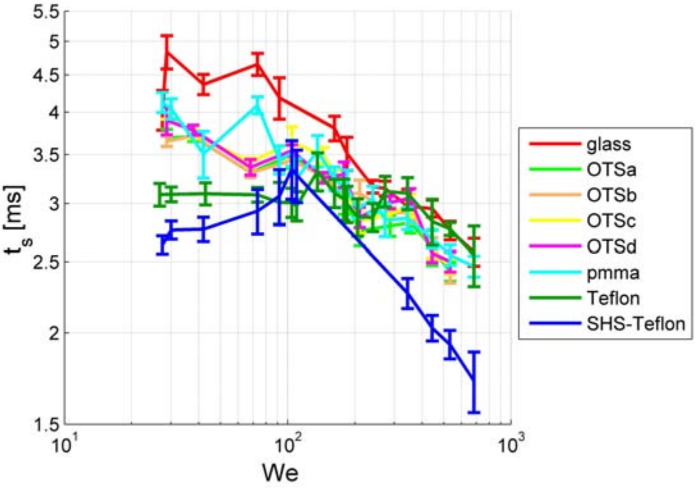

a.

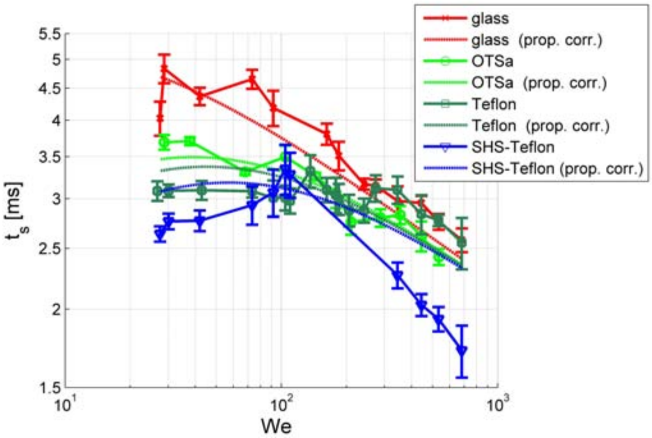

b.

Figure 6.8: (a) experimental values of spreading time, t_s vs. Weber number; (b) comparison between experimental data and Equation 6.4 for four selected surface.

images were analyzed manually for impacts on SHS-Teflon at high We).

The best fit of experimental data was achieved with the following equation:

$$\begin{aligned} t_s &= 0.22\frac{D_0}{V}\sqrt{\frac{We^{3/2}}{3(1-\cos\theta_A)+0.81Oh^{1/3}We}} \\ &= 0.39\frac{D_{max}}{V}We^{1/12} \quad (R^2 = 0.87) \end{aligned} \tag{6.4}$$

The correlation coefficient is lower than for the power law for ξ_{max} (Equation 6.2), mainly due to higher error bar in experimental data and due deviation of SHS curves from all others curves, due to drop fragmentation. Nonetheless, correlation coefficient is high and the equation captures well the trend at both low and high We, as shown in Figure 6.8: in particular, the proposed correlation, as experimental data, shows a constant spreading time at moderate We for most hydrophobic surfaces.

Contact line average speed can be estimated as the ratio between D_{max} and the spreading time:

$$\bar{V}_{cl} \approx \frac{D_{max}}{t_s} = 2.6V\frac{1}{We^{1/12}} \tag{6.5}$$

Showing that contact line average speed is mainly a function of impact velocity and is independent from surface wettability.

6.6 Time at maximum spreading

Another characteristic time is the time at maximum spreading, $\Delta t_{\xi_{max}}$, i.e. the time interval between the moment the drop stops spreading and when it starts receding (see Figure 5.13). A clear trend of data can be observed: time at maximum spreading decreases with increasing We number and with decreasing contact angle hysteresis, $\Delta\theta$. This behavior can be explained considering that, when the hysteresis, the drop need more time to change the contact angle from the advancing to the receding value. It is

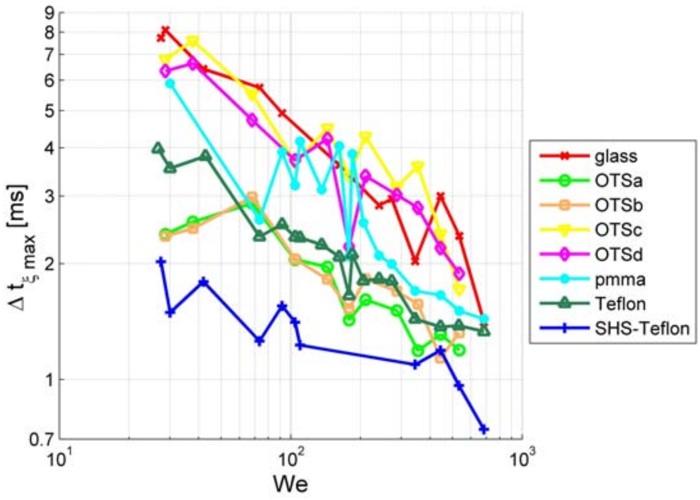

Figure 6.9: Time at maximum spreading, $\Delta t_{\xi_{max}}$ (see definition in Section 5.2) vs. Weber number.

noteworthy that for $\Delta t_{\xi_{max}}$ a distinction between moderate and high We numbers is not apparent as for drop spreading time, since curves do not overlap, even for high We. Hydrophilic surfaces maintain an approximately constant slope ($We^{-2/5}$ for glass surface) on the entire analyzed We range. Surfaces with lowest contact angle hysteresis (SHS-Teflon, OTSa, OTSb) show approximately constant $\Delta t_{\xi_{max}}$ for moderate We. It is important to stress that correlation between $\Delta t_{\xi_{max}}$ and wettability can be found by using contact angle hysteresis, $\Delta\theta$, rather than advancing contact angle, θ_A. For example, Teflon sample, which is less wettable than OTSa and OTSb (considering advancing contact angle), but has higher contact angle hysteresis, shows a trend more similar to a more hydrophilic surface, like PMMA, which has a similar $\Delta\theta$. Contact angle hysteresis, $\Delta t_{\xi_{max}}$, has an effect even when We numbers are high: when the drop reaches maximum diameter, contact line speed is close to zero and capillary effect, which are initially negligible compared to inertial effects, start to play an important role. The role of capillarity can be understood well looking back at Figure 6.1: in the first stages of spreading (until 3-4 convective times, D/V), glass and OTSa spread factor curves are overlapped, whereas in the later spreading stages, when rim decelerates down to zero velocity, wettability starts influencing drop dynamics evolution [47].

6.7 Rebound time on SHS

A further important characteristic time is drop rebound time, in case rebound occurs. Among all tested surfaces, complete rebound was observed for all We only for SHS-Teflon surface. Complete rebound was observed also on Teflon in the We range $40 < We < 200$, whereas partial rebound was observed on SHS-Zonyl-a and SHS-Zonyl-b. With regards to Teflon sample, the upper limit for rebound coincide with occurrence of splashing (see also Range and Feuellebois[77], where a critical Weber for splashing equal to 300 was measured for a drop impacting on an aluminum with similar roughness $R_a = 0.44$). We believe that the occurrence of splash (with formation of smaller drops) determines drop energy dispersion due to an increase of surface, and consequently surface energy. As such, residual kinetic energy in the drop core is not enough to promote complete rebound of the drop and drop remains stuck to the surface.

The different behavior of SHS is illustrated in Figure 5.12, which include the image sequences of water drops impacting at $V = 1.7 m/s$ ($We = 113$) on SHS-Teflon, SHS-Zonyl-a, and SHS-Zonyl-b. Drop deformation is almost identical in both the advancing and the recoiling phases, until $t = 14.9 ms$. After that, a clear difference is seen: drop rebounds on SHS-Teflon, whereas it remains stuck on SHS-Zonyl-a and SHS-Zonyl-b. The explanation for this difference has to be found in wetting state transition. On SHS-Teflon, liquid drop remains in a Cassie-Baxter state, in which liquid lays on the solid and on air pockets, that are trapped below the liquid, inside surface crevices. On SHS-Zonyl-a and SHS-Zonyl-b, which have similar contact angles and slightly higher surface roughness (see Table 5.1), the impact pressure likely causes a transition to Wenzel state, in which liquid penetrates inside the surface crevices and the superhydrophobicity vanishes. Two other clues support the idea of wetting state transition: firstly, drop that impacted on the surface were more difficult to remove from the surface than gently deposited drops (through surface tilting or airflow), i.e. impacting drops appear to have reduced mobility than deposited drops. Secondly, visual inspection of an impacting drop and a deposited drop from the top, showed light diffraction at the surface/liquid interface appeared differently, which was likely due to water penetration in vapor pockets. Apparently, roughness standard measurements (R_a and R_q) are not valid criteria to determine whether a drop would rebound or not: SHS-Teflon and SHS-Zonyl-a have similar roughness, but drop rebounds only on the first surface. Some studies in literature [78, 79, 80, 81, 82] have investigated the transition from Cassie-Baxter to Wenzel state in the specific case of drop impacting on specific SHS, micro patterned with pillars. However, the extension of such results on random patterned SHS is not trivial; understanding drop impalement on a SHS goes beyond the aim of the present study.

An important observation from experimental tests is that all above mentioned surfaces, were partial or complete rebound occurs (OTSa, OTSb, Teflon, SHS-Zonyl-a, SHS-Zonyl-b and SHS-Teflon) are characterized by a

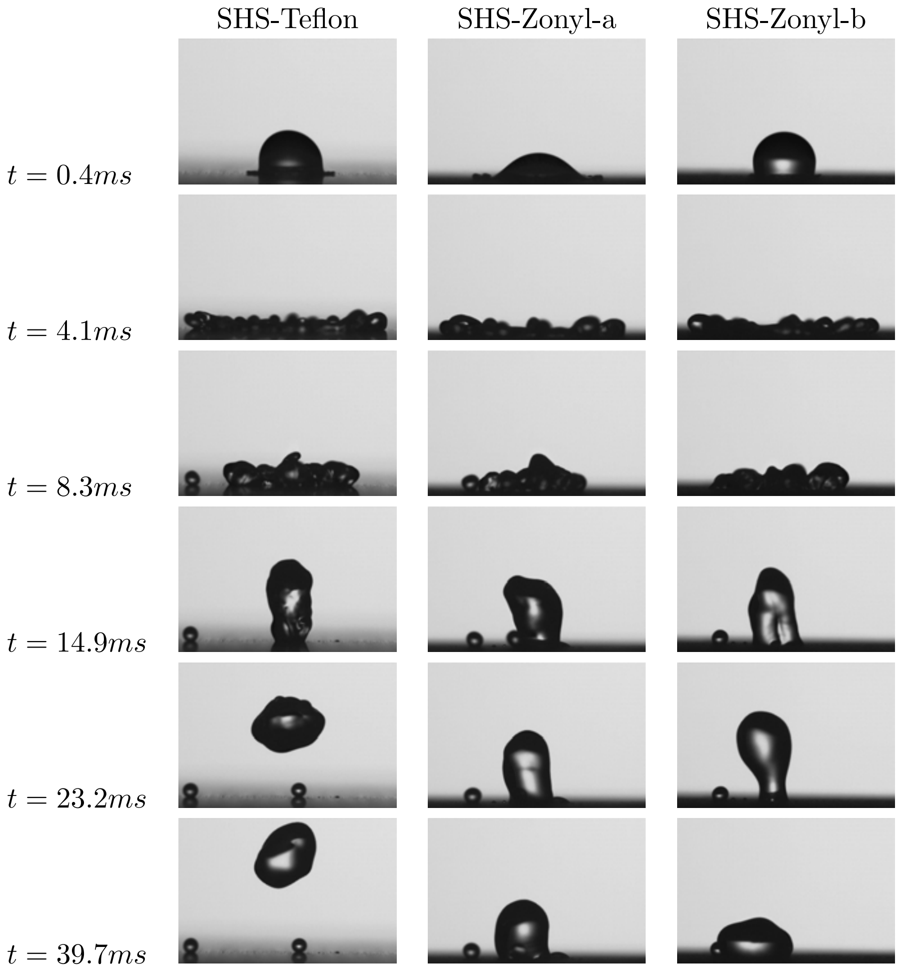

Figure 6.10: Image sequence of water drop impacting on different SHS ($D = 2.86mm$, $V = 1.70m/s$, $We = 113$, $t_{conv} = D/V = 1.7ms$). Surfaces are SHS-Teflon (left column), SHS-Zonyl-a (center) and SHS-Zonyl-b (right). Water drop rebound occurs only on SHS-Teflon.

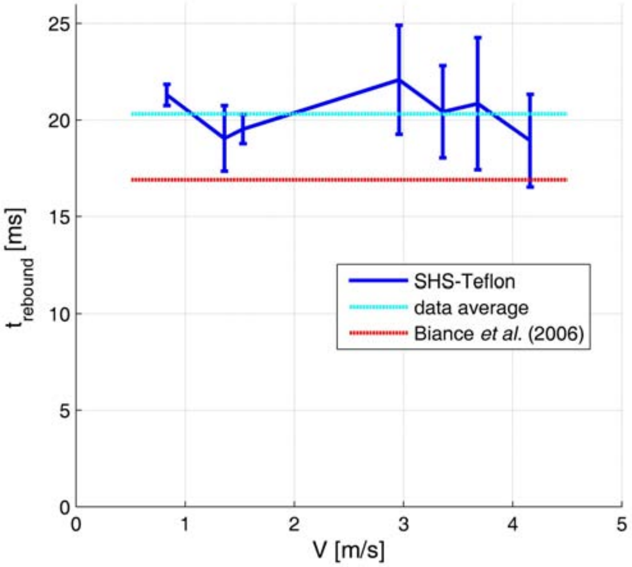

Figure 6.11: Rebound time, $t_{rebound}$, versus impact speed, V, for drop impacts on SHS-Teflon. Data are compared to prediction from [56]. The corresponding range for the x-axis of in terms of We is $25 < We < 680$.

receding contact angle higher than $\sim 100°$: in fact, receding contact angle appear as the dominating wettability parameter, that governs drop recoiling and eventual drop rebound, either partial or complete. Even in the high We regime, inertial effects and capillary effects become comparable in the recoiling phase, since contact line speed, V_{cl}, is not anymore in the order of impact speed, V, as in the initial stages of spreading. For this reason, measurement of receding contact angle is valuable to predict if drop will partially or completely rebound from the surface; nevertheless, particular attention should be paid for SHS, because transition to Wenzel state drastically reduces the value of θ_R and may inhibit drop rebound, as can observed in Figure 6.10.

Figure 6.11 illustrates rebound time for SHS-Teflon surface as function of impact speed. Rebound time is constant not only for lower impact speeds (corresponding to moderate We), but in the entire impact velocity range: average rebound time is $20.3ms$. Data confirms qualitatively results from Richard *et al.* [53], in which it was found that drop rebound time is only a function of drop size and not impact velocity for $0.3 < We < 37$. The correlation proposed in [53] (see Equation 4.10) between drop rebound time and drop diameter predicts a rebound time of $16.9ms$ (for $D_0 = 2.86mm$), underestimating drop rebound time by approximately 20%. Nevertheless, it is noteworthy that drop rebound time remains constant even in the high We regime ($We > 280$), though significant break-up of the drop occurs, especially during the recoiling phase.

6.8 Summary

Impact of millimetric water drops was studied for a large range of We number ($25 < We < 680$) for ten surfaces with different wettability characteristics. Results from impact image analysis have shown that two impact regimes can be identified for drop spreading. It was found that for moderate We numbers ($30 < We < 280$ for a 2.86mm drop) drop spreading, i.e. maximum spreading and spreading time, are influenced by both impact conditions (We) and surface wettability, through the value of the advancing contact angle, θ_A. For high We numbers ($We > 280$), capillary forces become small compared to inertial forces and convection becomes predominant with respect to capillary effects: thus, drop spreading is mainly affected by We number and role of wettability is secondary. Fitting of experimental data allowed to improve existing correlations for drop maximum spread factor [45, 60] with a new one (see Equation (6.2)) and identify a general condition to identify the limit between moderate and high We regime as: $We = 35/Oh^{1/3}$.

Analysis of time evolution of drop spread factor, $\xi(t)$, has pointed out that a different time scaling exist for hydrophilic and hydrophobic surfaces: on a hydrophilic surface all curves of drop spread factor (at different We)

collapse on one single curve if time is scaled by V^a, where $-0.5 < a < -0.4$, suggesting that drop evolution characteristic time scales with $We^{a/2}$; on a SHS, the spread factor evolution in time, $\xi(t)$, is qualitatively different, since characteristic times of drop evolution do not appear to be influenced by impact conditions, in particular impact velocity, for moderate We numbers. Different time scaling can be in terms of system damping, which is caused by a combination of viscous dissipation and capillary effects.

A correlation for drop spreading time, t_s, was also proposed. It was found that contact time at maximum spreading, $\Delta t_{\xi_{max}}$, monotonically decreases with increasing We numbers and decreasing contact angle hysteresis, $\Delta\theta$, in the entire analyzed Weber range. Also, receding contact angle governs drop recoiling phase and is responsible for drop sticking or rebounding (partially or completely) from the surface. Drop rebound either partial or complete can be observed only for receding contact higher than $\sim 100°$.

Differences were found in drop rebound on different SHS. On SHS-Teflon, drop always rebound in the analyzed We range; on the other two SHS surfaces (SHS-Zonyl-a and SHS-Zonyl-b) drop rebound partially in the moderate We range, but not at high We. Lack of drop rebound is attributed to transition from Cassie-Baxter to Wenzel state in the area close to the impact point: due to impact pressure, liquid penetrated inside valleys and surface is locally no more in a non-wetting state. On SHS-Teflon, for which rebound occurs, it was observed that rebound time is not only constant for low impact velocities (corresponding moderate We), but in the entire observed velocity range (up to $4.2 m/s$, corresponding to $We = 680$).

Chapter 7

Drop impact in freezing conditions

7.1 Experimental conditions

For water drop impact in freezing conditions, drop diameter was kept constant at 2.8mm, as for isothermal drop impact tests. The needle was placed at three different heights, to obtain three different impact speeds: 0.7, 1.3 and 2.4m/s, which correspond to Weber numbers equal to 40, 130 and 450, respectively. These We values were chosen because they correspond to moderate, intermediate and high We impact regimes, according to the impact regimes identified in Chapter 6.

Surface temperature was decreased from 5 to -20℃, in 5℃ steps: six different temperatures were tested. Lower values of surface temperature could not be achieved without frost accretion. Drop temperature was kept at 0℃ by dripping water from a needle directly connected with a reservoir, filled with a water-ice mixture.

Drop impact tests were repeated on six different surfaces with different wettability characteristics and different surface effusivity: glass, PMMA, Teflon, SHS-Teflon, copper and aluminum. Surface properties (advancing and receding contact angles and surface roughness) are reported in Table 5.2.

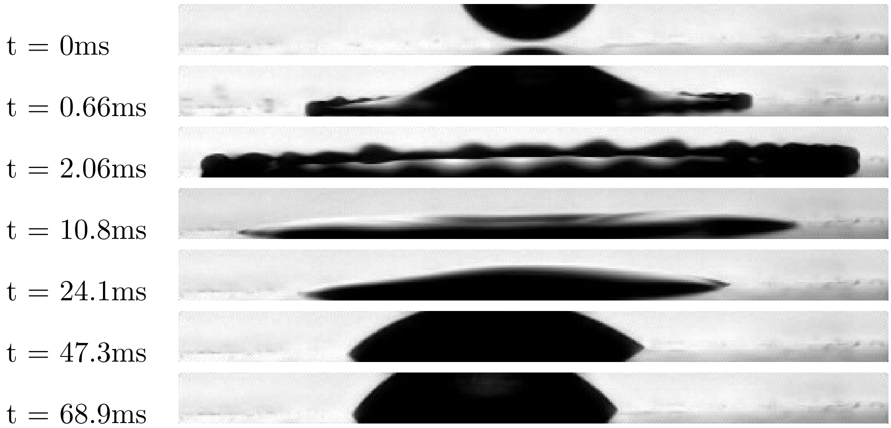

Figure 7.1: Water drop impact on PMMA. Impact conditions: $D = 2.8\text{mm}$, $V = 2.4\text{m/s}$, surface temperature $T_{sur} = -10℃$.

7.2 Impact on PMMA

Figures 7.1, 7.2 and 7.3 illustrate different stages of water drop impact on PMMA, with surface at temperature of -10, -15 and -20℃, respectively. Drop impact speed is 2.4m/s ($We = 450$). Image sequences in Figures 7.1 and 7.2 are identical, showing that surface temperature has no effect on drop impact dynamics, neither during spreading nor during recoiling phase. As one can observe in the two image sequences, the maximum diameter, D_{max}, is the same and is achieved in the same time. Receding of the drop also takes place. No solidification can be observed in the image sequence in Figures 7.1 and 7.2, not even close to the drop-surface contact area.

Drop impact dynamics change when surface temperature is further lowered to -20℃ (see Figure 7.3). Although no differences can be observed during the spreading phase, once the drop has reached its maximum contact diameter, a pinning of the contact line occurs: drop diameter remains constant and no drop recoil is observed. For this impact condition, the absence of drop receding is caused by the presence of small frost crystals

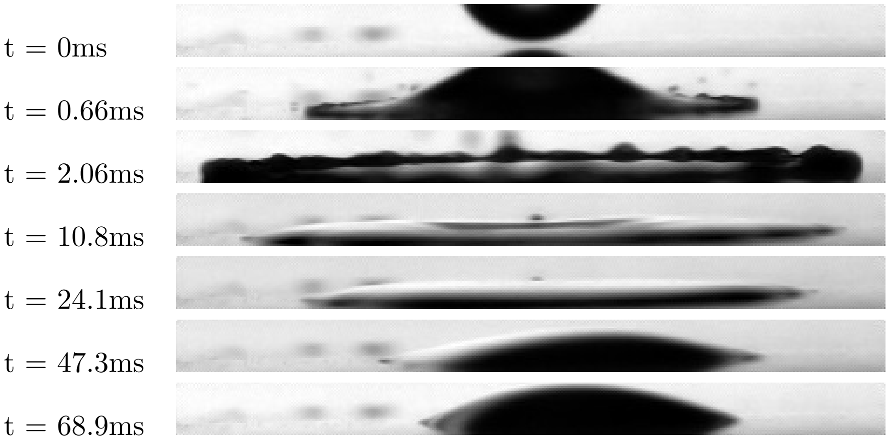

Figure 7.2: Water drop impact on PMMA. Impact conditions: $D = 2.8$mm, $V = 2.4$m/s, surface temperature $T_{sur} = -15$℃.

Figure 7.3: Water drop impact on PMMA. Impact conditions: $D = 2.8$mm, $V = 2.4$m/s, surface temperature $T_{sur} = -20$℃.

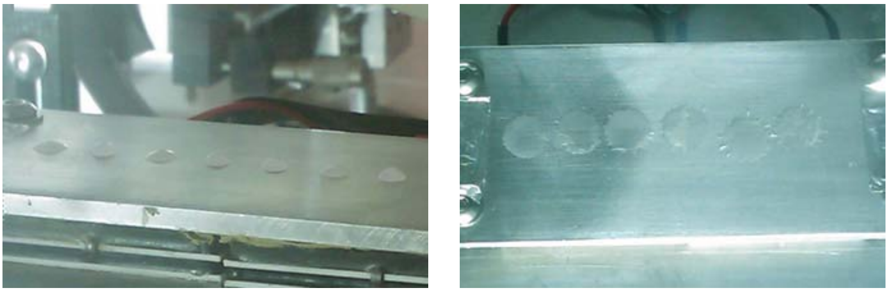

Figure 7.4: Pictures of sessile water drop after impact on PMMA: a) no frost is present on the surface, and solidification occurs several seconds after drop impact; b) frost is present on the surface and drop recoil is inhibited.

on the surface. Indeed, -20°C is the frost temperature at the test condition ($\sim 5\%$ relative humidity at 20°C) and a small quantity of frost, barely visible by naked ice, starts to form on the surface. The presence of such crystals completely modifies the drop impact outcome, because it causes the formation of a small ice layer at the drop-surface interface, which causes pinning of the contact line.

Images in Figure 7.4 further illustrate the differences between drop impacting on frost free and frosted surfaces. Figure 7.4a shows sessile drops, which impacted on a cold ($T < 0$°C) frost free PMMA surface: drop freeze after several seconds, after recoiling has completed. Figure 7.4b shows that, when the surface is frosted, recoil does not occur and final contact area between solidified drop and solid surface corresponds to maximum contact area, reached at the end of the spreading phase.

Another important phenomenon that was observed is drop supercooling. When no frost is present on the surface, it was noticed that it takes up to several seconds before solidification is achieved. This is probably due to drop supercooling. A proof that drop is supercooled is that when liquid drop is sitting on the surface after impact, solidification process can be activated by a small perturbation, for example, by touching the drop: this

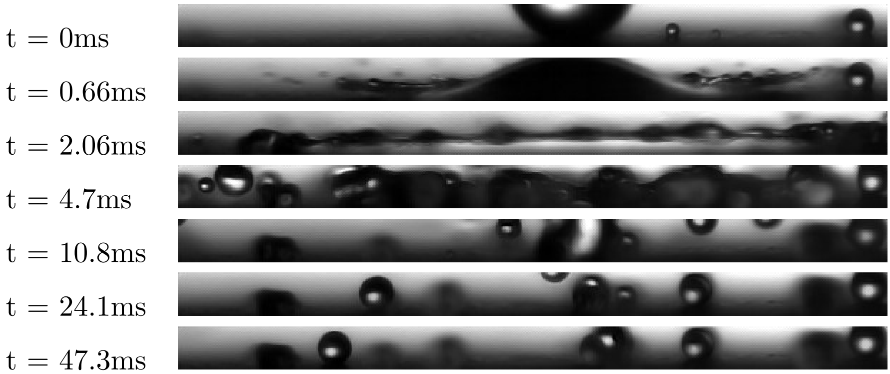

Figure 7.5: Water drop impact on SHS-Teflon. Impact conditions: $D = 2.8\text{mm}$, $V = 2.4\text{m/s}$, surface temperature $T_{sur} = -15$°C.

indicates that the drop is in a metastable system and starts freezing when the system is perturbed. Once solidification starts, the solidification front propagates from the drop-surface contact area to the drop apex.

7.3 Impact on SHS-Teflon

Figure 7.5 illustrates the drop impact sequence on SHS-Teflon with a surface temperature $T_s = -15$°C. As observed for impacts on PMMA, drop dynamics is not affected by surface temperature. No solidification occurs, not even at the drop-surface interface, and the drop core rebounds from the surface after 19.5ms (see Figure 6.11), as during isothermal impacts (see Chapter 6). Also, secondary drops, generated by rim break-up during the initial moments of recoil phase, maintain a high mobility on the surface, and easy roll away or even rebound. When the video recording stops, approximately 100ms after impact, there is still no sign of solidification. The same tests was repeated with a surface temperature $T_s = -19$°C (just above the frost temperature). The image sequence, which was not reported here for brevity, is identical to image sequence in Figure 7.5: drop impact

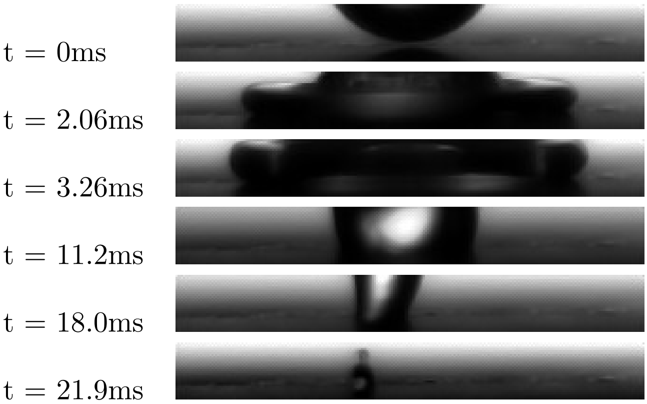

Figure 7.6: Water drop impact on SHS-Teflon. Impact conditions: $D = 2.8$mm, $V = 0.7$m/s, surface temperature $T_{sur} = -20$℃.

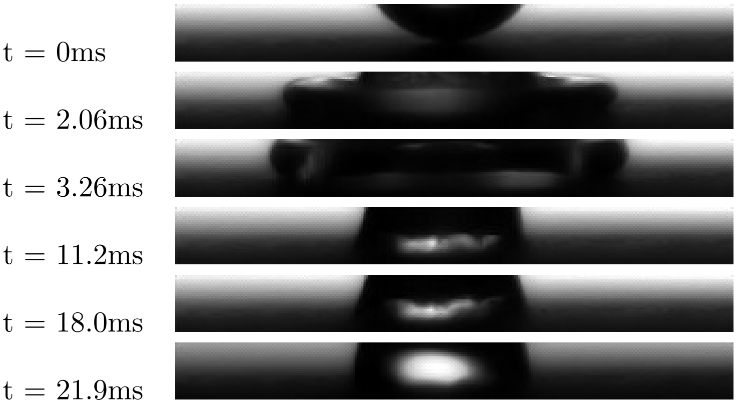

Figure 7.7: Water drop impact on SHS-Teflon. Impact conditions: $D = 2.8$mm, $V = 0.7$m/s, surface temperature $T_{sur} = -25$℃.

Figure 7.8: Frost accretion on SHS-Teflon.

dynamics is again not affected and the drop core rebounds from the surface.

Figures 7.6 and 7.7 show other two tests performed at lower impact speed ($V = 0.7$m/s) at two different surface temperature, T_s, -20°C and -25°C. When $T_s = -20$°C (see Figure 7.6), the drop spreads and recoil as in isothermal impacts. The rebound time, as can be observed in Figure 7.6, is 22ms, a value within rebound time statistics obtained for isothermal impacts. We can thus deduce that surface temperature has no or very little effect on drop dynamics and does not affect rebound. When surface temperature is further lowered to $T_s = -25$°C, below frost temperature, frost starts to form.

Frost presence has a considerable effect on drop impact outcome (see Figure 7.7): after reaching its maximum spreading, recoil phase starts; however, at a certain time ($t \approx 8$ms), drop contact line remains pinned and only partial rebound occurs, because a consistent part of the drop remains attached to the surface. Pinning of the contact line and rebound inhibition can be attributed to frost, which is absent at -20°C and present at -25°C.

It is important to note a difference between hydrophilic surface (as PMMA) and superhydrophobic one (as SHS-Teflon). When frost is present on the surface, drop on PMMA reaches its maximum spreading and does not recoil, i.e. drop contact diameter remains at its maximum value. On a SHS surface, recoil is not completely inhibited and drop partially rebounds from the surface. The explanation for this different behaviors has two bases. First, frost on the surfaces with different wettability has different form: as can be observed in Figure 7.8 shows an image taken some minutes after frost started to accrete on SHS; frost is made of isolated structures, with a fractal structure similar to a tree shape. Such structure are different to typical frost formation on PMMA, where frost is more homogeneous and compact. Second, heat transfer between surface and drop is likely reduced by air pockets, which act as insulating layer and retard the solidification of the liquid layer at the drop-surface interface.

7.4 Other surfaces

Other surfaces (glass, Teflon, copper and aluminum) were tested. High-speed videos (which are not reported here for brevity) confirm that freezing characteristic time are higher than drop dynamics characteristic time and, if no frost is present on the surface, the drop impact outcome is not modified by surface temperature.

One comment should be made on differences between glass and metallic surfaces. Results from different surfaces were similar and no relation between contact temperature (which is a function of surface effusivity) and drop impact solidification, which is only influenced by the presence of frost on the surface, was found. However, an unexpected phenomenon was observed for copper: in some cases, solidification time of the sessile drop after impact were unexpectedly high, in the order of minutes, even higher than that of glass, which has a much lower thermal effusivity (37063 for copper, 1516 for glass). Also, even perturbing the drop (e.g. by airflow), it was possible to move the drop on the surface without making the drop freeze (unlike other surfaces, where perturbation cause the drop to freeze); the moving drop could freeze instantaneously as soon as it came in contact with an already frozen drop. The available information from this test was not sufficient to explain this result, in terms of the considered parameters (roughness, wettability and effusivity); probably, understanding of the phenomenon involves one or more other parameters, which have not been considered here.

Images in Figure 7.9 show sessile drop after impact on copper surface.

a b

Figure 7.9: Images of sessile water drop after impact on copper: a) drop impacting on a frosted surface at $T = -30$°C; b) surface temperature is very close to frost temperature and different outcomes can be observed.

Surface in Figure 7.9a was at a temperature (-30°C) well below the freezing point and the frost point (-16°C for this test): it is apparent that drops do not recoil, as already shown for drops in Figure 7.4b; also, drop upper surface (ice/air interface) show some cracks. Presence of frost on the surface, with temperature well below frost point (in this case, $T_{frost} = -16$°C), likely causes a fast drop solidification: as such, drop does not have enough time to expand while freezing (specific volume of ice is 10% higher than water) and cracks are formed at the end of solidification. Figure 7.9b illustrates how drop impact is linked to local conditions of the surface: when surface temperature is close to frost termperature (in the reported case, $T_s = -13$°C and $T_{frost} = -15$°C), different outcomes can be observed on the surface. One drop (second from right in Figure 7.9b) freezes upon impact and does not recoil, probably because of local formation of frost on the surface; one drop (second from left in Figure 7.9b) recoils, but freezes a few second after impacts; other three drops freeze only after some minutes, as already mentioned above. Also, noi cracks are seen on the drop after freezing.

7.5 Summary

Water drop impact tests in freezing conditions showed that drop spreading and recoiling are not affected by solidification effects, if frost does not form on the surface, irrespective of surface effusivity and wettability. Also, on a superhydrophobic surface, rebound still occurs. However, as soon as frost starts to form, solidification of the liquid drop occurs at the drop/surface interface and contact line remains pinned, once maximum spreading is reached. As such, recoiling is inhibited and complete rebound on superhydrophobic surfaces does not occur: only in in some cases, partial rebound can be observed. This study shows that contact line dynamics is affected by the presence of ice crystal on the surface which accelerates the solidification of liquid water. Additionally, it was observed that frost accretion on a superhydrophobic surface is different than on a hydrophilic surface, i.e. frost develops in a fractal structure, similar to snowflakes; on a hydrophilic surfaces, frost accretes as a more homogeneous layer.

Chapter 8

An engineering perspective: drop impact studies for icing mitigation

In the previous Chapters the differences in spreading and receding after impact of millimetric drops, in isothermal and in freezing conditions, was shown. In the present Chapter the issue of scaling of the problem down to impact of micrometric drops, in the range 20-200µm, which are of interest for icing in aeronautics, is considered.

8.1 Drop impact on aerodynamic surfaces

Table 8.1 shows a relationship between drop size, D_0, and the corresponding maximum normal Weber number, We_N, at different relative wind speeds. Values of We from single drop impact experiments reported in the present study (up to ~ 700) are in the same order of magnitude of We for typical supercooled drops prescribed by FAR (15-40µm) up to 50m/s, whereas We at speed of 100m/s are in the very high We regime, especially for

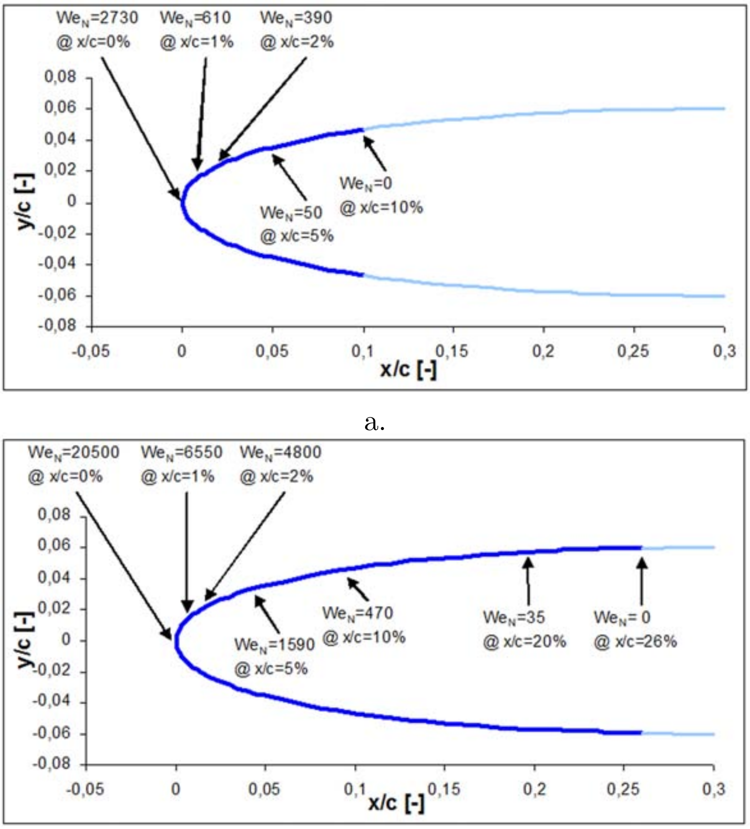

a.

b.

Figure 8.1: Estimation of the normal Weber number, We_N, associated with impacting drops on a NACA0012 profile: a. drop size $D_0 = 20\mu m$; b. drop size $D_0 = 150\mu m$. Assumed speed is $V = 100 m/s$. Blue lines indicate drop collection area. Axes are not equally scaled.

Table 8.1: Correspondence between drop size, D_0, and maximum impact normal Weber number, We_N, at different impact speed, V.

	maximum We_N		
D_0 [µm]	@V=20m/s	@V=50m/s	@V=100m/s
5	28	173	692
15	83	519	2077
40	222	1385	5539
200	1108	6924	27694

SLD (sub-millimetric drops)[1]. However, the values provided in Table 8.1 must be scrutinized carefully: first, the effect of drop deceleration is not considered in the estimation (in other words, the impact speed is lower than the relative wind speed); second, and more importantly, the reported values correspond to the maximum We_N numbers, that are achieved only by drops impacting at the stagnation point. Figure 8.1a and b well illustrate the drop collection region for a NACA0012 for impacting drops with a diameter of 20µm (Figure 8.1a) and 150µm (Figure 8.1b), assuming a relative wind speed of 100m/s. For small drops ($D_0 = 20$µm, Figure 8.1a) the drop collection region is approximately 10% of the chord [1]. It can be observed that normal Weber, We_N, drastically decreases from the stagnation point (0% of the chord) to 1% of the chord by a factor of 4.5 (from 2730 to 610), in consideration of the fact that the drop speed component, normal to the surface, is low even at small distances from the stagnation point. Figure 8.1b shows a very similar trend, with the only difference that the collection region is larger (it extends down to 25% of the chord [1] for the considedered case), due to the increased drop size and inertia, that increase drop collection.

Figure 8.1 provides useful information on the drop impact conditions

---

[1] Preliminary tests at higher Weber number were performed using an innovative drop generator; Weber tests up to 1800 were achieved - see Appendix C.

not only because it allows to relate single drop impact tests to drop impact on aerodynamic surfaces, but also three different zones can be identified in the impact collection zone:

1. the zone close to the stagnation point ($\approx 0 - 2\%$ of the chord), where impacts occur at very high normal We numbers ($We_N > 1000$, order of thousands) and drop splash will likely occur;
2. an intermediate zone (from $\approx 2\%$ to $\approx 5\%$ of the chord), where normal We numbers are high ($200 < We_N < 1000$, order of hundreds), were impact conditions are similar to sigle drop impact test conditions;
3. a third zone (from $\approx 5\%$ to the collection zone limit), where impacts are characterised by low impact angles and normal We numbers are low ($We_N < 200$, order of tens);

In the next section, the result from drop impact studies will be used to understand the outcome from drop impact on aerodynamic surfaces in icing conditions.

8.2 Drop deformation after impact on aerodynamic surfaces

Isothermal drop impact tests reported in Chapter 6 allowed derivation of an empirical correlations for drop maximum spreading, ξ_{max} (see Equation 6.2) and drop spreading time, t_s, (see Equation 6.4). The dependence of ξ_{max} and t_s on drop size, impact speed and surface wettability (through the advancing contact angle, θ_A) are illustrated in Figures 8.2 and 8.3. Figure 8.2 shows ξ_{max} (a) and t_S (b) as function of drop size for different surface wettabilities at fixed impact speed, $V = 20$m/s. The range of drops of aeronautic interest are highlighted in the blue region. Small differences exist between surfaces with different wettability: the Weber range is $83 < We < 1108$ (for $15 < D_0 < 200$µm), so mostly in the high Weber regime, where influence of wettability on drop impact spreading is reduced.

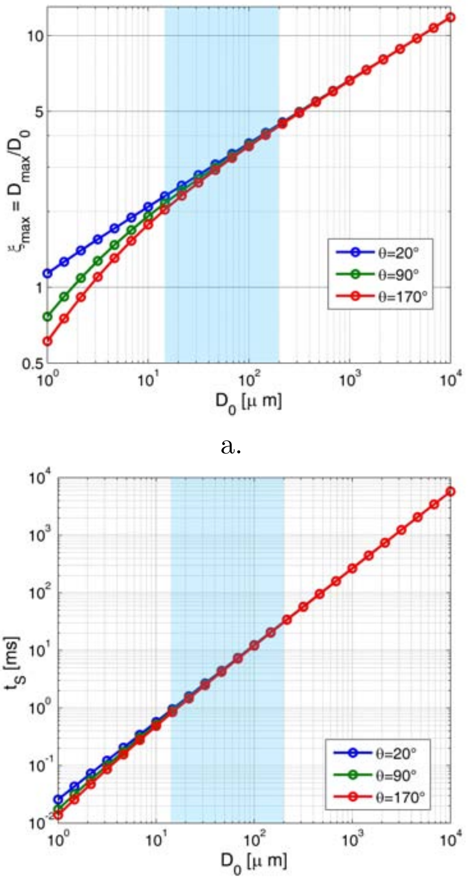

a.

b.

Figure 8.2: Maximum spreading, ξ_{max} (a), and spreading time, t_s (b), as function of drop size, assuming an impact speed of $V_N = 20$m/s. Results were obtained using correlations in Equation 6.2 and 6.4. Lines refer to three different values of surface wettability, indicated in the legend. Blue shadowed area highlights the diameter of interest for aeronautical icing (15 to 200µm).

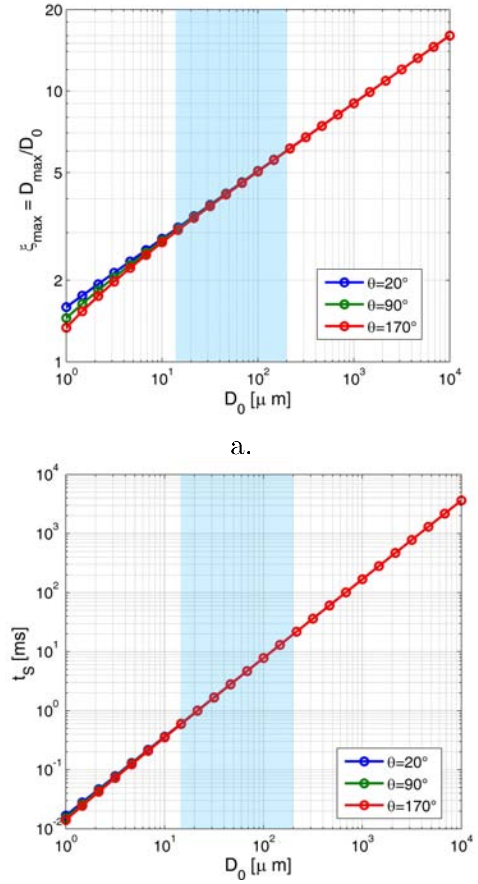

a.

b.

Figure 8.3: Maximum spreading, ξ_{max} (a), and the spreading time, t_s (b), as function of drop size, assuming an impact speed of $V_N = 50$m/s. Results were obtained using correlations in Equation 6.2 and 6.4. Lines refer to three different values of surface wettability, indicated in the legend. Blue shaded area highlights the diameter of interest for aeronautical icing (15 to 200μm).

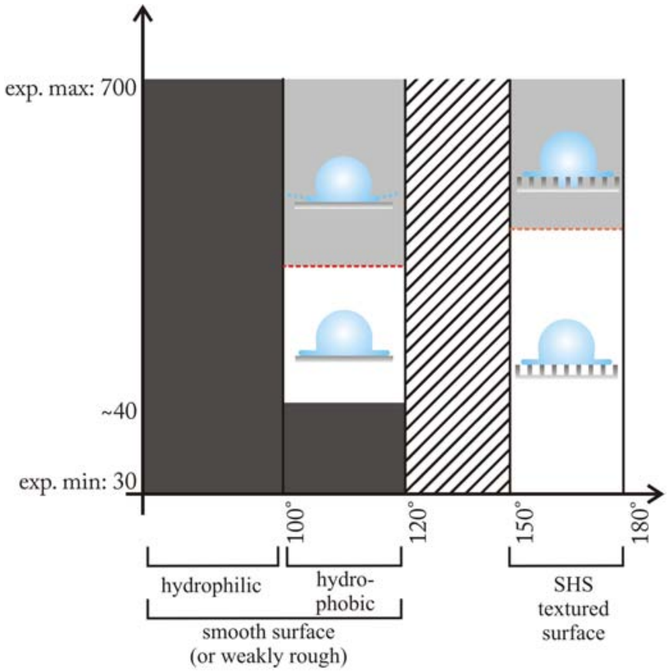

Figure 8.4: Schematic of drop impact rebound map as a function of Weber number, We and receding contact angle, θ_R.

Figure 8.3 is analogue to Figure 8.2, only assuming a higher impact speed, $V = 50\text{m/s}$. The trend is similar and differences between surfaces with different wettabilities are reduced because of the higher We numbers.

However, the difference between different surfaces has to be found especially in the receding phase. As observed in isothermal drop impact studies, when the We numbers become high (order of hundreds), a difference between hydrophilic and hydrophobic surfaces can be observed especially after the drop reaches its maximum spreading: on a hydrophilic surface, drop partially recoils, but if the surface is hydrophobic or superhydrophobic, the recoil is substantial and may even lead to rebound of the drop. In particular, we observed that the dominating parameter to drop deformation evolution after spreading is the receding contact angle, θ_R. In Figure 8.4 a schematic for the drop impact regime map, as function of the Weber number, We, and receding contact angle, θ_R, is shown. If the surface has a contact angle lower than 100°, no rebound can be observed from the surface (dark grey colored region). If the surface is hydrophobic, with $\theta_R > 100°$, the rebound will occur if the drops does not splash on the surface upon impact; in case splash occurs, part of impact energy is converted into surface energy and rebound does not occur. Indeed, some additional tests on a Teflon surface deposited on smooth glass (surface roughness $R_a = 0.17 \pm 0.04$µm) confirmed that, if splash does not occur during drop spreading, drop rebound occurs in the entire investigated We range (up to $We = 700$). To achieve higher contact angles, as already discussed in Chapter 4, textured surfaces must be used: in this case, the drop can achieve a superhydrophobic state, in which receding contact angles are higher than 150°. For a superhydrophobic surface, drop rebound is regulated by resistance to liquid penetration of vapor pockets during impact. If the drops remain in a Cassie-Baxter state, drop will rebound from the surface. Otherwise, if liquid enters the surface cavities (i.e. wetting state changes from Cassie-Baxter to Wenzel), drop rebound will be inhibited.

8.3 Rebound versus solidification time

Another key-point for extending millimetric water drop tests to micrometric drops is relationship between rebound time and the freezing time. An estimation of drop solidification time, based on a simple comparison between the latent heat and convection, is the following:

$$t_{sol,conv} = \frac{m h_{ls}}{h A \Delta T} \approx \frac{\rho 1/6 \pi D_0^3 h_{ls}}{h \pi D_0^2/4 (T_{fr} - T_s)} = \frac{2 \rho D_0 h_{ls}}{3 h (T_f - T_s)} = \kappa D_0 \qquad (8.1)$$

where it appears that solidification time is proportional to drop size. This is helpful to conduct a preliminary comparison between drop rebound and solidification time as function of drop size. In Figure 8.5 blue line represents the solidification time, as given by Equation 4.10 (curve slope in

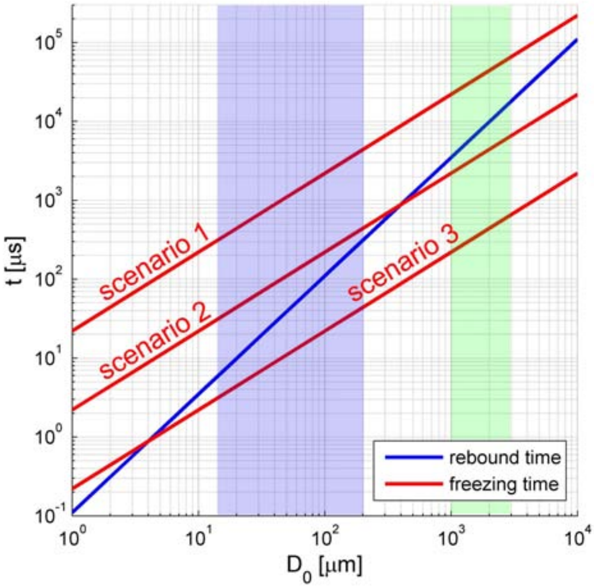

Figure 8.5: Comparison between rebound and solidification (or freezing) time as a function of drop size, D_0. Rebound time is calculated using Equation 4.10 (line slope: 1.5). solidification time is calculated using Equation 8.1 (line slope: 1), assuming different values for the proportional factor, κ.

logarithmic scale: 1.5), and red lines three possible different scenarios for solidification time (curve slope: 1, as indicated in Equation 8.1). According to scenario 1 (see Figure 8.5), drop solidification time is higher than rebound time on the entire drop size spectrum. For scenario 2, solidification time is lower than rebound time for millimetric drops, which are object of experimental studies (green shaded region in Figure 8.5), but is still higher than rebound time in the micrometric drop region (blue shaded area), due to different curve slope. Finally, scenario 3 depicts that solidification time can be lower than rebound time on almost the entire drop size spectrum. Although strong assumptions are made to plot Figure 8.5 (e.g., dependence of impact speed was not considered, although its influence on drop deformation and heat transfer parameters, such as h, the convection coefficient, see Equation 8.1), the graph provides a clear indication: in case millimetric drops will rebound from SHS without freezing, it is likely that result can be extended to micrometric drops (scenario 1). In case drop freezes upon impact without rebounding, micrometric drops may either not freeze (scenario 2) or may freeze, too (scenario 3). In this light, millimetric drops represent an conservative test case to study drop impact behavior in icing conditions, justifying the use of millimetric drops in single impact tests.

Part III

Proof-of-concept: Tests in icing conditions

Chapter 9

Icing wind tunnel facility: icing conditions and materials

9.1 Introduction

In this Part of the thesis the results from performance assessment of superhydrophobic coatings in icing conditions are presented. In Part II attention was focused on understanding the phenomena that govern the dynamic interactions of a water drop impacting on a surface. Part III is more application oriented and is aimed at evaluating the performance of a coating strategy in realistic icing conditions. In the present chapter details on icing wind tunnel facility, experimental conditions and test article are provided. In Chapter 10 results are presented and discussed.

9.2 Experimental setup

9.2.1 Icing Wind Tunnel

Tests were performed in an open loop wind tunnel (see Figure 9.1a), which has a rectangular test section of 254x305mm and a length of 305mm. The air velocity in the test section is 28m/s, corresponding to an air volumetric flow of 2.17 m^3/s. The turbulence intensity is $1.2 - 1.5\%$ in the inner core flow. The test section was made out of acrylic to observe the samples from all directions. To obtain icing conditions, the tunnel was placed inside a cold room (see Figure 9.1b), where the static air temperature was kept constant at $-17°$C (difference between total and static air temperature are negligible, since the Mach number is $Ma = 0.09$). The liquid water cloud was generated using two different nozzle spray systems: the first system generates clouds with a small drop diameter, i.e. a mean volume diameter, MVD, of 50µm and low liquid water content, LWC (1.5g/m^3); such condition corresponds to very severe icing condition (see FAR29, Appendix C – Icing Certification for icing condition requirements for certification); the second system generates a cloud with high MVD (750µm) and high LWC (12.3g/m^3), which is approximately representative of freezing rain condition. Water is supplied by pressurized tank with air at a pressure of 6.9bar. Water drops are sprayed at a temperature of $+2°$C, then they are cooled down by cold air at $-17°$C and reach an estimated temperature of $-2°$C (for 50µm) or 0°C (for 750µm) before impacting on the test sample. Figure 9.2 illustrates schematically the structure of the test apparatus. Various icing regimes, such as rime ice, glaze ice and runback ice (see Figure 9.3), can be obtained in the tunnel by varying test conditions. The duration of icing tests was kept constant at 2 minutes. Table 9.1 summarizes main parameters for the two icing test conditions. The interested reader may find more details in [83].

9.3 Test Article

The test article is a 2D wing with a NACA 0021 symmetric airfoil, placed with a zero angle of attack in the test section. The wing was designed in a modular system consisting of two components: the main body for the wing and an exchangeable insert (see Figure 9.4), made of aluminum sheet (6061-T6, Aircraft Spruce and Specialty Co. Corona, CA). The central part of the main body (149x305mm) was designed to allow insertion of the

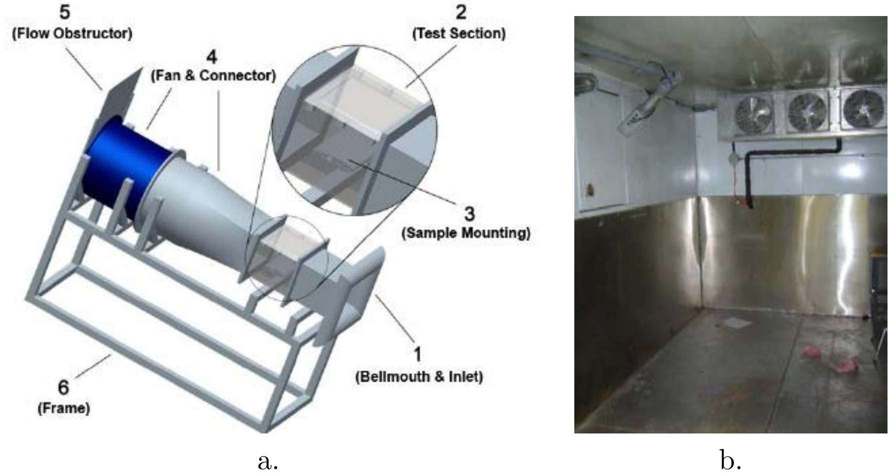

Figure 9.1: (a) Drawing of the open-loop wind tunnel; (b) Picture of the cold room, where the open-loop tunnel was placed during tests.

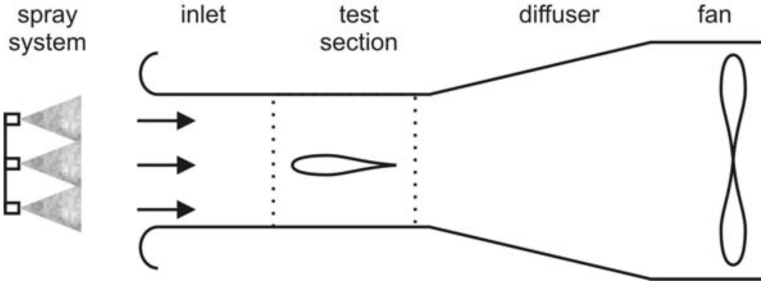

Figure 9.2: Schematic of the open-loop icing wind tunnel (side view)

a. b.

Figure 9.3: (a) Rime ice accretion on the leading edge; (b) glaze ice (area 1) and runback ice (area 2).

Table 9.1: Details of icing test conditions inside the IWT. Note that Mach number is low (Ma=0.09) and the difference between total and static temperature is negligible.

Icing condition	air speed [m/s]	T_{static} [°C]	LWC [g/m^3]	MVD [µm]
low LWC	28	-17	1.5	50
high LWC	28	-17	12.3	750

sample to be tested (79x150mm, i.e. 53% of wing chord and 49% of wing span). The insert is made of 6061 T6 aluminum sheet, which was coated in different ways to achieve different surface wettabilities, as described in the following section.

The exchangeable insert section was instrumented with an electrical resistor positioned at the leading edge on the inner surface (see Figure 9.4), to simulate the presence of an anti-icing/de-icing heating system. The heater power supply was controlled by a PID controller (Watlow®, series 965) to keep the leading edge temperature at the desired value. The presence of a heat source at the leading edge generates a chord-wise temperature gradient on the wing, similarly to an aircraft wing, on which only the leading edge is heated.

To monitor temperature distribution, the exchangeable insert was also instrumented with three K-type thermocouples, mounted chord-wise on the inner surface (see Figure 9.4).

9.4 Coating of exchangeable inserts

Three different inserts were prepared: (i) untreated aluminum; (ii) aluminum coated with PMMA; (iii) etched aluminum coated with Teflon® (DuPont™), labeled as SHS-Teflon (see Chapter 6 for details on surface preparation). For clarity's sake, the wettability properties of the three different coatings used for IWT tests are reported in Table 9.2. The untreated aluminum sample, as received, was the most hydrophilic. The PMMA sample shows similar advancing contact angle to untreated aluminum sample, but lower contact angle hysteresis, $\Delta\theta$. The etched aluminum with Teflon coating is superhydrophobic, showing high θ_A and low $\Delta\theta$.

9.5 Experimental procedure

The test procedure was as following: (1) the cold room temperature was set at -17°C; (2) the wind tunnel fan was started; (3) heating system was switched on and allowed the insert temperature to reach a steady state

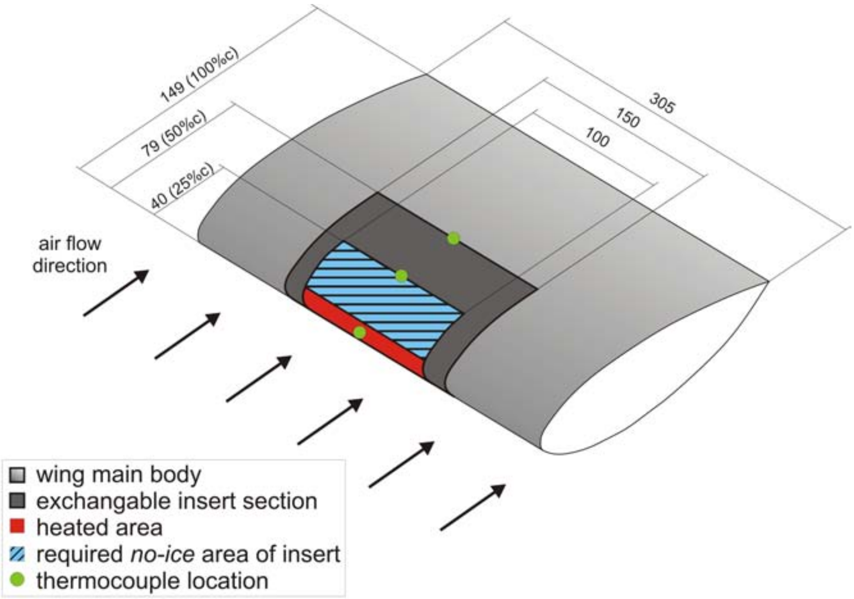

Figure 9.4: Schematic of the wing assembly. The exchangeable inserts are mounted centrally, on the leading edge. Three K-type thermocouples are used to monitor insert temperature. The electrical heater is mounted at the leading edge of the insert, on the internal side of the wing skin. The area to be kept free from ice (no-ice area) is defined as the hatched area from leading edge to 25% of the wing chord, having the same span as the heater. Dimensions are in mm.

Table 9.2: Wetting properties of different coatings for test article. Measurement standard deviation is given.

coating	θ_A [°]	θ_R [°]	$\Delta\theta$ [°]
untreated aluminum	74±1	10±1	64±2
PMMA	74±1	58±1	16±2
SHS-Teflon	161±2	155±2	6±4

condition; (4) spray system was activated to generate liquid water cloud; (5) test were run for two minutes, after which fan and spray system were switched off; and finally (6) pictures of the samples were taken immediately, to record resultant ice accretion. At all times temperatures at various locations of the insert were monitored. The spray cloud inside the test section was not characterized in terms of drop diameter and velocity; only the mean drop diameters produced at the nozzle have been considered.

9.6 Assessment of coating performance

The objective of IWT test was to understand if application of superhydrophobic coating is effective in combating icing. Coating performance can be evaluated by means of two measures: firstly, reduction of power required to heat the leading edge, without the loss of anti-icing performance; secondly, reduction of runback ice.

An objective criterion was needed to define how effective a superhydrophobic coating is, to allow a quantitative comparison among different coatings. The limitation of previous works [23, 32] was that results were mostly qualitative, since no clear quantitative criterion was established to evaluate coating performance. In fact, values of the heating power used in different conditions were reported, but a criterion to establish how required heating power has to be defined was never provided. In the present study, both leading edge temperature and heating power were used as reference parameters. The threshold value for heating power (and the corresponding leading edge temperature) was defined as the heating power that must be provided at the leading edge, to avoid ice accretion on the "no-ice area" (see Figure 9.4). The no-ice area is defined as the area from the leading edge to 25% of the chord length. In other words, if the supplied power is less than the threshold value, ice will accrete on the no-ice area; otherwise, ice will not accrete in the no-ice area.

The threshold for heating power and leading edge temperature were measured for each sample in each icing condition (at low and high LWC, see Table 9.1). For the first test with each sample, the leading edge temperature was set to a first guess value. The PID control system assured that the necessary heating power was supplied, so that the set leading temperature could be reached. After the test, visual observations were made to evaluate if ice had accreted on the no-ice area. If ice accreted on the no-ice area, the test was repeated increasing the set leading edge temperature, and consequently the heating power; if ice did not accrete in the no-ice area, set leading edge temperature was decreased. Tests were repeated iteratively, until the threshold values for leading edge temperature and heating power were identified. Once threshold values were identified, tests were repeated three times to confirm results. After each test, the state of the coating was inspected by conducting simple wetting tests, i.e. to observe how a drop beads on the surface (coating degradation results in lower contact angle, i.e. the airfoil surface becomes more hydrophilic); for a hydrophilic surface (as untreated aluminum) an increase in required heating power would be registered. If any of the coated surfaces showed any unusual wetting behavior or showed unexpected increase in power during repeated tests, it was discarded.

Also, pictures were used to evaluate the presence of runback ice downstream of the no-ice area towards the trailing edge.

Chapter 10

Performance of superhydrophobic coatings in icing wind tunnel

Results from IWT tests are reported in Table 10.1 for both icing conditions, i.e. low and high LWC. Table 10.1 reports the values of heating power that has to be supplied, in order to prevent ice formation in the required no-ice area (see Figure 9.4). The value of temperature at the leading edge of the wing is also recorded.

10.1 Low LWC tests

For low LWC icing conditions, considerable differences between different samples were observed. For the untreated aluminum sample, i.e. the most hydrophilic sample with least drop mobility as signified by highest $\Delta\theta$ (see Table 9.2), a heating power of 171W has to be supplied; the wing leading edge was kept at 50°. Images in Figure 10.1 illustrates ice accretion on the untreated aluminum sample (the required no-ice area is highlighted by a rectangle to guide the eyes). It can be observed that the required no-ice area is mostly free from ice, except some ice beads. Furthermore, runback ice can be observed downstream of the no-ice area, which certainly affects

Table 10.1: Heating power required to avoid ice formation in the no-ice area (defined in Figure 9.4) for the two different icing conditions tested (low and high LWC). Corresponding temperatures measured at the wing leading edge, T_{LE}, are also reported. Experiment details: $V = 28\text{m/s}$, $T_{air} = -17°\text{C}$; test duration was 2 minutes.

coating	low LWC [1.5g/m^3]		high LWC [12.3g/m^3]	
	heating power [W]	T_{LE} [°C]	heating power [W]	T_{LE} [°C]
untreated aluminum	171W±15	50°C	97 W±13	45°C
PMMA	100W±10	40°C	85 W±6	35°C
SHS-Teflon	33 W±11	20°C	87 W±14	25°C

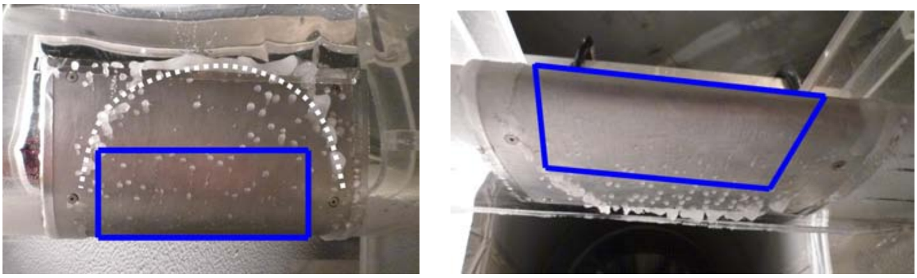
a b

Figure 10.1: Top view (a) and bottom view (b) of the untreated aluminum sample after tests in low LWC icing conditions ($V = 28\text{m/s}$, $T_{air} = -17°\text{C}$; test duration was 2 minutes). Heating power was 171W. Required no-ice area is contoured by rectangles to guide the eyes. Dotted line highlights the point at 0°C on the wing top side (a). 0°C-line has an arc shape because only the central part of the leading edge is heated and a 2D temperature distribution field forms due to spanwise heat conduction.

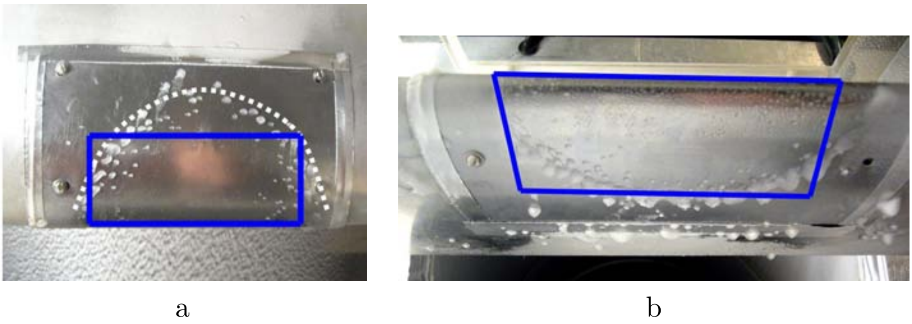
a b

Figure 10.2: Top view (a) and bottom view (b) of the PMMA sample after tests in low LWC icing conditions ($V = 28\text{m/s}$, $T_{air} = -17°\text{C}$; test duration was 2 minutes). Heating power was 100W. Required no-ice area is contoured by rectangles to guide the eyes. Dotted line highlights the point at 0°C on the wing top side (a). 0°C-line has an arc shape because only the central part of the leading edge is heated and a 2D temperature distribution field forms due to spanwise heat conduction.

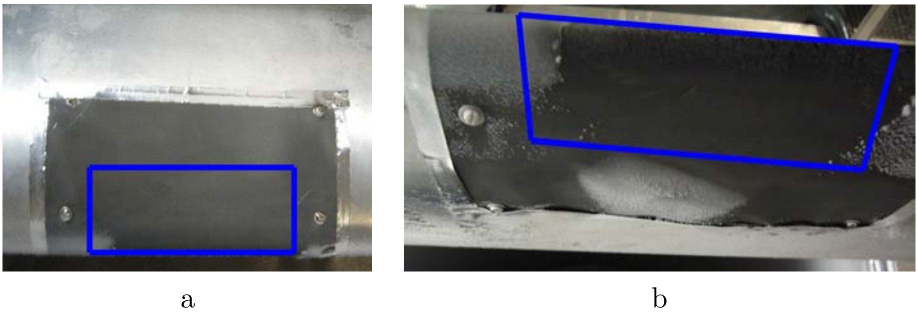
a b

Figure 10.3: Top view (a) and bottom view (b) of the SHS-Teflon sample after tests in low LWC icing conditions ($V = 28\text{m/s}$, $T_{air} = -17°\text{C}$; test duration was 2 minutes). Heating power was 33W. Required no-ice area is contoured by rectangles to guide the eyes.

the aerodynamic performance of the wing. Indeed, ice does not form on the sample in the area close to the leading edge, because the surface temperature is kept well above water freezing temperature (which is 0°C, since tests are performed at atmospheric pressure). However, as drop mobility is reduced on untreated aluminum, aerodynamic drag forces are not sufficient to overcome adhesion force between drops and the surface. As a consequence, liquid water is not shed away from the surface by aerodynamic forces, but flows downstream and freezes in the areas where surface temperature falls below 0°C. The 0°C-line is highlighted in Figure 10.1 by a dotted line (a ridge is formed).

For the PMMA sample (see Figure 10.2) the required heating power is 100W, i.e. a power reduction of 40% compared to the reference untreated aluminum sample. The leading edge temperature is 40°C (leading edge temperature is lower than that of untreated aluminum sample as a consequence of the lower supplied heating power). Higher drop mobility on PMMA, in comparison with untreated aluminum, due to lower contact angle hysteresis (see Table 9.2) corresponds to reduced adhesion between water and surface. Thus, aerodynamic forces are capable of partly overcoming drop adhesion force and of allowing shedding of part of the liquid water from the surface. Also, increased drop mobility reduces the drop residence time on the surface before shedding due to drag forces, thus reducing the probability for drops to freeze on the surface. Nevertheless, ice accretion is not completely eliminated even on PMMA sample; ice still forms as small ice beads, even in the required no ice area (see Figure 10.2), and runback ice is still present, but less compared to untreated aluminum.

For the SHS-Teflon sample (see Figure 10.3) a significant reduction of heating power was found, i.e. only 33W (80% less compared to untreated aluminum). Also, images in Figure 10.3 show that on SHS-Teflon sample ice forms neither in the no-ice area, nor downstream of this area. In other words, not only the no-ice area is free from ice (note a few ice beads were present in the no-ice area for both untreated aluminum and PMMA samples even), but also no runback ice forms, not even downstream 50% of the chord towards the trailing edge, where surface is untreated. A small area where ice formation occurs can be observed on the bottom side of the wing only (Figure 10.3b): however, ice formation in this area is probably due to uneven local surface, which likely caused local flow separation and recirculation. Indeed, a remarkable issue is the complete absence of ice formation on the entire wing, also downstream the SHS-Teflon sample: even if the wing is not entirely coated (SHS-Teflon sample occupies only approximately 50% of the wing chordwise), the whole wing remains free from ice. Absence of ice downstream the heated area is an important clue, suggesting that the presence of a water repellent coating (high contact angles and low contact angle hysteresis, see Table 9.2) in the leading edge area, which corresponds to the water drop collection zone, allows removal of impacting drops by aerodynamic drag forces. Due to reduced adhesion between liquid water drops and surface, impacting drops can also rebound from the surface after impact or, in case some liquid water remains on the surface, drops can easily roll downstream, since the aerodynamic forces easily overcome drop adhesion forces [40]. This is why no liquid water flows downstream towards the trailing edge and no runback ice accretes in the unheated and untreated area: water is shed from the surface immediately after impact and does not have the chance to flow and freeze downstream. As such, it is only necessary to provide a low heating power at the leading edge (in comparison with hydrophilic samples), necessary only to keep the drop collection zone at a temperature above the freezing point, to avoid drop impact freezing upon impact.

The results shown above provide a clear assessment of coating performance. Results suggest that a superhydrophobic coating promotes shedding of most of the liquid water impacting on the surface, so that water can re-enter the external flow quickly, before freezing. On a hydrophilic surface, such as on untreated aluminum or PMMA, water does not freeze in the areas where the surface temperature is kept above the water freezing temperature (0°C at 1atm). However, water flows downstream due to aerodynamic drag and freezes, where temperature falls below the freezing temperature. This phenomenon was clearly observed for both untreated aluminum and PMMA samples. Thus, most of the anti-icing systems (not using a SHS) have to be designed to work as fully evaporative systems, so that liquid water is evaporated in the heated area and no liquid water to flow downstream. Differently, tests on SHS sample showed that the application of a water repellent coating in the area close to the leading edge, where most of drop impact occurs, promotes water shedding from the surface. On a SHS, most of the liquid water is shed from the surface due to drop rebound or due to aerodynamic drag, before liquid water can freeze, and runback ice formation is inhibited. This means that, when the operational requirement in icing condition is to keep the entire wing (or other aerodynamic surfaces, e.g. propellers, engine nacelle, etc.) free from ice, i.e. no runback ice is allowed, the benefit of a water repellent coating would be even higher than the above reported 80% savings in heating power: with 33W heating power input, runback ice does not form at all on the wing, if SHS coating is applied at the leading edge; conversely, 171W heating power input is not sufficient to avoid runback ice on untreated aluminum, and much more heating power would be needed to avoid runback ice, since the anti-icing system should be run as fully evaporative.

10.2 High LWC tests

For high LWC conditions tested (which is not typical of aircraft icing conditions prescribed in FAR29, Appendix C, but anyways interesting from a mechanistic perspective) differences in threshold values for required heating power appear to be not so striking as for the low LWC case (Table 10.1). Differences in terms of heating power between untreated aluminum sample and SHS-Teflon sample are approximately 10%. However, a comparison betwen pictures taken at the end of tests shows that remarkable differences still exist between the hydrophilic untreated aluminum sample (Figure 10.4) and the SHS-Teflon sample (Figure 10.5). On one hand, for untreated aluminum sample (97W supplied) the required no-ice area is not perfectly free from ice and many ice beads close to the leading edge form, as confirmed by the front view of the sample (Figure 10.4). On the other hand, the top side of the SHS-Teflon sample remains much cleaner as no ice accretion is observed (Figure 10.5) when 87W was supplied. Only two small ice structures are observed inside the required no-ice area (top left

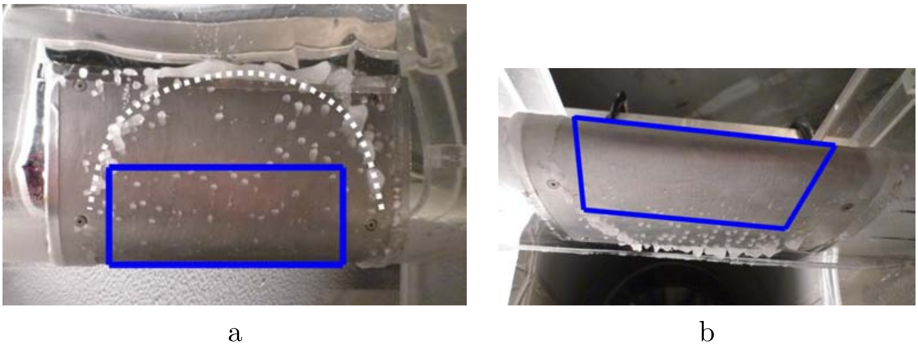

a b

Figure 10.4: Top view (a) and front view (b) of the untreated aluminum sample after tests in high LWC icing conditions ($V = 28$m/s, $T_{air} = -17°$C; test duration was 2 minutes). Heating power was 97W. Required no-ice area is contoured by rectangles to guide the eyes.

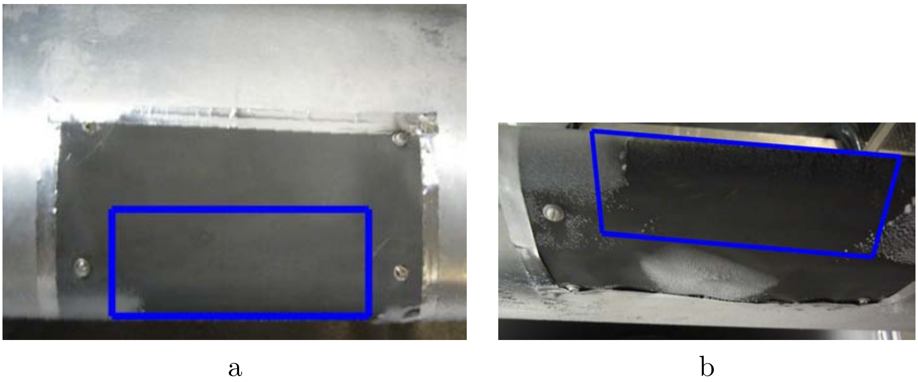

a b

Figure 10.5: Top view (a) and front view (b) of the SHS-Teflon sample after tests in high LWC icing conditions ($V = 28$m/s, $T_{air} = -17°$C; test duration was 2 minutes). Heating power was 87W. Required no-ice area is contoured by rectangles to guide the eyes.

corner of the rectangle in Figure 10.5a), but this ice formation is most likely influenced by ice accretion on the side of the samples, where surface is unheated and uncoated.

A significant accretion of runback ice can be observed on the untreated aluminum sample, whereas runback ice is almost absent downstream of the SHS-Teflon coated area, even in the areas where the wing is uncoated and unheated. As for low LWC test conditions, for high LWC icing conditions the presence of water repellent coating in the drop collection zone promotes water shedding from the surface. Instead of drops sliding slowly downstream, as occurs on a hydrophilic surface, most of the liquid water on a SHS is shed from the surface due to drop rebound after impact or due to aerodynamic drag more rapidly, before liquid water can freeze. Only a small part of water remains on the surface and reach the unheated area. As such, also the uncoated and unheated areas (downstream of the SHS insert) experience significant reduction of ice formation, compared to untreated aluminum sample.

A further important difference between hydrophilic and superhydrophobic samples is the shape and consistency of ice shape. For untreated aluminum sample, ice has typical characteristics of glaze ice, which is transparent and compact (Figure 10.4a). Formation of glaze ice on untreated aluminum sample was expected, because in the tested high LWC condition the MVD is high ($\approx 750\mu m$): drops do not have enough time after injection to reach thermal equilibrium with air (at $-17°C$) and drop temperature remains close to the freezing point. The large drops spread over the airfoil prior to complete freezing, forming a sheet of glaze (clear) ice. On the other hand, ice on the SHS-Teflon sample is more similar to rime ice, which is opaque, milky and rough (Figure 10.5). Ice structures are not compact, as in the case of glaze ice on untreated aluminum sample, but have the shape of isolated ice structures (Figure 10.5a). No specific tests to measure ice adhesion were performed; however, it was observed that the adhesion of isolated ice structures to the surface was relatively low, since they could be removed easily from the surfaces by hands (simply tearing it away from the surface), whereas it was much harder to detach ice formed on a hydrophilic sample, either untreated aluminum or PMMA sample (if ice needed to the removed, a force comparable to a hammer strike was needed. Pictures of PMMA sample in high LWC conditions are not reported for brevity, since results for PMMA sample did not qualitatively differ from results for untreated aluminum sample, reported in Figure 10.4.

10.3 Summary

IWT tests were aimed at understanding the effectiveness of a coating strategy to combat ice formation on surfaces exposed to icing conditions.

Tests in various icing conditions showed that the application of a superhydrophobic coating provide multiple benefits: first, a significant reduction of heating power needed to keep the leading edge of the wing ice free (up to 80% heating power saving); second, a significant reduction (for high LWC condition) or a complete inhibition (for low LWC condition) of runback ice. The effectiveness of mitigation approach is even more clear in icing conditions that can be typically experienced by an aircraft (referred to as low LWC test in the present paper).

Tests provided experimental evidence of the mechanisms proposed in Section 4.3 to explain the effectiveness of a coating strategy in icing conditions: drop rebound and drop shedding by aerodynamic forces. On a SHS, liquid water is removed from the surface before it can flow downstream and freeze in the unheated areas.

As an additional benefit, it was qualitatively observed that ice accretion on SHS was different from ice accretion on hydrophilic surface: isolated ice structures form on a SHS, rather than compact ice, as on hydrophilic surfaces. This result is complementary to observations made during single drop impact experiments in freezing condition (see Chapter 7), where it was seen that frost forming on SHS has a fractal structure (similar to snowflakes); differently, on a hydrophilic surfaces, frost accretes as a more homogeneous layer. This ice characteristics facilitate ice braking and enhance ice removal from the surface, thus suggesting that a coating strategy may be implemented in combination with a de-icing strategy, to make ice removal more effective and increase safety.

Chapter 11

Conclusions and Future Developments

11.1 Achievements of the research activity

The final aim of the research activity in the present thesis was to answer a simple, fundamental question: can superhydrophobicity be an effective strategy against icing?

Two parallel and complementary paths were followed during the research program. On one hand, basic research (see Part II) was performed to better understand the dynamic interaction between water and solid surfaces when water drops impact on a surface, with a particular focus on the effect of surface wettability and of water solidification. On the other hand, applied research (see Part III) allowed to test superhydrophobic surfaces in icing condition, that are representative of atmospheric icing events, which can lead to ice formation on aerodynamic surfaces.

The combination of results from the two research paths were useful to determine how superhydrophobicity can help combating ice accretion on a surface. In particular, two different mechanisms, that can aid in combating ice accretion, were identified and demonstrated: (i) partial or complete rebound of drop upon impact, with drop entrainment in a prevailing airflow; (ii) shedding of sessile drop, which is possible when liquid-surfaces adhesion forces are overcome by external forces (aerodynamic forces or gravity). On a hydrophilic surface, water does not freeze in the areas where the surface temperature is kept above the water freezing temperature, e.g. the leading edge of a wing. However, adhesion forces between liquid and surface are high, the mobility of the liquid on the surface is low and, when water flows downstream due to aerodynamic drag, water freezes where temperature falls below the freezing temperature, causing runback ice formation. Differently, on a superhydrophobic surface, where the adhesion force between liquid and surface is low, most of the liquid water is shed from the surface due to drop rebound or due to aerodynamic drag, which makes water drop to be removed from the surface. In this way, liquid water is removed from the surface before it can flow downstream and freeze in the unheated areas.

It is important to stress that both drop impact studies and icing wind tunnel tests highlighted that the use superhydrophobic coatings represent an icing mitigation strategy, which cannot replace anti-icing and/or de-icing systems. Icing wind tunnel tests showed that ice accretes on all surfaces in icing conditions, if no heating is supplied to the coating, irrespective of surface wettability. Also, drop impact studies in freezing conditions confirmed that a drop can rebound on a surface with temperature below the freezing point only if no frost is present on the surface. Considering that icing events occur in super-saturated conditions (otherwise, water drops would evaporate), as soon as a thin layer of ice (or frost) forms on the surface, the coating is not effective any longer, since impacting drops accumulates on an already iced surface.

Nonetheless, the use of superhydrophobic coatings together with a standard anti-icing system can lead to substantial reduction of ice accretion and increase the energy efficiency of the ice protection system. We showed that superhydrophobic coatings are particularly effective in glaze icing conditions, i.e. when ambient temperature is close to freezing temperature (-5 to 0°C). In glaze icing conditions, release of the latent heat of fusion prevents the impinging drops from freezing on impact. However, liquid drops splash or run back to freeze elsewhere, in unprotected (e.g. unheated) areas. As a result, efficient operation of aerodynamic surfaces typically require that anti-icing systems have to operate as fully-evaporative systems, so that liquid water is evaporated in the heated area and no liquid water flows downstream, to avoid runback ice accretion. If a coating strategy is used, we showed that much less energy is needed, because heating power has to be supplied only to keep the water drop collection zone above the freezing point, and not to provide latent heat, necessary for water evaporation. As a result, ice accretion can be reduced not only in the protected areas, where ice protection system is present, but also in unprotected areas.

11.2 Future developments

The fact that superhydrophobicity was proved as potentially useful for mitigation strategy opens new perspectives for the future technological development for industrial applications.

The major issue to be tackled, which has not been treated in the thesis because it exceededs the scope of the present study, is the durability of the coatings. Most of the superhydrophobic coatings are based on application fluoropolymers for their natural low adhesion to water; however, polymers also show low adhesion to the solid substrate, reducing wear resistance of the coating. Also, a suitable roughness, necessary to achieve a superhydrophobic state, has to be preserved to coating loss of performance.

Aside from improvement of coating resistance, further studies are necessary to develop icing mitigation strategy. A possible research line for the future is the design and optimization of patterned surfaces to control water/surface interaction in the different areas of aerodynamic surfaces. A combination of superhydrophobic to hydrophilic surfaces could be used to “manage” water/surface interaction, on the basis of different surface wettabilities.

Further tests should be performed in different icing conditions, in particular those prescribed by FAR (see Appendix A). Also, coatings should be tested at higher wind velocities and Reynolds numbers, to better represent operating conditions during in-flight icing. The main issue of new experimental tests is the cost of icing tests in bigger icing wind tunnels.

To overcome the high cost due to experimental tests in icing wind tunnel, numerical simulations represent a potentially valid complementary tool for developing an icing mitigation strategy. One of the most critical issues of numerical simulations dependence of models from empirical data, i.e. IWT tests. For this reason, on of the main research target in the next two years will be the development of models for drop impacts on aerodynamic surfaces in icing conditions. The research will be financed by a grant from Lombardy region, “Strumenti innovativi per il progetto di sistemi antighiaccio per l’aeronautica”. Research will be conducted in collaboration with Aerodynamic group from Politecnico di Milano, in order to complement drop impact numerical simulations and experimental tests. Main outcome of the project will be the development of detailed drop impact models, which will be integrated in icing simulation codes, reducing the dependence from empirical correlations and improving relialibility of numerical simulations.

Acknowledgements

Prof. Marco Marengo justly deserves the first thanks. Finding a good master (in the sense of teacher, not of owner!) is a necessary condition to become a good scientist. I cannot say myself if I am now a good scientist, but the condition is definitely fulfilled. Talks and discussions with prof. Marengo have always inspiring and motivating: research is sometimes hard, and working with someone who can help you find the way out is of the utmost importance.

Second on the list is prof. Alidad Amirfazli, co-supervisor of the thesis. Being a visiting student at his laboratory at UofA (University of Alberta) has given me a unique opportunity and has positively oriented the rest of the PhD. His meticulousness in reviewing our papers made me sometimes go crazy, but has definitely taught me how research has to be conducted.

Financial support of Alenia Aermacchi is acknowledged. Discussions with Tiziano Gilardoni, Fabio Brenna, Emanuele Marlo and all other icing engineers have been valuable to focus the research path and achieve good results.

I cannot but heartly thank Cariplo Foundation for its multiple support during these three years. First, for financial support of my experience as vising PhD student at UofA in Canada through the grant “Promuovere la formazione di capitale umano di eccellenza” in 2008. Second, for supporting my application to the Lindau Nobel Laureate Meeting 2010, where I had the

chance to get in contact with 60 Nobel Laureate and 630 brilliant young researchers. None of the experiences would have been possible, without support of Cariplo Foundation.

From a personal point of view, my thoughts go to my wife Ilaria, who gave me her support (the most important one) and even accepted to move to Canada with me and our first baby.

Finally, how can I forget my family, including my parents and parents-in-law? Thanks to them I could start a PhD and get married at the same time, have two babies, buy a house, and so on. Indeed, they also gave a fundamental (financial, and not only) support to research, although not directly, in the usual form of a grant. I hope they will be satisfied by the results, among which this thesis is one of the most important.

List of Publications

International Journals

1. C. Antonini, G. Persico, A.L. Rowe. Prediction of the dynamic response of complex transmission line systems for unsteady pressure measurements. Meas. Sci. Tech., 2008, 19, 125401 (11pp).
2. C. Antonini, F.J. Carmona, E. Pierce, M. Marengo, A. Amirfazli. General Methodology for Evaluating the Adhesion Force of Drops and Bubbles on Solid Surfaces. Langmuir, 2009, 25 (11), 6143-6154.
3. C. Antonini, M. Innocenti, T. Horn, M. Marengo, A. Amirfazli. Understanding the Effects of Superhydrophobic Coatings on Energy Reduction in Anti-Icing Systems. Accepted by Cold Reg. Sci. Technol.
4. M. Marengo, C. Antonini, I.V. Roisman, C. Tropea. Drop collisions with "simple" and complex surfaces. Accepted by Curr. Opin. Colloid In.

Conference proceedings

1. S. Dall'Olio, M. Marengo, S. Zinna, C. Antonini, G.E. Cossali. Description, uncertainty analysis and simulation of a new test rig for

refrigerant two-phase flow characterization. ECI, Heat Transfer and Fluid Flow in Microscale III, Sept. 2008, Canada.

2. C. Antonini, F.J. Carmona, E. Pierce, M. Marengo, A. Amirfazli. New Insights Into The Adhesion Force For Drops And Bubbles On Surfaces. 32nd Annual Meeting of The Adhesion Society, Feb. 2009, Georgia, USA.
3. C. Antonini, M. Marengo, A. Amirfazli. Drop impacts onto cooled solid surfaces: a critical literature review. 13th International Workshop on Atmospheric Icing of Structures, Sept. 2009, Switzerland.
4. M. Innocenti, C. Antonini, M. Marengo, A. Amirfazli. Experimental analysis of the influence of hydrophobicity on icing mitigation. 13th International Workshop on Atmospheric Icing of Structures, September 2009, Switzerland.
5. C. Antonini, M. Marengo. Drop Impact on non-wettable surfaces. 28th UIT Heat Transfer Congress. Brescia, Italy, June 21-23, 2010.
6. C. Antonini, M. Marengo. Statistical analysis of water drop impact on surfaces with variable wettability. 23rd ILASS Europe Conference, Brno, Czech Republic, September 6-8, 2010.

List of Tables

List of Figures

Appendices

Appendix A

FAR for icing certification

This Appendix reports the regulations related to icing certification for 14 CFR parts 25 CFR (Code of Federal Regulation), which rules the airworthiness standard of transport category airplanes.

The requirements for engine inlet certification for operation in icing conditions are stated in FAR 25.1093. The primary concerns are airflow blockage that would reduce engine performance and engine damage due to ingestion of ice. The FAA also requires that areas of the airplane be investigated to determine if ice will accumulate on them and shed into the engine; such areas be protected to prevent ice accumulation and shedding. This requirement is stated in FAR 25.1091(e).

A.1 Sec. 25.1419 Ice protection

If the applicant seeks certification for flight in icing conditions, the airplane must be able to safely operate in the continuous maximum and intermittent maximum icing conditions of appendix C. To establish this:

(a) an analysis must be performed to establish that the ice protection for the various components of the airplane is adequate, taking into account the various airplane operational configurations; and

(b) To verify the ice protection analysis, to check for icing anomalies, and to demonstrate that the ice protection system and its components are effective, the airplane or its components must be flight tested in the various operational configurations, in measured natural atmospheric icing conditions and, as found necessary, by one or more of the following means:

   (1) Laboratory dry air or simulated icing tests, or a combination of both, of the components or models of the components.
   (2) Flight dry air tests of the ice protection system as a whole, or of its individual components.
   (3) Flight tests of the airplane or its components in measured simulated icing conditions.

(c) Caution information, such as an amber caution light or equivalent, must be provided to alert the flight crew when the anti-ice or de-ice system is not functioning normally.

(d) For turbine engine powered airplanes, the ice protection provisions of this section are considered to be applicable primarily to the airframe. For the power plant installation, certain additional provisions of Subpart E of this part may be found applicable.

A.2 Sec. C25.1 Appendix C

(a) *Continuous maximum icing.* The maximum continuous intensity of atmospheric icing conditions (continuous maximum icing) is defined by the variables of the cloud liquid water content, the mean effective diameter of the cloud droplets, the ambient air temperature, and the inter-relationship of these three variables as shown in fig. A.1 of this appendix. The limiting icing envelope in terms of altitude and temperature is given in fig. A.2 of this appendix. The inter-relationship of cloud liquid water content with drop diameter and altitude is determined from fig. A.1 and A.2. The cloud liquid water content for continuous maximum icing conditions of a horizontal extent, other than 17.4 nautical miles, is determined by the value of liquid water content of fig. A.1, multiplied by the appropriate factor from fig. A.2 of this appendix.

(b) *Intermittent maximum icing.* The intermittent maximum intensity of atmospheric icing conditions (intermittent maximum icing) is defined by the variables of the cloud liquid water content, the mean effective diameter of the cloud droplets, the ambient air temperature, and the interrelationship of these three variables as shown in fig. A.2 of this appendix. The limiting icing envelope in terms of altitude and temperature is given in fig. A.2 of this appendix. The inter-relationship of cloud liquid water content with drop diameter and altitude is determined from fig. A.2 and A.2 and 5. The cloud liquid water content for intermittent maximum icing conditions of a horizontal extent, other than 2.6 nautical miles, is determined by the value of cloud liquid water content of fig. A.2 multiplied by the appropriate factor in fig. A.2 of this appendix.

(c) *Takeoff maximum icing.* The maximum intensity of atmospheric icing conditions for takeoff (takeoff maximum icing) is defined by the cloud liquid water content of 0.35g/m^3, the mean effective diameter of the cloud droplets of 20 microns, and the ambient air temperature at ground level of minus 9 degrees Celsius (-9°C). The takeoff maximum icing conditions extend from ground level to a height of 1,500 feet above the level of the takeoff surface.

A.2.1 Part II: Airframe Ice Accretions for Showing Compliance With Subpart B

(a) Ice accretions – General. The most critical ice accretion in terms of airplane performance and handling qualities for each flight phase

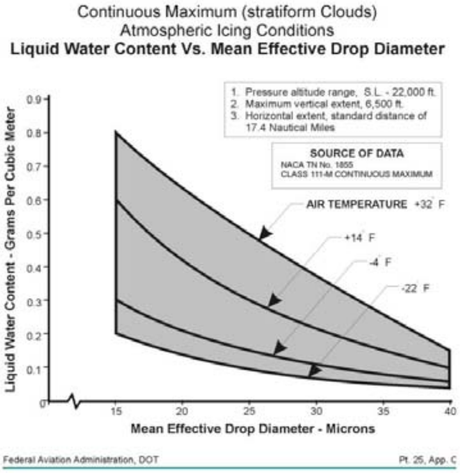

Figure A.1: 14 CFR Parts 25 and 29 Appendix C Continuous Maximum v(Stratiform Clouds) Atmospheric Icing Conditions, Liquid Water Content Vs. Mean Effective Drop Diameter (14 CFR Parts 25 and 29 Appendix C, Figure 1).

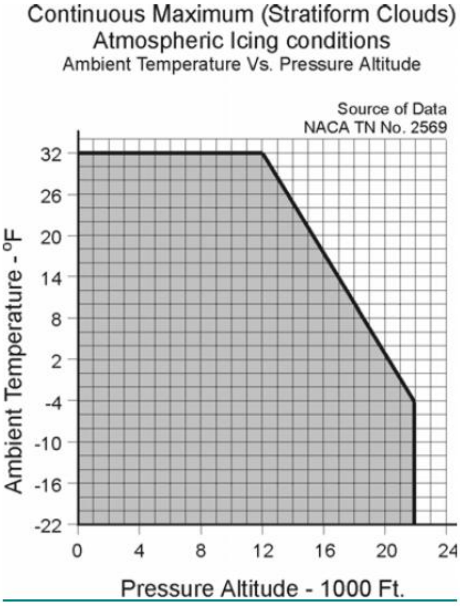

Figure A.2: 14 CFR Parts 25 and 29 Appendix C Continuous Maximum Stratiform Clouds,) Atmospheric Icing Conditions, Ambient Temperature Vs. Pressure Altitude (14 CFR Parts 25 and 29, Appendix C, Figure 2).

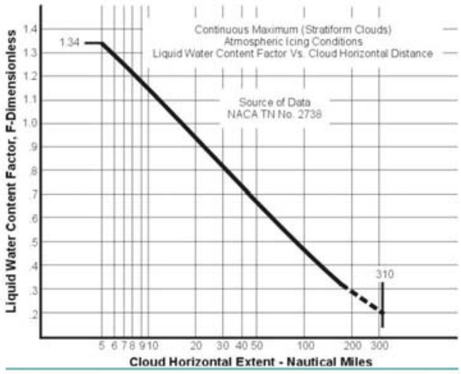

Figure A.3: 14 CFR Parts 25 and 29 Appendix C Continuous Maximum (Stratiform Clouds) Atmospheric Icing Conditions, Liquid Water Content Factor Vs. Cloud Horizontal Distance (14 CFR Parts 25 and 29, Appendix C, Figure 3).

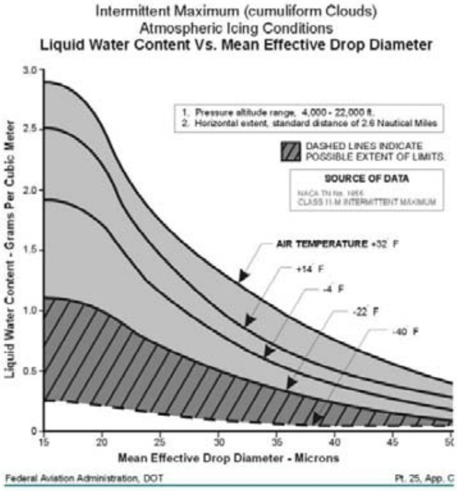

Figure A.4: 14 CFR Parts 25 and 29 Appendix C Intermittent Maximum (Cumulus Clouds) Atmospheric Icing Conditions, Liquid Water Content Vs. Mean Effective Drop Diameter (14 CFR Parts 25 and 29, Appendix C, Figure 4).

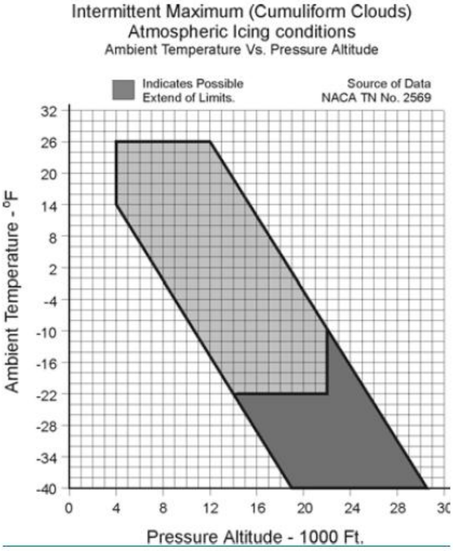

Figure A.5: 14 CFR Parts 25 and 29 Appendix C Intermittent Maximum (Cumulus Clouds) Atmospheric Icing, Ambient Temperature Vs. Pressure Altitude (14 CFR Parts 25 and 29, Appendix C, Figure 5).

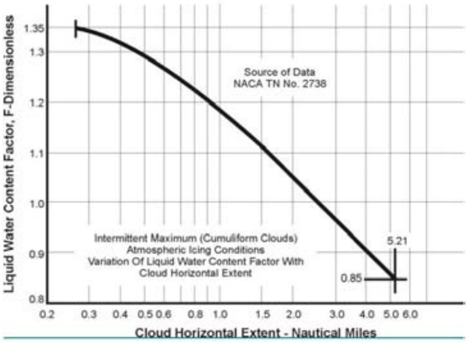

Figure A.6: 14 CFR Parts 25 and 29 Appendix C Intermittent Maximum (Cumulus Clouds) Atmospheric Icing Conditions, Liquid Water Content Factor Vs. Cloud Horizontal Distance (14 CFR Parts 25 and 29, Appendix C, Figure 6).

must be used to show compliance with the applicable airplane performance and handling requirements in icing conditions of subpart B of this part. Applicants must demonstrate that the full range of atmospheric icing conditions specified in part I of this appendix have been considered, including the mean effective drop diameter, liquid water content, and temperature appropriate to the flight conditions (for example, configuration, speed, angle-of-attack, and altitude). The ice accretions for each flight phase are defined as follows:

(1) Takeoff ice is the most critical ice accretion on unprotected surfaces and any ice accretion on the protected surfaces appropriate to normal ice protection system operation, occurring between liftoff and 400 feet above the takeoff surface, assuming accretion starts at liftoff in the takeoff maximum icing conditions of part I, paragraph (c) of this appendix.

(2) Final takeoff ice is the most critical ice accretion on unprotected surfaces, and any ice accretion on the protected surfaces appropriate to normal ice protection system operation, between 400

feet and either 1,500 feet above the takeoff surface, or the height at which the transition from the takeoff to the en route configuration is completed and VFTO is reached, whichever is higher. Ice accretion is assumed to start at liftoff in the takeoff maximum icing conditions of part I, paragraph (c) of this appendix.

(3) En route ice is the critical ice accretion on the unprotected surfaces, and any ice accretion on the protected surfaces appropriate to normal ice protection system operation, during the en route phase.

(4) Holding ice is the critical ice accretion on the unprotected surfaces, and any ice accretion on the protected surfaces appropriate to normal ice protection system operation, during the holding flight phase.

(5) Approach ice is the critical ice accretion on the unprotected surfaces, and any ice accretion on the protected surfaces appropriate to normal ice protection system operation following exit from the holding flight phase and transition to the most critical approach configuration.

(6) Landing ice is the critical ice accretion on the unprotected surfaces, and any ice accretion on the protected surfaces appropriate to normal ice protection system operation following exit from the approach flight phase and transition to the final landing configuration.

(b) In order to reduce the number of ice accretions to be considered when demonstrating compliance with the requirements of Sec. 25.21(g), any of the ice accretions defined in paragraph (a) of this section may be used for any other flight phase if it is shown to be more critical than the specific ice accretion defined for that flight phase. Configuration differences and their effects on ice accretions must be taken into account.

(c) The ice accretion that has the most adverse effect on handling qualities may be used for airplane performance tests provided any difference in performance is conservatively taken into account.

(d) For both unprotected and protected parts, the ice accretion for the takeoff phase may be determined by calculation, assuming the takeoff maximum icing conditions defined in appendix C, and assuming that:

  (1) Airfoils, control surfaces and, if applicable, propellers are free from frost, snow, or ice at the start of the takeoff;
  (2) The ice accretion starts at liftoff;
  (3) The critical ratio of thrust/power-to-weight;
  (4) Failure of the critical engine occurs at VEF; and
  (5) Crew activation of the ice protection system is in accordance with a normal operating procedure provided in the Airplane Flight Manual, except that after beginning the takeoff roll, it must be assumed that the crew takes no action to activate the ice protection system until the airplane is at least 400 feet above the takeoff surface.

(e) The ice accretion before the ice protection system has been activated and is performing its intended function is the critical ice accretion formed on the unprotected and normally protected surfaces before activation and effective operation of the ice protection system in continuous maximum atmospheric icing conditions. This ice accretion only applies in showing compliance to Sec. Sec. 25.143(j) and 25.207(h).]

A.3 Sec. 25.1093 Induction system icing protection

(a) *Reciprocating engines.* Each reciprocating engine air induction system must have means to prevent and eliminate icing. Unless this is done by other means, it must be shown that, in air free of visible moisture at a temperature of 30° F., each airplane with altitude engines using:

(1) Conventional venturi carburetors have a preheater that can provide a heat rise of 120° F. with the engine at 60 percent of maximum continuous power; or

(2) Carburetors tending to reduce the probability of ice formation has a preheater that can provide a heat rise of 100° F. with the engine at 60 percent of maximum continuous power.

(b) *Turbine engines.*

(1) Each turbine engine must operate throughout the flight power range of the engine (including idling), without the accumulation of ice on the engine, inlet system components, or airframe components that would adversely affect engine operation or cause a serious loss of power or thrust *a*) under the icing conditions specified in Appendix C, and *b*) in falling and blowing snow within the limitations established for the airplane for such operation.

(2) Each turbine engine must idle for 30 minutes on the ground, with the air bleed available for engine icing protection at its critical condition, without adverse affect, in an atmosphere that is at a temperature between 15° and 30° F. (between -9° and -1°C) and has a liquid water content not less than 0.3 grams per cubic meter in the form of drops having a mean effective diameter not less than 20 microns, followed by momentary operation at takeoff power or thrust. During the 30 minutes of idle operation, the engine may be run up periodically to a moderate power or thrust setting in a manner acceptable to the Administrator.

(c) *Supercharged reciprocating engines.* For each engine having a supercharger to pressurize the air before it enters the carburetor, the heat rise in the air caused by that supercharging at any altitude may be utilized in determining compliance with paragraph (a) of this section if the heat rise utilized is that which will be available, automatically, for the applicable altitude and operating condition because of supercharging.

Appendix B

A methodology for evaluating the adhesion force on solid surfaces

The material in this Appendix has been already published in [41].

B.1 Introduction

Understanding the incipient motion of a drop adhered to a surface has wide applications, from self-cleaning of superhydrophobic surfaces to electromagnetic drop actuation in microfluidic systems. When a drop is placed on an ideal horizontal surface, its shape is axisymmetric, so that the contact line (three-phase boundary) is circular and the contact angle distribution along the contact line is uniform. If an external force, such as gravity (on tilted surfaces) or aerodynamics (in shear airflows), is applied to such a resting drop, the contact line and/or contact angle distribution along the contact line must distort, if motion is to be resisted. This distortion is responsible for the adhesion force, which keeps the drop attached to the surface in presence of the external force. As such, knowledge of the contact line shape and of the contact angle distribution along the contact line is fundamental to estimate the drop adhesion force. Figure B.1a shows the profile of a drop

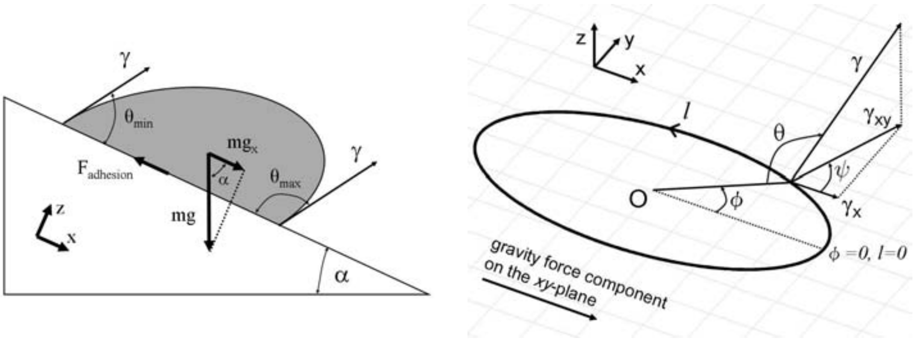

a b

Figure B.1: (a) profile of a drop on a tilted surface. (b) view of the contact line; γ is the surface tension vector, γ_{xy} its projection on the xy-plane, and γ_x its component along the x-direction; θ is the contact angle, ψ the angle normal to the contact line, ϕ the azimuthal angle, and l the curvilinear coordinate along the contact line; O is the origin of the coordinate system. Note that, for a non-circular shape, such as an ellipse, ψ and ϕ are generally not equivalent.

on a tilted surface.

To determine whether the drop will move as a result of an external force, it is necessary to predict the drop adhesion force. The adhesion force is the manifestation of interfacial tension, γ^1, acting at the contact line.

Consider the case of a drop subject to an external force, such as gravity, whose component on the plane of the surface is oriented in the x-direction (see Figure B.1a). In this case, the only component of the adhesion force, which is generally considered, is the one in the x-direction. As a result of this coordinate system convention, the external force component and, therefore, net adhesion force in the y-direction is null, whereas z-direction adhesion force is generally neglected, as drop movement in the z-direction is constrained by the surface. Consider Figure B.1b, at each differential segment of the contact line, dl, the resisting force, dF_x, is given by:

---

[1] To be consistent with symbology of Langmuir, where the material of this Appendix was published [41], the symbol γ was used for surface tension, instead of σ.

$$\mathrm{d}F_x = \gamma_x \,\mathrm{d}l \tag{B.1}$$

where γ_x is as defined in Figure B.1b. Note that γ_x is a function of both the local contact line normal, ψ, and the contact angle, θ (see Figure B.1b). By integrating Equation B.1 over the entire contact line, it is possible to calculate the force of adhesion in the x-direction from the surface tension, the contact angle distribution, and the contact line shape and length.

The procedure for adhesion force calculation can also be extended to bubbles attached to solid surfaces. The present paper focuses on drops, as they have been the subject of experimentation. However, it is important to underline that the following discussion and the proposed methodology applies equally to bubbles. Indeed, the physical mechanism that keeps a bubble attached to a solid surface is similarly due to surface tension forces, as for drops.

Previous models to describe the drop adhesion acknowledge the basic principle that the drop shape deformation is important. However, they are generally limited by assumptions for contact line shape and contact angle distribution along the contact line.

With regards to the contact line, different ideal shapes have been used. The first proposed shape was a circular contact line, the same as for a drop sitting on an ideal smooth horizontal surface. Brown [84] assumed a circular contact line for the purposes of his finite element model, which predicted the contact angle distribution of a drop on an inclined surface. A circular contact line was also assumed in the mathematical model of Quéré *et al.* [85], which predicted the volume at which a very small spherical drop would move on an inclined surface. Dussan and Chow [86] developed a mathematical model, based on asymptotic theory, which was not limited to circular contact lines, but was only valid for small contact angle hysteresis. This model was developed to predict the contact line shape and the speed at which the drop moves along the surface when the adhesion force is overcome by the external force. They modelled the contact line as two arc segments, named advancing and receding contact lines, connected by two straight-line segments. Bouteau *et al.* [87] used the same simplified

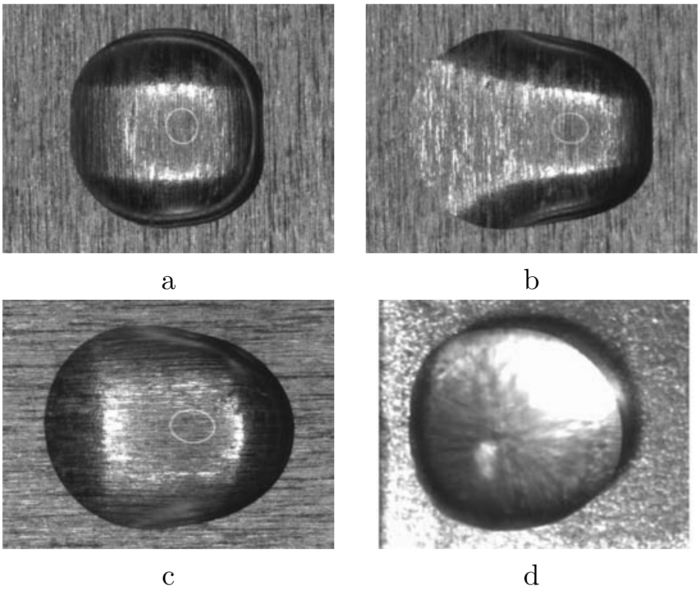

Figure B.2: Four different examples of the contact line shape. Images were recorded from the top of the drop. The view of the contact line was possible as the contact angle is lower than 90°. (a) and (b): a 15μl drop of bromonaphthalene on mill finished aluminum at different inclination of the surface; the external force is gravity; (c): same as (a) and (b), with a different orientation for the surface; (d): a 40μl water drop on PMMA, exposed to an air shear flow. The direction of the external force is from left to right in all cases.

contact line model to investigate the critical sliding angle of a drop placed on a surface. In [87], for the system studied, it was concluded that the "parallel-sided elongated drop" provided a better agreement with experimental observations than that of elliptical or circular contact line models for the systems studied, except for the highest values of the contact angle hysteresis. However, the results indicates that as it stands the current contact line models are too specific for a general system (e.g. the drops in Figure B.2) and there is a need for developing a more general representation for the contact line. Extrand and Kumagai [88] approximated the contact line of a drop at incipient motion as an ellipse. Using a series of profile images, captured by a camera, which rotated around the drop, ElSherbini and Jacobi [89, 90] observed that a double-ellipse model provided a good approximation for the contact line of a drop at incipient motion. However, they recommended that a single ellipse with an equivalent area leads to similarly good approximation of drop volume and adhesion force for the system studied. Therefore, a single ellipse was used in [89] to represent the contact line.

These simplified models of contact line shape may not always be adequate, especially in experiments involving surfaces with anisotropic topography [91], which is the case for many industrial grade materials. Drops placed on such surfaces often exhibit contact line shapes that are not well represented by a circular or elliptical approximation, as illustrated in Figure B.2.

With regards to mathematical representations of the contact angle distribution along the contact line, different models have been proposed in literature. All the models are based either on the knowledge of the advancing and receding contact angles, or on the maximum and minimum contact angles. The advancing and receding contact angles, θ_A and θ_R, are the contact angles measured on a horizontal surface while expanding and contracting a drop, respectively. The maximum and minimum contact angles, θ_{max} and θ_{min}, are the contact angles measured on a surface inclined to the sliding angle at the leading and trailing edge, respectively. In papers [88, 92], θ_{max} and θ_{min} are assumed to be equal to θ_A and θ_R, respectively. There are however theoretical [93] and experimental [38] arguments that indicate advancing angle may not necessarily be equal to maximum contact angle; these studies similarly indicate that receding contact angle will not be necessarily equivalent to the minimum angle observed even for the same surface-liquid combination.

The simplest proposed model [92] involved dividing the contact line into two sections. Each section is assumed to have a uniform contact angle, one section having the advancing contact angle, θ_A, and one having the receding angle, θ_R. The angles θ_A and θ_R are measured on a level surface while expanding and contracting a drop, respectively. Extrand and Kumagai [88] assumed that the distribution of the contact angle cosine, $\cos\theta$, varies linearly with respect to the azimuthal angle, ϕ (see Figure B.1b), ranging from θ_A to θ_R.

Examining multiple profile images of a drop from different azimuthal orientations, ElSherbini and Jacobi [89, 90] measured the contact angle distribution along the contact line of drops on tilted surfaces. For the systems studied, they concluded that the overall contact angle distribution along the contact line could be described as a function of the contact angles at the trailing and the leading edge of the drop profile, θ_{min} and θ_{max}, on a surface inclined to the sliding angle (see Figure B.1a). Note that θ_{min} and θ_{max} are simultaneously observed when the line of sight for the camera is parallel to the y-direction. In [89] the contact angle distribution, $\theta(\phi)$, or its cosine, $\cos\theta(\phi)$, along the azimuthal angle, ϕ, was found to be adequately expressed as a third-degree polynomial function of θ_{min} and θ_{max}.

In [94] it is shown that the third 3^{rd} order polynomial interpolation is inadequate on micro-grooved surfaces, because the contact angle distribution is not monotonic; the maximum contact angle is found at an azimuthal angle $\phi = 90^\circ$ and not at the leading edge. Therefore, it was necessary to define a case specific and complex contact angle distribution.

If the contact line shape and the contact angle distribution along the contact line are provided, it is possible to calculate the drop adhesion force. The force is computed by integration of the differential force $\mathrm{d}F_x$, defined in Equation B.1. However, a simplified expression can be found in literature. As an example, in [88] the following expression was used:

$$\frac{F_{\mathrm{adh,max}}}{\gamma R} = k\left(\cos\theta_R - \cos\theta_A\right) \tag{B.2}$$

where R is a length scale for the contour of the drop and k is an adjustable parameter based on experimental data. This simplified formulation requires only the knowledge of the receding and advancing contact angle, θ_R and θ_A, respectively. Two remarks can be made for this formulation. First, in light of the findings of [93, 38], Equation B.2 should be redefined as Equation B.3:

$$\frac{F_{\mathrm{adh,max}}}{\gamma R} = k\left(\cos\theta_{min} - \cos\theta_{max}\right) \tag{B.3}$$

because the minimum and maximum contact angles, θ_{min} and θ_{max}, respectively, do not necessarily coincide with the the receding and advancing contact angles, θ_R and θ_A, defined for a drop on a horizontal surface. Secondly, the introduction of the adjustable parameter k is necessary to fit the formulation to experimental data. It should be expected that the adhesion force cannot be adequately represented only by θ_{min} and θ_{max}, since it depends both on the contact line (shape and length) and on the contact angle distribution along the contact line. The advantage of using such a simplified formulation is that the adhesion force can be predicted accurately for a given liquid-surface combination, once k is known for that system. The disadvantage is that an experimental calibration of k is required whenever either the surface or the liquid is changed.

According to a recent study [95], the time a drop rests on a surface may cause a variation of the contact angle distribution and therefore influences the adhesion force. From experiments, the adhesion force is observed to increase with resting time on the order of minutes [95]. The automated apparatus used to capture multiple profile images is capable of recording images in a few seconds. Thus, it can be assumed that drop shape variation, as well as evaporation [38], are negligible for the time needed for image acquisition.

This study proposes a new methodology, IBAFA (Image Based Adhesion Force Analysis), to accurately evaluate the drop adhesion force by recording multiple profile images of a drop. Results show that the proposed methodology allows an accurate reconstruction of both the contact line shape and the contact angle distribution along the contact line. In particular, the application of the IBAFA does not require any assumption for either the contact line shape (e.g. circular or elliptical) or the advancing/-maximum and receding/minimum values that are seen at the moment of incipient motion. In fact, IBAFA can be used to study any drop attached to a surface, and not only to study drops at the condition of incipient motion, when the contact angles values reach the minimum/maximum or advancing/receding limits. As a direct consequence, the adhesion force can be evaluated with a high level of accuracy. The adhesion of bubbles to the walls can be also investigated in a similar way. Furthermore, IBAFA can be a valuable tool in studies similar to [93], where time effect has to be investigated. By recording drop multiple profile images at different time steps, variation of the contact line, of the contact angle distribution along the contact line, and of the adhesion force can be measured and evaluated.

Although the proposed methodology will be discussed in terms of tilted surface experiments, it can be applied to any number of other cases, e.g. the incipient motion of a drop in shear fluid flows. Understanding this phenomenon is significant to applications such as fuel cells [96], aircraft icing [97] and enhanced oil recovery [98]. With regards to bubbles, the bubble adhesion to the solid surface is of interest in studies of heat transfer in multiphase flows and shear-driven flows.

B.2 Adhesion force

Consider a drop subjected to an external force, such as gravity, in a static condition (see Figure B.1a). The only force acting on the drop in the x-direction, aside from the external force, is the adhesion force due to interfacial forces. The shear force between the fluid and the solid will be zero, since there is no motion.

It was found that the original formulation for the drop adhesion force, presented in [84], has been misinterpreted in the literature. The adhesion force is given by the integral of the component of the surface tension force, projected in the external force direction (see Figure B.1b and Equation B.1). In [84], the adhesion force was given only for a drop with a circular contact line as:

$$F_{\text{adhesion}} = F_x = -\gamma \int_0^{2\pi} r \cos\theta(\phi) \cos\phi \, \mathrm{d}\phi \tag{B.4}$$

where γ, ϕ, and $\theta(\phi)$ have been previously defined, and $r = r(\phi)$ describes the contact line. Although Equation B.4 is only valid for drops with circular contact lines, this expression was later presented in [88] and [99], where it was applied to models with elliptical contact line shapes. Recalling that interfacial tension forces are normal to the contact line, Equation B.4 assumes that the normal to the contact line (ψ in Figure B.1b), is equal to the azimuthal angle, ϕ, which is only true for circular contact lines. Furthermore, Equation B.4 implies that the differential segment of the contact line $\mathrm{d}l$ (see Equation B.1) is equal to $r\,\mathrm{d}\phi$, which again is only applicable to circles. For a generic curve, the correct expression for the differential segment length is $\mathrm{d}l = \sqrt{r^2 + r'^2}\,\mathrm{d}\phi$, where r' is the first derivative of r with respect to ϕ.

In [94], Sommers and Jacobi proposed a new formulation for the case of a parallel sided elongated drop. In their new formulation, it is acknowledged that the normal to the contact line, ψ, differs from the azimuthal angle, ϕ. However, in this new formulation the differential length is still calculated as $r\,\mathrm{d}\phi$. Thus, the adhesion force is not evaluated properly. Again taken collectively, the recent results (e.g. [87, 94]) point to a need for a general treatment of the contact line shape to avoid the necessity of defining various case specific contact line models.

For these reasons, the general analytical expression for the adhesion force must be defined as:

$$F_{\text{adhesion}} = F_x = \int_0^{L} \gamma_x \, \mathrm{d}l = -\gamma \int_0^{L} \cos\theta(l) \cos\psi(l) \, \mathrm{d}l \tag{B.5}$$

where L is the total length of the contact line, $\psi(l)$ is a function describing the distribution of the normal to the contact line, and $\theta(l)$ is a function describing the contact angle distribution along the contact line, each being expressed in terms of the curvilinear coordinate l (see Figure B.1b). The l is measured from the leading edge of the contact line (where $l = 0$) in the counter-clockwise direction (see Figure B.1b). The azimuthal angle, ϕ, is often used in literature as the independent variable. To be consistent, Equation (B.5) was reformulated as Equation (B.6) below:

$$F_{\text{adhesion}} = -\gamma \int_0^{2\pi} \cos\theta(\phi) \cos\psi(\phi) \sqrt{r^2 + r'^2}\, \mathrm{d}\phi \tag{B.6}$$

Equation B.6 simplifies to Equation B.4 for circular shapes, since for this case $\psi = \phi$ and $\mathrm{d}l = r\,\mathrm{d}\phi$.

Thus, to compute the adhesion force it is necessary to know: (1) the contact line shape, from which $\psi(\phi)$ is derived, and (2) the contact angle distribution along the contact line, $\theta(\phi)$.

B.3 Perspective error

The methodology proposed in this paper to determine adhesion force of a drop depends on having multiple profile images from different azimuthal positions. As already highlighted in [89], when drop profile images are used, there is a perspective error associated with the identification of the contact point coordinates. The perspective error can be understood with the help of Figure B.3b. In a profile image taken at azimuthal angle ϕ, the camera will not record the "original coordinates" of the contact points (r_ϕ, ϕ), but (r_ω, ω), which are labeled as "recorded coordinates" (see Figure B.3b). The recorded radius, r_ω, is the projection of the original radius, r_ϕ, on the viewing plane of the camera. This perspective error will not be present if the contact line is a circle, as in this particular case $\omega = \phi$, or if the line of sight for the camera is parallel either to the x- or y-directions. To correct the perspective error and find the correct contact point coordinates (r_ϕ, ϕ) from a set of recorded coordinates (r_ω, ω), a mathematical representation of the contact line must be specified. This representation is discussed in Section B.5.1. Simulated experiments were especially useful in quantita-

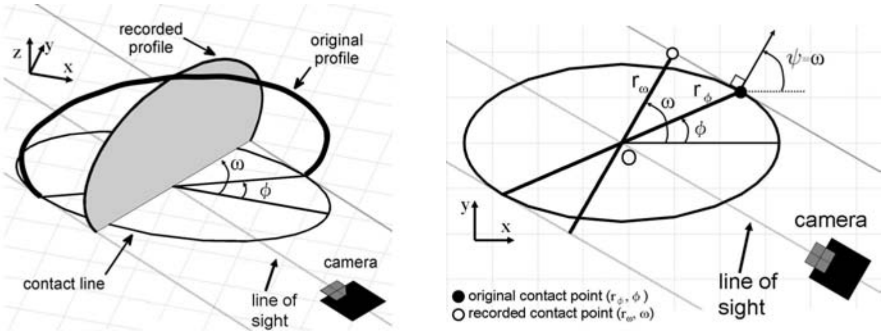

a b

Figure B.3: (a) Profile recorded by the camera (shaded), shown together with the original profile (thick line). The original profile is from the synthetic drop shown in Figure B.5. (b) Top view of the ideal elliptical contact line. Due to perspective error, the contact point coordinates for the recorded profile will be (r_ω, ω), instead of (r_ϕ, ϕ) for the original profile. The coordinate origin is O. Note that, from basic trigonometry, the normal to the contact line, ψ, equals the recorded contact point angular coordinate, ω, for any general contact line; $\phi = \omega$ only for circular contact lines.

tively evaluating the effect of perspective error on the proposed drop shape reconstruction method.

B.4 Methods and Materials

In this study, both experimental and numerical tests were performed. During the experimental tests, images of a drop placed on a tilted surface were recorded by a camera, which rotated 180º around the drop, capturing profile images at 10º intervals and thus obtaining 18 images. The equipment consisted of a custom-built hardware equipped with a rotating camera (A302f, Basler AG) and a 10W halogen light source along with a diffuser for back lighting. To capture top views of the drop, another digital camera (XD700, Sony) was mounted above the drop, so that it tilted with the surface, maintaining a line of sight perpendicular to the surface at all times. Inclination of the stage was measured using a two-axis inclinometer (TSD-90, Instruments & Control Inc.). Both surface inclination and camera rotation were motorized and synchronized with image capture through computer control. To obtain an unobstructed image of the contact line in the top view camera, different surface/liquid combinations were chosen so that the contact angle was never greater than 90°. The surface selections were mill finished aluminum and PMMA, and the liquids bromonaphthalene and water were used. Before use, surfaces were all cleaned using 95% acetone in a sonicrator, dried and rinsed with distilled water. The surfaces were dry before experiments. Drops were placed on horizontal surfaces that were then subsequently tilted. However, the apparatus also allows to place drops on already tilted surfaces.

Simulated experiments with synthetic drops were implemented numerically to further test the capability of the proposed methodology, IBAFA. These simulations avoid the experimental uncertainties and allow the comparison with drop shape models that have known analytical solutions, as the contact line shape and the contact angle distribution can be derived analytically. In addition, synthetic drops with a contact angle greater than 90°provide a more challenging study case, as they may represent drops on

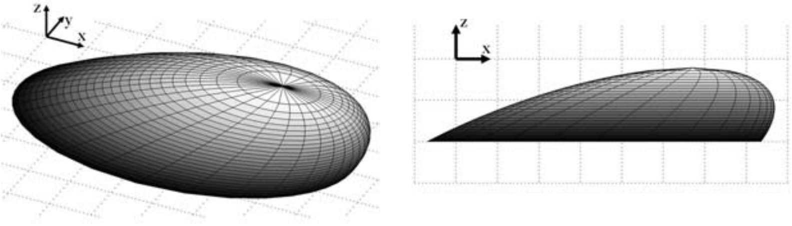

a b

Figure B.4: A x-symmetric synthetic drop, represented by a truncated inclined ellipsoid (semi-axes: $a = 3$, $b = 1.3$, $c = 1$, rotated by 20°around the y-axis). (a) 3D view; (b) profile, as seen on the xz-plane, showing maximum and minimum contact angles.

superhydrophobic surfaces. The simulated experiment approach has been used in various studies, e.g. [100, 101, 102].

As test cases, two different synthetic drops were used: (1) axes-inclined ellipsoids, labeled as x-symmetric drops (see Figure B.4); (2) axes-aligned ellipsoids, labeled as xy-symmetric drops (see Figure B.5). An ellipsoid surface may not necessarily satisfy the Young-Laplace equation, which governs the shape of any liquid-vapor interface. However, this fact does not affect the aim of the present study, that is to evaluate a methodology based on the use of a series of profile images. The critical point is to understand whether the proposed methodology is able to accurately reconstruct the geometry of a 3D shape. Ellipsoids were chosen, because they provide elliptical contact lines, which have been used in the latest studies to fit the experimental drop contact lines [88, 89, 90]; thus, methodologies in literature can be applied to such shapes and their results can be evaluated.

The x-symmetric synthetic drop is representative of drops subject to an external force in the x-direction, e.g. on a tilted surface or in a shear airflow, as they provide a non-zero adhesion force in that direction. An xy-symmetric synthetic drop cannot be practically achieved on a tilted surface, since the total net adhesion force is zero in both x- and y-directions,

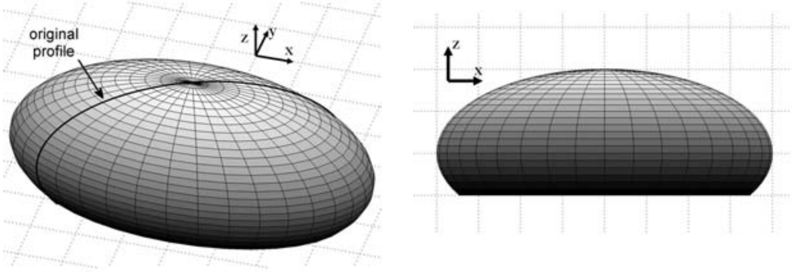

a b

Figure B.5: A xy-symmetric synthetic drop, represented by an ellipsoid truncated in the lower part to simulate drops with high contact angles (semi-axes: $a = 4$, $b = 2$, $c = 2$). (a) 3D view; (b) profile as seen on the xz-plane. In (a) the contour of a generic original profile is highlighted (used is Figure B.3a).

due to symmetry with respect to x- and y-axes. However, it may be of practical interest for drops subject to an external anisotropic external field, such as an electrical field. Using the proposed, generalized representation of the contact line, which is described next, the adhesion force was evaluated from simulated drops with the following geometries: (1) x-symmetric ellipsoid with semi-axes $a = 3$, $b = 1.3$, $c = 1$, rotated by 20°around the y-axis with respect to the canonical orientation; the ellipsoid was truncated by a horizontal plane (see Figure B.4); (2) xy-symmetric ellipsoid with semi-axes $a = 4$, $b = 2$, $c = 2$; the ellipsoid was truncated in the lower part to reproduce contact angles higher than 90°, and to emulate a drop on a hydrophobic surface (see Figure B.5). Simulated experiments were performed for other geometries; however, since the general trend was similar, only results for the above two shapes have been reported here for brevity.

Once the synthetic drop geometry was defined, the image recording process was simulated. Just as a camera records a series of drop profile images by rotating around the drop in an actual experiment, profile images of the synthetic drop were created at different azimuthal angles. The construction of simulated profiles can be understood with the help of Figure B.3a, in which the shape of the xy-symmetric synthetic drop, shown in Figure B.5, was used. At each line of sight for camera, an original profile (thick line in Figure B.3a) was identified. The recorded profile (outline of the shadowed area) was obtained as the projection of the original profile on the plane perpendicular to the line of sight for the camera. The simulation of the camera recording process was necessary to simulate perspective error, which has been described in the previous section.

The profile image series, whether obtained from actual or simulated experiments, were then used to infer a continuous representation of contact line and contact angle distribution. These representations were subsequently used to evaluate the drop adhesion force, as described in Section B.5.

B.5 IBAFA methodology

The procedure for drop adhesion force evaluation can be divided into three steps: (1) the reconstruction of the contact line shape from the measured contact points, whose coordinates have been obtained from a series of profile images; (2) the extraction of the contact angles from the profile images and the determination of the contact angle distribution along the contact line; (3) the calculation of the drop adhesion force, as expressed by Equation B.6.

In the first step, the contact line shape reconstruction was tested both in actual experiments and in simulated experiments. In the experiments, profile images of a drop on a tilted surface were recorded by a camera and analyzed. The radii of the two contact points in each image were extracted (Figure B.6). The x- and y-origins were set to the apex, since it is the only landmark that can be seen from every azimuthal viewing angle.

The procedure was also tested in simulated experiments, which offer the opportunity: (1) to more precisely test the contact line reconstruction method on a variety of pre-defined drop shapes, without experimental limitations; (2) to verify if the perspective error was corrected effectively, i.e. if the corrected contact point coordinates, $(r_{\phi,C}, \phi_C)$, coincide with the original contact point coordinates (r_ϕ, ϕ).

The second step for IBAFA consists of the extraction of the contact

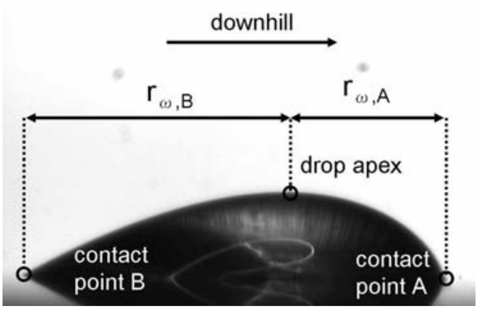

Figure B.6: Example of profile image for a drop on a tilted surface. Note that the camera has been rotated in the same plane as the surface. Note that the camera is positioned with a tilt angle of approximately 1°-2° looking down on to the drop. This is to facilitate automatic identification of the contact point and the measurement of the contact angle from the profile images.

angles from the profile images and the subsequent reconstruction of the contact angle distribution along the contact line. This procedure was tested in simulated experiments using synthetic drops. The advantage of testing the contact angle measurement procedure using synthetic drops is that the drop geometry is defined analytically and is therefore deterministacally known. This is fundamental when it is necessary to evaluate the possible error sources. As an example, the issue of perspective error was carefully analyzed, since in [89, 90] this issue was only partially explored. In the present study, measurement data can be directly compared to the analytical values and the adhesion force error can be exactly calculated, providing a quantitative estimation of perspective error influence on results.

The third step is the calculation of the drop adhesion force. Once the contact line and the contact angle distribution along the contact line are known, the drop adhesion force can be evaluated, according to Equation B.6. Generally, only the force in the x-direction (see Figure B.1a) is of interest, since the net force on the y-direction, F_y, is null. However, since tests were performed on synthetic drops with at least one axis of symmetry, the integration of the forces was computed on one half of the contact line. In this way, F_y will be non-zero and it can be used as an additional information for the evaluation of the methodology. The evaluation of F_y may be of concern for generic non-symmetric drops. Such drops can exist if the surface is irregular or if there is a surface energy gradient that is not aligned with the direction of the surface tilt. In this case, it can be valuable to calculate the F_y to verify if the assumed contact angle distribution correctly estimates a zero force in the y direction.

The forces F_x and F_y are defined as:

$$\frac{F_{x,L/2}}{\gamma} = -\int_0^{\pi} \cos\theta(\phi) \cos\psi(\phi) \sqrt{r^2 + r'^2}\, \mathrm{d}\phi \tag{B.7}$$

$$\frac{F_{y,L/2}}{\gamma} = -\int_0^{\pi} \cos\theta(\phi) \sin\psi(\phi) \sqrt{r^2 + r'^2}\, \mathrm{d}\phi \tag{B.8}$$

where the adhesion forces were normalized with respect to γ in calculations and the subscript $L/2$ recalls that the integration is performed on half of the contact line (i.e. with the azimuthal angle, ϕ, ranging from 0 to π). The adhesion force value from Equation B.6, F_{adhesion}, is twice that of F_x. The numerical discretization of Equations B.7 and B.8 is described in Section B.5.3.

The adhesion force for synthetic drops on tilted surfaces was calculated using four different methodologies: *(i)* assuming a circular contact line shape, $\theta = \theta_{max}$ on the leading half of the contact line and $\theta = \theta_{min}$ on the trailing half; this approach was proposed in [92] for bubbles; considering the F_x, this methodology is also equivalent to the model proposed in [86], where a drop contact line shape was represented by a leading and a trailing circular arc; *(ii)* methodology from [88], assuming an elliptical contact line shape and a linear interpolation for the contact angle cosine distribution, $\cos\theta(\phi)$, given the maximum and minimum contact angle; *(iii)* methodology from [89], assuming an elliptical contact line shape and a third order polynomial relation for the contact angle cosine distribution, $\cos\theta(\phi)$; *(iv)* IBAFA, which reconstructs the drop geometry from a series of profile images without any restrictive assumptions. Results were compared to the benchmark, which was the analytical force derived from the analytical expressions for

Table B.1: Summary of the characteristics of different adhesion force calculation methodologies.

methodology		**contact line**	**contact angle distribution**
(i)	from [92]	circular	leading half θ_{max} and trailing half θ_{min}
(ii)	from [88]	elliptical	$\cos\theta(\phi)$ linear function
(iii)	from [89]	elliptical	$\theta(\phi)$ 3^{rd} order polynomial
(iv)	IBAFA	Fourier series	extracted from profile images

contact line and contact angle from synthetic drops. Table B.1 summarizes the characteristics of each of these methodologies.

This study should be seen as a comparison among different methodologies present in the literature and a novel approach in order to evaluate the adhesion force. In this light, whether or not the Young–Laplace equation is satisfied is a moot point: this further justifies the choice of ellipsoids as numerical test cases.

B.5.1 Contact line shape reconstruction

A top view of the contact line is not always available, as the contact line will be obstructed, wherever the contact angle exceeds 90°. Contact angles well beyond 90º are often encountered in studies of superhydrophobic surfaces [103, 104]. In these situations, the contact line can still be measured, by reconstructing it from a series of drop profile views, recorded by a camera revolving around the drop.

As was described previously, the contact points taken from profile views of the drop must be corrected for perspective error, but this correction requires a mathematical representation of the contact line shape. In [89], this correction was carried out while assuming that the contact line was an ellipse. In IBAFA, a more general representation of the contact line is proposed: a Fourier cosine series. This representation does not require any assumption on the contact line shape, in order to provide an analytical formulation. Thus, the contact line shape can be expressed as:

$$r(\phi) = \sum_{j=0}^{n-1} a_j \cos(j\phi) \tag{B.9}$$

where n is the number of coefficients (a_j) used in the series. In using a cosine series, rather than a full Fourier series, the contact line is assumed to be symmetrical about the x-axis, which is often the case for drops placed on homogeneous surfaces and subject to an external force in the x-direction. The assumption is made to save computational time, but including the sine terms is only a trivial matter.

It should be noted that the Fourier cosine series is a general representation that can be applied to any drop/bubble contact line shape, regardless of the liquid/gas/surface combination. In other words, there is no need to find and tune the most appropriate contact line shape for each specific case, as done in the literature to date. No restricting or case specific assumption for the contact line shape is therefore required.

Fourier cosine series algorithm

Given m points of the contact line and their original coordinates $(r_{\phi,i}, \phi_i)$ (see Figure B.3), it is necessary to find n coefficients a_j, so that the cosine series best fits the data. Mathematically, since $m > n$, this is achieved by specifying an objective function, H, and optimizing it. The chosen objective function was the mean-square deviation between the contact point radius given by the cosine series $r(\phi_i)$ and the correct original contact point radius $r_{\phi,i}$:

$$H(a_j) = \sum_{i=1}^{m} \frac{(r(\phi_i) - r_{\phi,i})^2}{m-1} = \sum_{i=1}^{m} \frac{\left(\displaystyle\sum_{j=0}^{n-1} a_j \cos(j\phi) - r_{\phi,i}\right)^2}{m-1} \tag{B.10}$$

The solution was performed in two ways: with a variable grid search method and by use of the built-in MatLab® (The MathWorks, Inc., USA) function *fmincon*, which finds the constraint minimum of a function, H. Both methods have shown equivalent performance in terms of fitting the points and convergence characteristics.

To improve solution convergence, a convexity constraint was applied, meaning that the fitted contact line representation must be convex at all points. The convexity condition is not a restrictive assumption in practice, as it would not be possible to measure the contact angle or contact point position from a profile image of the drop if the contact line was concave at that point. This condition is mathematically expressed by the curvature $\kappa(\phi)$, which must be positive all along the contact line:

$$\kappa(\phi) = \frac{r^2 + 2r'^2 - rr''}{(r^2 + r'^2)^{3/2}} > 0 \tag{B.11}$$

where:

$$r' = r'(\phi) = \frac{\mathrm{d}r}{\mathrm{d}\phi} = \sum_{j=0}^{n-1} -a_j j \sin(j\phi) \tag{B.12}$$

$$r'' = r''(\phi) = \frac{\mathrm{d}^2 r}{\mathrm{d}\phi^2} = \sum_{j=0}^{n-1} -a_j j^2 \cos(j\phi) \tag{B.13}$$

Several tests were performed both with ellipse and double-ellipse contact line shapes and different aspect ratios. The convexity constraint is particularly useful for highly elongated shapes (e.g. for an ellipse with semi-axes ratio $a/b > 2$), since areas of low curvature are present. If the constraint was not applied, the solution of the contact line reconstruction procedure could converge to incorrect shapes.

Correction of the perspective error

It has been previously discussed that the contact points, (r_ω, ω), recorded from the profile images, are merely a projection of the original contact points, (r_ϕ, ϕ), on the viewing plane (see Figure B.3b); thus, the recorded points must be corrected for perspective error. Figure B.8 shows how the contact line shape of an experimental drop (15μl drop of bromonaphthalene on mill finished aluminum) will be represented, if not corrected for perspective error; the difference is substantial.

Since there are two unknowns $(r_{\phi,i}, \phi_i)$ for each ith recorded contact point, two equations must be defined. One is given by the simple trigonometric relationship (see Figure B.3b):

$$r_\omega = r_\phi \cos(\phi - \omega) \tag{B.14}$$

whereas the second is derived by considering that r_ω should be perpendicular to the line of sight. By expressing the cartesian derivative as a function of polar coordinates, this condition can be written as:

$$-\frac{1}{\tan\omega} = \frac{r + r'\tan\phi}{-r\tan\phi + r'} \left(= \frac{\mathrm{d}y}{\mathrm{d}x}\right) \tag{B.15}$$

where r and r' are given by Equations B.9 and B.12.

Substituting Equation B.14 into B.10, the functional H can be rewritten in terms of the recorded contact points, (r_ω, ω), as:

$$H(a_j, \phi_i) = \sum_{i=1}^{m} \frac{\left(\displaystyle\sum_{j=0}^{n-1} a_j \cos(j\phi) - \frac{r_{\omega,i}}{\cos(\phi - \omega)}\right)^2}{m - 1} \tag{B.16}$$

where it has been made explicit that H is a function of both a_j and ϕ_i for a given recorded contact point, (r_ω, ω). The problem is therefore to find the values of the cosine series coefficients, a_j, and the azimuthal angles, ϕ_i, which minimize the objective function, H, i.e. Equation B.16. This minimization problem is further constrained by Equations B.11 and B.15. Equation B.15 was reformulated as follows for implementation:

$$\frac{\sum_{j=0}^{n-1} a_j \cos(j\phi) + \tan\phi \sum_{j=0}^{n-1} -a_j j \sin(j\phi)}{-\tan\phi \sum_{j=0}^{n-1} a_j \cos(j\phi) + \sum_{j=0}^{n-1} -a_j j \sin(j\phi)} + \frac{1}{\tan\omega} = 0 \tag{B.17}$$

B.5.2 Determination of the contact angle distribution

The contact angle distribution along the contact line for a drop can be constructed from a series of profile images taken from various azimuthal positions. To extract contact angles from individual profile images, polynomial curves were fitted to the drop profile edge. The contact angles were then calculated from the slope of the fitted curves at the contact points. These contact angle measurements were assigned to the corresponding contact points $(r_{\phi,i}, \phi_i)$, which had been previously calculated during the perspective error correction procedure; the result is a discrete contact angle distribution. Particular attention was paid to perspective issues, both in the measurement of the contact angle and in the determination of the contact angle distribution along the contact line.

B.5.3 Numerical discretization of adhesion force

The adhesion forces in the x- and y-direction, defined in Equations B.7 and B.8, were discretized for numerical computation as follows:

$$\frac{F_{x,L/2,\mathrm{num}}}{\gamma} = -\sum_{i=1}^{N_{\mathrm{int}}} \cos\theta_i \cos\psi_i \sqrt{r_i^2 + r_i'^2}\,\mathrm{d}\phi_i \tag{B.18}$$

$$\frac{F_{y,L/2,\mathrm{num}}}{\gamma} = -\sum_{i=1}^{N_{\mathrm{int}}} \cos\theta_i \sin\psi_i \sqrt{r_i^2 + r_i'^2}\,\mathrm{d}\phi_i \tag{B.19}$$

where the summation is done over the N_{int} integration points. Recall that the integration is only performed over half of the contact line, $L/2$. The integration was performed using two different integration step sizes: (1) a coarse integration, where the integration points coincides with the measured contact points, i.e. $N_{\text{int}} = n$; a fine integration, where the number of integration points is higher than that of measured contact points, $N_{\text{int}} > n$.

To perform the integration, one must provide the values of the normal to the contact line, ψ_i, the values of the contact angle, θ_i, the contact radius, r_i, and its derivative, r'_i, associated with the ith integration point. For the coarse integration, the set of ψ_i, θ_i, r_i and r'_i are known, as the integration points coincide with the measured points and are provided by the profile image analysis. For the fine integration, a set of values needs to be interpolated between the measured points. As the contact line is known analytically, through the cosine series representation, the normal ψ, the radius, r_i, and its derivative, r'_i, can be defined in any point. The contact angle distribution along the contact line, $\theta(\phi)$, was found by a piecewise linear interpolation in the interval between the measured contact angles and evaluated at the integration points, to give θ_i.

The results reported in this paper were obtained using 18 profiles and $N_{int} = 181$, i.e. fine integration method was used. These two values were chosen as a compromise between two competing requirements: using as little as possible profile images and obtaining an accurate value for the adhesion force. In the next section, the necessary number of profiles to reach the prescribed accuracy is discussed.

After the image analysis process, the data extracted from the drop profile images are processed in a MatLab program to calculate the adhesion force. The structure of the code is simple and makes use of the built-in MatLab function, so that no particular numerical skills are required to implement the code. Also, the computational effort is not critical: on a typical PC, the data are processed in a few seconds to provide the value of the drop adhesion force.

B.5.4 Minimum number of profiles

For practical applications one needs to determine how many profiles are needed to obtain a evaluation of the adhesion force within a prescribed

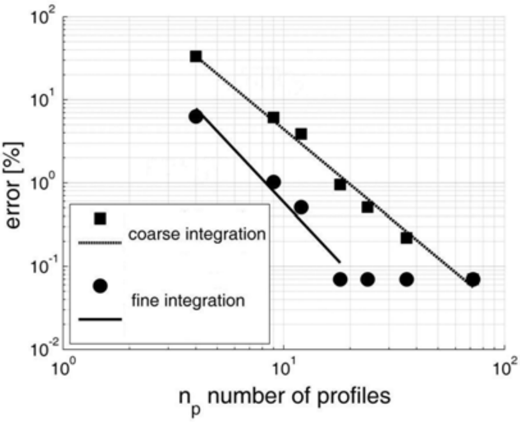

Figure B.7: Error convergence for the drop adhesion force by increasing the numbers of profile images. Simulated experiments were performed on a synthetic drop. The adhesion force was calculated using IBAFA and then compared to the analytical values to evaluate the error. As an example, rotating the camera by 20º intervals over 180º, 9 profile images are obtained. The lines are to guide the eyes.

accuracy. A compromise should be found between two competing requirements: the accuracy of the evaluation and the number of images that can be recorded and analyzed to obtain the information on the contact line and the contact angle distribution.

The error from using the proposed methodology in evaluating the adhesion force of the drop, compared to the analytically derived value, was calculated for different drop shapes, using a variable number of profile images. The adhesion forces was computed according to Equations B.18 and B.19. The calculation was performed using two different integration step sizes, labeled as coarse and fine integration. For the coarse integration, the number of integration points N_{int} was equal to the number of profiles n. For the fine integration, the number of integration points was set equal to 181.

Figure B.7 illustrates the percentage error in the evaluation of the adhesion force, by using a variable number of profiles. Results refer to the

x-symmetric drop (see Figure B.4). As a general trend, an increase of the number of profiles reduces the error, which linearly decreases on a logarithmic scale both for the coarse and for the fine integration. Furthermore, the fine integration provides better results compared to the coarse integration, using the same number of profiles. As an example, by recording 10 images, the error would be approximately 1% for the fine integration and 6% for the coarse integration. Finally, Figure B.7 shows that it is unnecessary to record more than 18 profile images of the drop, if the fine integration is used, as the error would no longer decrease for increasing number of recorded images. When 18 profiles are used, the error reaches a minimum value. This minimum is due to the accuracy in measuring the contact angle from the profile image. As reported in Table B.2, the maximum error in measuring the contact line is 0.3% for a 3^{rd} order polynomial. Due to this limitation in the measurement process, even if the number of profile is increased to over 18, the error cannot be further reduced. For the coarse integration, the minimum error (0.07%) is reached with 70 profiles.

It can be concluded that the fine integration offers much more accurate evaluations than the coarse integration, with a small extra computational effort. Furthermore, from this test and several others, which were not reported here, it was observed approximately 9 profile images (i.e. one image every 20°) can be a good compromise between the necessity of accurate force evaluation ($e \approx 1\%$) and the use of a limited number of profiles. A smaller number of profiles can be used, if a lower accuracy was acceptable.

B.6 Results and Discussions

B.6.1 Reconstruction of the contact line

In this section, the results for the reconstruction of the contact line are reported, to demonstrate the application of the methodology. Results refer to both experiments and simulated experiments.

In Figure B.8, the contact line of an experimental drop was reconstructed using either an ellipse (Figure B.8b) or the cosine series with five coefficients (Figure B.8c). The results show that the cosine series represen-

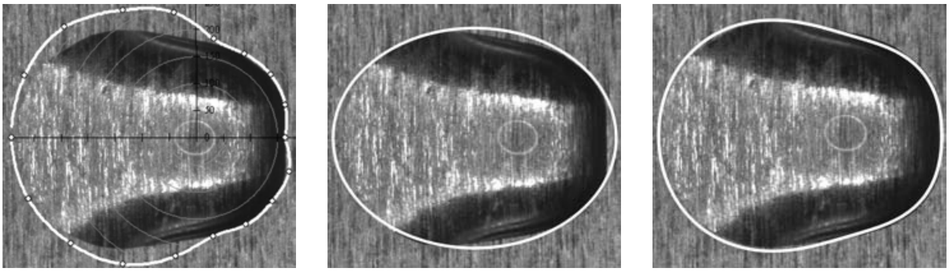

a b c

Figure B.8: Reconstruction of the contact line shape shown in Figure B.2b (15μl drop of bromonaphthalene on mill finished aluminum) from a series of profile images. (a) Comparison between the original contact line shape and recorded contact line points. No correction is applied. Perspective error is not negligible. (b) Elliptical representation. (c) Fourier cosine series representation with five coefficients.

tation is capable of fitting the original contact line more accurately than the elliptical approximation, which is the most current method in the literature.

The methodology was also tested with simulated experiments on analytically known contact lines. As an example, the reconstruction of a double-ellipse contact line shape (as suggested in [89]) is shown in Figure B.9 (semi-axes: vertical $b = 2$, horizontal $a_{x<0} = 4$, $a_{x>0} = 1$). Results were obtained using 24 points, which represent the result of 12 profile images (each profile image provides two contact point radii). From the recorded coordinates, both the overall shape of the contact line and the corrected position of the contact points $(r_{\phi,C}, \phi_C)$ were reconstructed. Figure B.9 shows that the contact line, reconstructed using IBAFA, represents correctly the original points (analytically available), denoted by circles. However, Figure B.9 shows that the reconstructed contact points (crosses), whose coordinates are $(r_{\phi,C}, \phi_C)$, do not all accurately coincide with the the original contact points (circles), with coordinates (r_ϕ, ϕ). This is especially visible in those regions, where the curvature is low. Note that this mismatch does not depend on the use of the cosine series representation. It is generally difficult to correct the perspective error on areas of low curvature, independently from

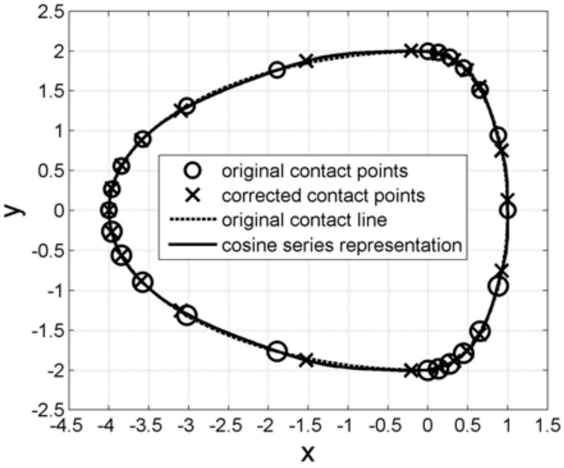

Figure B.9: Reconstruction of a double-ellipse contact line (solid line), which coincides with the analytically defined double-ellipse contact line (dashed line) with semi-axes: vertical $b = 2$, horizontal $a_{x<0} = 4$, $a_{x>0} = 1$. The symbols refer to original contact points (circle), used in simulated measurements, and to contact points corrected for perspective error (crosses). The units are arbitrary.

the chosen mathematical representation. Although corrected contact line points do not agree well with actual contact line points, Figure B.9 clearly indicates that this issue does not significantly affect the representation of the contact line shape since the corrected points all are in good agreement with the analytically constructed contact line. However, the determination of the contact angle distribution associated with these contact points would be misplaced, the possible consequences of which will be discussed in Section B.6.2.

B.6.2 Determination of the contact angle distribution

In this section the results obtained with IBAFA for determination of the contact angle distribution of synthetic drops, for both the xy-symmetric and x-symmetric cases, are presented. The contact angle distribution found using the present methodology is compared to that calculated analytically based on the pre-defined drop geometry.

xy-symmetric drop

Figure B.10 shows a plot of a simulated drop profile near the contact line of the xy-symmetric synthetic drop from Figure B.5. This segment of the profile was fitted with a polynomial, whose derivative at the contact point was then used to determine the contact angle. Each drop profile (dashed line in Figure B.10) consisted of 50 points, of which 10 were used for fitting a polynomial (solid line).

The polynomial fit was assessed in terms of error in resultant contact angle measurements, with respect to the analytical solution. This assessment was carried out for one through fourth order polynomial fits, with the results shown in Figure B.11a. Considering the maximum errors, whose values are reported in Table B.2, and the necessity of keeping the order of the polynomial low, to avoid the possibility of fittings with spurious oscillations, a third order polynomial was deemed suitable, in accordance with [105].

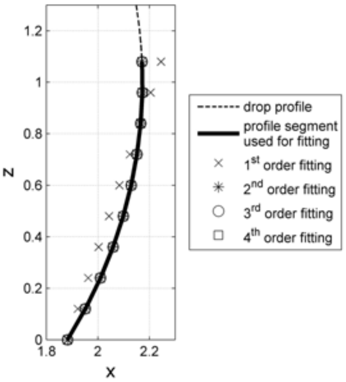

Figure B.10: Profile of a drop with high contact angle, compared to different order polynomial fittings. Close up view near the contact point. The whole drop profile consisted of 50 points, of which 10 were used to fit the polynomials. The units are arbitrary. The directions x and z refer to coordinates as defined in Figure B.1.

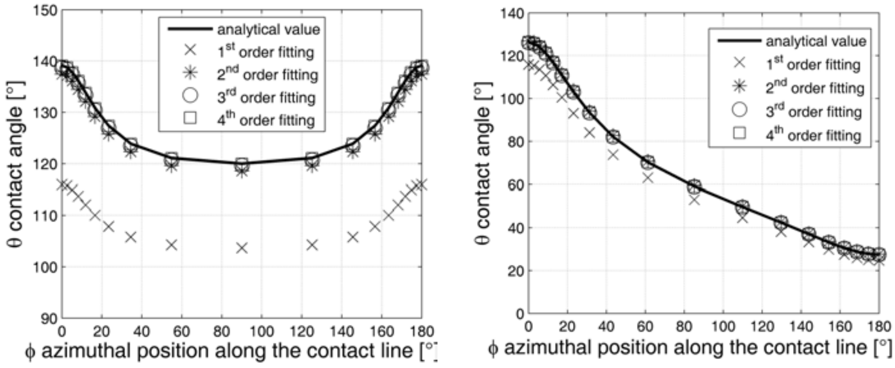

a b

Figure B.11: Determination of the contact angle distribution, using fitted polynomials of different order, compared to the analytical solution, at different contact line azimuthal positions: (a) xy-symmetric drop (see Figure B.5 for geometry details); (b) x-symmetric drop (see Figure B.4 for geometry details).

Table B.2: Maximum error for determining the contact angle. Polynomials of different order were used to approximate the drop profile. The analytical value of the contact angle, derived from the equation of the synthetic drop surface, was used as the benchmark.

	error [%]			
drops	1^{st} order	2^{nd} order	3^{rd} order	4^{th} order
xy-symmetric	16.64	1.21	0.33	0.05
x-symmetric	14.22	0.52	0.16	0.03

x-symmetric drop

The results from the x-symmetric drop from Figure B.4 were similar to those for the xy-symmetric drop. From the results depicted in Figure B.11b, the contact angle is accurately evaluated using a polynomial fitting of at least the third order. The magnitude of error for different polynomial orders are similar to those obtained with the xy-symmetric shape (see Table B.2).

An important result from these simulated experiments is that there is no imaging perspective issue related to the measurement of the contact angle from profile images/views. In other words, the value of the contact angle, that is extracted from a drop profile image, is not affected by perspective error and does not require any correction.

Contact angle distribution

Although there is no perspective issue in the measurement of the contact angle from profile views, as demonstrated by Figures B.11a and b, there may be an error in determining the local contact angle distribution along the contact line. This issue was alluded to in [90], i.e. the correct measured value of the contact angle may be assigned to the wrong position on the contact line.

To understand the above issue, see Figure B.9, which shows the reconstruction of a double-ellipse contact line. Although the overall contact line shape is well evaluated, in some areas there is a mismatch between the reconstructed contact points, whose coordinates are $(r_{\phi,C}, \phi_C)$, and the original contact points, whose coordinates are (r_ϕ, ϕ). This is observed particularly in the areas where the curvature is low. If in the low curvature area the contact angle gradient is low, the error from the contact point re-positioning has a negligible influence. If the contact angle gradient is high, then the drop adhesion force can be evaluated with a higher error.

B.6.3 Force calculation

Once the contact line shape and the contact angle distribution along the contact line are known, it is possible to calculate the force in the x- and y-directions, $F_{x,L/2}$ and $F_{y,L/2}$, respectively (see Equations B.18 and B.19).

Results were obtained with four different methodologies (see Table B.1), for the xy-symmetric and for the x-symmetric synthetic drops. Methodologies *(ii)* and *(iii)* were computed using the analytical contact line, since this coincides with an ellipse. As the contact line is given, the errors due to an inappropriately modeled contact line and for perspective error were both zero. Thus, it was possible to independently estimate the error due to the simplifying assumptions for the contact angle distribution (e.g. $\cos\theta(\phi)$ as linear or third-order polynomial function).

xy-symmetric drop

The methodologies *(i)*, *(ii)*, and *(iii)* all assume that a single profile image can provide the maximum and minimum contact angles, i.e. they can be found at the azimuthal angles $\phi = 0°$and $\phi = 180°$, respectively. This is not the case for the xy-symmetric drop, where maximum and minimum contact angles are found at $\phi = 0°$and $\phi = 90°$, respectively. Therefore, θ_{max} and θ_{min} must be extracted from two different images in practice. If a single image is used, it will appear that the contact angle is the same at $\phi = 0°$and $\phi = 180°$(see Figure B.5) and it will be concluded that the contact angle is uniform along the contact line. However, a uniform distribution of the contact angle along the contact line is not adequate to represent the correct distribution.

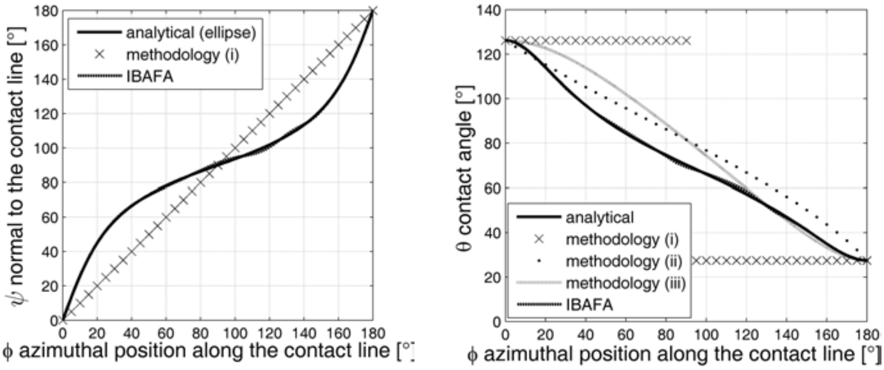

a b

Figure B.12: Distribution of geometrical properties along the contact line for the x-symmetric synthetic drop (see Figure B.4): comparison between analytical values and results from different methodologies. (a) normal to the contact line, $\psi(\phi)$ (note that for methodologies *(ii)* and *(iii)*, the analytical expression was used). (b) Contact angle distribution along the contact line.

For this reason, methodologies *(i)*, *(ii)*, and *(iii)* cannot be used to evaluate the adhesion force of a xy-symmetric drop. Only IBAFA was used for evaluating the forces on the xy-symmetric drop and compared to the analytical values.

For xy-symmetric drop, $F_{x,L/2}$ was theoretically zero as the drop is symmetric with respect to the y-axis: IBAFA evaluates it correctly, with negligible error (in the order of 10^{-4}). The results for $F_{y,L/2}$ show that IBAFA can evaluate the force with a small error (-0.30%) when compared to the analytical value.

x-symmetric drop

Considering the case of a drop subject to an external force, such as gravity, the x-symmetric drop case is more interesting than the previous one, as it is more representative of a distorted drop subjected to an external force.

For a x-symmetric drop, both $F_{x,L/2}$ and $F_{y,L/2}$ are of interest, as they

Table B.3: Adhesion forces obtained with the methodologies described in Table B.1 for the x-symmetric synthetic drop. The distribution of the normal $\psi(\phi)$ and of the contact angle $\theta(\phi)$ along the contact line is shown in Figure B.12. Forces have been calculated on half of the contact line, $L/2$, and were normalized with respect to γ.

methodology	$F_{x,L/2}/\gamma$	$e_x[\%]$	$F_{y,L/2}/\gamma$	$e_y[\%]$
analytical	1.370	-	1.125	-
methodology *(i)*	2.418	76.50	0.468	-58.40
methodology *(ii)*	1.321	-3.56	0.598	-46.86
methodology *(iii)*	1.546	12.86	0.598	-46.86
IBAFA	1.369	-0.10	1.125	0.03

are both non-zero (over half of the contact line). Table B.3 shows the results obtained with the four methodologies, and Figure B.12 illustrates the distribution of $\psi(\phi)$ and $\theta(\phi)$. As for the xy-symmetric shape, IBAFA results are in very good agreement with the analytical ones, since the errors are lower than 0.1% for both force components. On the other hand, the methodology *(i)* evaluates the force inadequately, with an error of 76.5% for $F_{x,L/2}$. The other two methods, *(ii)* and *(iii)*, provide results with low accuracy (see Table B.3). The results in terms of $F_{y,L/2}$ are poorer, since the evaluated force is the half as the analytical value. It should be noted that methodologies *(ii)* and *(iii)* were taken from [88] and [89], for which $F_{y,L/2}$ may not have been relevant. In fact, they were more concerned with the evaluation of the force in the x-direction, i.e. the direction of the gravity component along the surface. However, the error of the evaluated adhesion force is a direct consequence of an inaccurate description of the contact angle distribution along the contact line, regardless of x- or y-direction.

The reason for the low accuracy of methodology *(iii)* may be due to its range of applicability. In [89], where this methodology is taken from, it is shown that the third degree polynomial interpolation represents well the contact angle distribution along the contact line for a case with small difference between the maximum and minimum contact angle

($\theta_{max} - \theta_{min} \approx 15°$). Also, it is reported that the maximum analyzed contact angle hysteresis, $\theta_A - \theta_R$, is 51°, but no value is reported for the maximum analyzed $\theta_{max} - \theta_{min}$. Thus, the methodology may not apply to this case, where $\theta_{max} - \theta_{min} \approx 100°$. On the contrary, IBAFA is shown to work for both small and large differences between θ_{min} and θ_{max}.

The errors obtained using methodologies *(ii)* and *(iii)* provide an estimation of the error, when the assumed contact angle distribution does not represent the actual contact angle distribution adequately. Note that in methodology *(ii)* the contact angle distribution is also arbitrarily selected, irrespective of the Young-Laplace equation. With regards to methodology *(iii)*, the assumed contact angle distribution (3^rd order polynomial) has been proposed to fit experimental data, but does not necessarily satisfy the Young-Laplace equation, as well; it has been just a convenient model for a particular system. Thus, the assumed contact angle distribution may not apply to a generic drop. The effective error with experimental drops will strongly depend on the system studied, i.e. for some liquid/surface combination the methodologies may work well, for some others they may not. Regarding the latter point one needs to consider that methodologies *(ii)* and *(iii)* use an elliptical contact line and thus can describe the contact line of the proposed synthetic drop accurately, since this is also an ellipse. For a generic experimental drop the contact line may significantly differ from an ellipse (see Figure B.2), and the reported error may even increase further.

As a reference, the value of the fitting parameter k in Equation B.3 was derived for the x-symmetric drop. Using the analytical value of the force, the adjustable parameter k takes the value 1.18. As a reference length, an equivalent radius was used, i.e. the radius of the circle with the same area as the contact surface.

The accuracy, by which the adhesion force is evaluated using IBAFA, allows its application to other problems. For example, determination of interfacial tension from tilt plate experiments. Consider a stationary drop on a tilted surface, with a known mass. The gravity force is derived from the surface inclination and the mass. Since at the equilibrium condition the adhesion force is equal to the component of the gravity force along the surface, the liquid surface tension can be obtained using the inverse of procedure for IBAFA.

B.7 Conclusions

In this paper, a detailed description of a new methodology, IBAFA, for evaluating the adhesion force of a drop on a surface, subjected to an external force, is given. The methodology is based on the use of multiple profile images of a drop. The images are used to accurately reconstruct both the contact line shape and the contact angle distribution along the contact line. A general representation of the contact line shape is given by the use of the Fourier cosine series representation. Furthermore, the current formulation for the calculation of the adhesion force for drops with non-circular contact line currently presented in literature is discussed and corrected.

The generality of the approach allows the methodology to be particularly suitable for the analysis of drops with highly “irregular” shapes, such as those encountered in industrial applications, where surfaces with anisotropic topography may be often involved.

The contact line shape reconstruction procedure was validated both with actual experiments and simulated experiments. The procedure for the calculation of the adhesion force was tested using simulated experiments with synthetic drops of known shapes.

One of the critical issues, connected to the use of multiple profile images, was perspective error. The Fourier series representation provides the required mathematical formulation for correcting it. Perspective error plays instead no role in measurement of the contact angles from the profile images.

The results for the drop adhesion force demonstrated the capability of IBAFA to evaluate the adhesion force due to surface forces correctly, with a small error, generally in the order of 1%, when compared to the analytical results. This good agreement is a direct consequence of the capability of the new methodology to reconstruct the contact line shape and the contact angle distribution accurately, and to correct the perspective error.

Different methodologies available in literature [88, 89, 92] were also implemented, to provide the reader an estimation of the error, when simplifying assumptions, e.g. circular and elliptical contact line, are invoked. The methodology from [92] provides results with a magnitude of the error in the order of 100%. The methodology from [88] and [89] leads to an error in the evaluation of the force up to 50%.

Appendix C

Drop impact at high-speed: a preliminary study

In this Appendix we present a preliminary study of millimetric or sub-millimetric drop impacts at high speed, up to $V = 10m/s$, with Weber numbers in the range $60 < We < 1800$. Aim of the study was to extend the range of impact conditions of tests, presented in Part II (where $We < 680$). Achieving high speed impact conditions impact conditions was made possible by use of an AirFlow Drop Generator (AFDG) developed by the research group of CSI (Center of Smart Interfaces) at University of Darmstadt. The novel generator allows to generate smaller drops (down to $D_0 = 0.7$mm) and achieve high impact speed compared to traditional falling drop system (as those described in Part II of the thesis). Experimental results were compared to correlations and models in literature for estimating drop spreading and eventually drop rebound, if this occurred, in a wide range of We numbers.

Due to limitations of the available high speed camera system (as discussed in Section C.2), the accuracy of the study was not sufficient to include the results in the thesis main body. Nonetheless, processed images provide some useful information, that deserved to be reported here.

C.1 Methods and Materials

The drop impact apparatus consists of: (i) ADFG, for drop generation; (ii) a high speed camera, to record drop impacts, with a floodlight to provide adequate back lighting; and (iii) a set of surfaces with variable wettability.

C.1.1 AirFlow Drop Generator (ADFG)

The peculiarity of the AFDG is the presence of two nozzle, concentric with respect to the needle, where drop is generated[1]. Airflow in the two nozzles has a double benefit: first, airflow in the internal nozzle allows to generate smaller drops, because drag aerodynamic forces co-operate with gravity force to overcome adhesion forces and to detach smaller drops from the needle tip; second, both airflows in the internal and in the external nozzles contribute in accelerating the drop to higher speed than in the case of drop free fall. The airflow drop generator is a compact device (25x20x10cm). Beside the two concentric nozzles, the hardware consists of an electronic board for control and a PC interface. Airflows (primary stream, PS, and secondary stream, SS) can be controlled independently in each nozzle to adjust drop diameter and velocity. The procedure for drop generation is the following: (1) a drop is generated at the tip of the needle (for present study: Hamilton Gauge30, external diameter 0.31mm); the liquid (water) is dispensed manually using a 25µl Hamilton syringe; (2) airflow of primary and/or the secondary stream is activated, according to the airflow intensity set value; (3) a triggering signal activate camera recording, short after airflow activation.

C.1.2 Image recording system

A pco1200hs high speed camera was used, as described in Section 5.1.4. Drop impact images were registered with a resolution of 47ppm (pixel per millimeter), i.e. 21µm/pixel; frame rate was varied from 7000 to 15000fps.

---

[1] No images of the drop generator were included, since it is currently undergoing a patent examination

In the latter case (15000fps) a window of 1280 × 30pixel can be observed, which corresponds to 27 × 0.6mm. Back light illumination of the drop impact region is provided by a 1kW (96000 lumen) floodlight, which allows to reduce exposure time down to $20 - 30$µs.

C.1.3 Surface Preparation

Drop impact tests were performed on five surfaces: (i) smooth glass; (ii) PMMA; (iii) Teflon; (iv) SHS-Teflon; (v) SHS-Zonyl-a (see Section 5.2 for details on surface preparation and Table 5.1 for surface characteristics).

C.2 Issues on high-speed recording

Preliminary tests with the AFDG have shown that there are two critical issues to consider, to create a valuable drop impact database: drop repeatability, in terms of both diameter and impact speed, and spatial/temporal resolution (or equivalently dimension of the observation window). Drop repeatability is a severe issue. Although a high precision syringe was used for liquid dispensation, the accuracy was of the order of 0.25μl, leading to poor drop diameter reproducibility for smaller drops (±6% for a 2mm drop, ±48% for a 1mm drop); also, variation of drop diameter has a direct consequence on drag forces, and thus on drop acceleration and on impact velocity. Preliminary tests have shown there is a non-negligible variation of all drop parameters, which makes drop impact tests non-repeatable, if compared to standard free falling drop, where repeatability of drop impact diameter and velocity is usually very high (see Section 6.1). Test high repeatability usually allows to split the recording procedure for free falling drops into two steps: (1) videos are recorded at relatively low frame rate (in the order of 1000fps) using a wide observation window in order to measure drop impact conditions, i.e. D_0, V and non-dimensional numbers; (3) videos are then repeated at high frame rate (in the order of $10000 - 20000$fps) observing a very narrow area, close to the impact area, to measure time evolution of constact diameter, $D(t)$ (and its non-dimensional form, the spread factor, $\xi(t) = D(t)/D_0$). When impact conditions are non-reproducible, as for tests with AFDG, the recording procedure cannot be separated into two steps and impact conditions have to be measured for each impact. This opens an issue related to finding the optimum compromise between fps (i.e. time resolution), spatial resolution and size of the observation window.

Considering for example a frame rate 15000fps and resolution of 47ppm, the resulting observation window height is 0.5mm (using the available pco-1200hs high speed camera with a 105mm macro lens). This implies that a millimetric drop cannot be observed entirely before impact and the diameter has to be reconstructed from partial view of the drop; also, since at least 2 images of the drop before impact have to be recorded for evaluating impact speed, there is an upper limit for automatic measurement of velocity which is 3.75m/s (=0.25mm/0.066ms). In practice, manual image analysis allows to double this limit to 7.5m/s or even slightly higher (10m/s), but with a significant deterioration of measurement accuracy.

All the above mentioned critical issues affect the measurement accuracy. Nevertheless, they do not compromise the interest in the present work, which is a preliminary study aimed at understanding new phenomena related to high speed drop impact.

C.3 Experimental conditions

The following four impact datasets, with corresponding average drop diameter, D_0, and impact speed, V, were obtained:

1. dataset A: $D_0 \approx 1.5$mm and $V \approx 3$m/s;

2. dataset B: $D_0 \approx 1.5$mm and $V \approx 6$m/s;

3. dataset C: $D_0 \approx 1.0$mm and $V \approx 8$m/s;

4. dataset D: $D_0 \approx 2.2$mm and $V \approx 6$m/s;

C.4 Comparison with available correlations

Values of drop maximum spread spread factor, ξ_{max}, and rebound time, $t_{rebound}$ (in case the drop rebounds), have been measured from impact image videos and compared to correlations in literature. Experimental data for hydrophilic surfaces were compared to correlations proposed by Scheller and Bousfield [45] (see Equation 4.11), and by Roisman [51] (see Equation 4.12). Exdperimental data for SHS were compared with the correlation by Clanet *et al.* [54] (see Equation 4.13). Drop rebound time was compared with correlation proposed by Clanet *et al.* [54] (see Equation4.10).

C.5 Results and Discussion

C.5.1 Dataset A

For dataset A, average values are: $D_0 \approx 1.5$m and $V \approx 3$m/s, $We \approx 200$ and $Oh \approx 0.0026$. The repeatability of impact conditions for dataset A is good. Figure C.1 illustrates a comparison between experimental results on maximum spreading and Roisman semi-empirical correlation. The correlation of data is good for all surfaces. The are no significant variations between surfaces. This result is consistent with what was shown in Chapter 6, where we identified a high Weber regime, in which maximum spread factor is not influenced by surface wettability. Note that the correlation also works well for a 400µm drop ($V = 3.2m/s$, $We = 57$), that was accidentally generated during one test. Correlation from Scheller and Bousfield [45] also provides good results, and has not reported, being very similar to Figure C.1. Figure C.2 shows that Clanet correlation for SHS underestimates ξ_{max} on SHS-Teflon, as already observed in Chapter 6.

Note that SHS-Zonyl-a data are missing in Figure C.1 and C.2. This lack is due the impossibility to measure a maximum diameter for drop impacting on SHS-Zonyl-a. When drop impacts, high fragmentation of the drop is occurs at the first stages. Thus, it is impossible to identify a rim and to follow time evolution of drop contact diameter unambiguously. Figure C.3 and C.4 show frames from drop impact on SHS-Teflon and SHS-Zonyl-

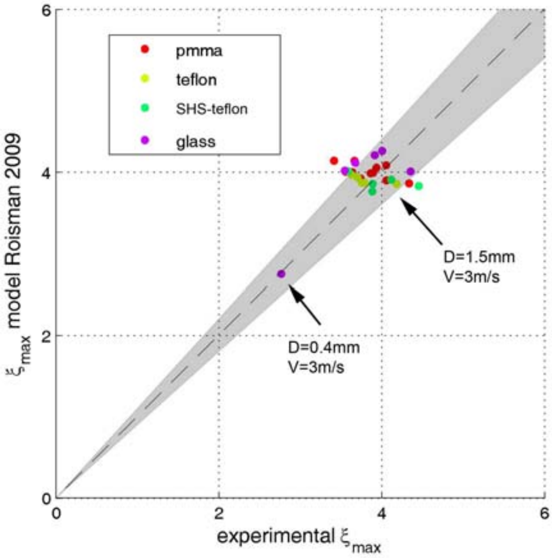

Figure C.1: Comparison between experimentally measured maximum spread factor and Roisman correlation [51] for different surfaces (dataset A). Shadowed areas identify deviations within ±10%.

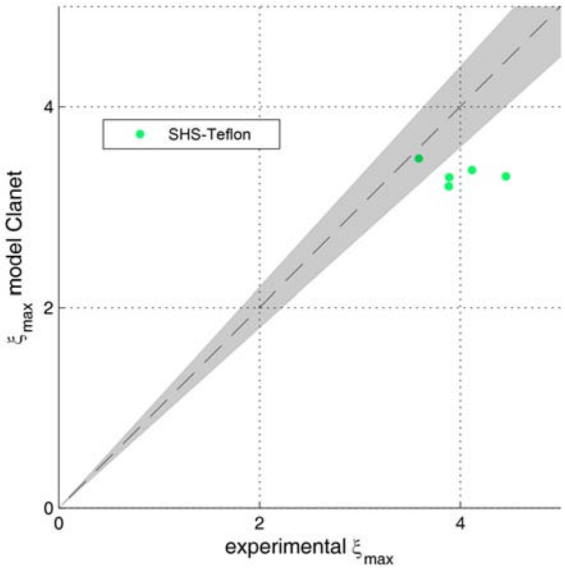

Figure C.2: Comparison between experimentally measured maximum spread factor and Clanet *et al.* correlation [51] for SHS-Teflon (dataset A). Shadowed areas identify deviations within ±10%.

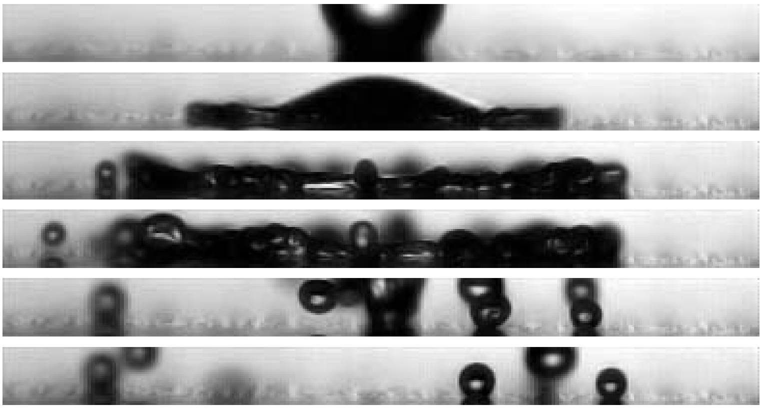

Figure C.3: Image sequence of water drop impact on SHS-Teflon, $V = 2.9$m/s, $D_0 = 1.4$mm, $We = 161$, $t_{conv} = 0.48$ms (dataset A). Frame sequence time is: 0, 0.4, 1.1, 1.8, 5.0, 19.6 [ms].

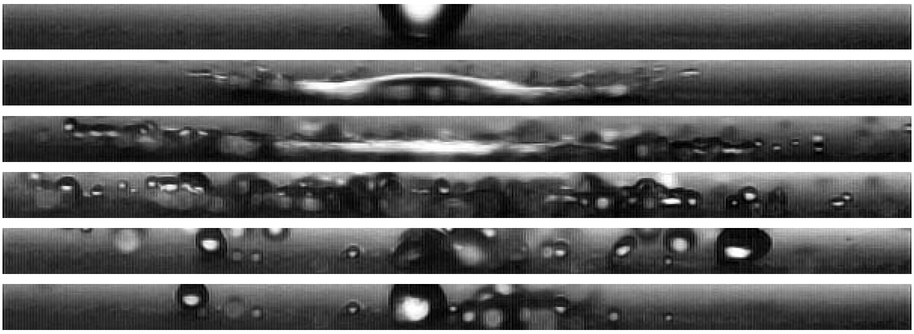

Figure C.4: Image sequence of water drop impact on SHS-Zonyl-a, $V = 4$m/s, $D_0 = 1.4$mm, $We = 306$, $t_{conv} = 0.35$ms (dataset A). Frame sequence time is: 0, 0.4, 1.1, 1.8, 5.0, 19.6 [ms].

a, resprectively, from database A. On SHS-Teflon, liquid/air interface can be clearly detected during spreading, rim can be identified, and so contact diameter, D; at the end of spreading, rim instability causes formation of secondary drops, but the drop core recoils and rebound of the drop core occurs at $t = 6.0$ms. On SHS-Zonyl-a, drop splash and fragmentation into secondary drops occur; rim cannot be identified and it is impossible to detect clearly when spreading stops; there is only a partial recoiling, which is given by merging of small drops in the area around the impact point. On SHS-Zonyl-a no rebound can be observed and the central drop appear to have less mobility then secondary drops (as proved by subsequent manual surface tilting); reduced mobility suggests a transition from Cassie-Baxter to Wenzel wetting state. This transition occurs when air pockets, that exist between liquid and solid surface to give superhydrophobicity, collapse and the liquid completely wets the surface. With regards to rebound time on SHS-Teflon, a good agreement was found between experimental data ($t_{rebound} = 5.9 \pm 0.2$ms) and Clanet *et al.* correlation, which predicts $t_{rebound} = 5.8$ms for $D_0 = 1.4$mm and $t_{rebound} = 6.4$ms for $D_0 = 1.5$mm.

C.5.2 Dataset B

For dataset B, The average diameter is $D_0 = 1.5$mm, whereas impact speed is approximately $V = 6$m/s . However, in this case higher uncertainties affect measurement of both shape (because drops are far from being spherical) and velocity, which exceeds the limit of maximum speed that can be automatically measured (see Section C.2). Also, reproducibility of impact conditions is low. For this reason, the We range is wide: $600 < We < 1300$. For dataset B, the correlation between experimental results and Roisman correlation is poor, as one can see from Figure C.5. Only few points lie in the close to the bisector line; most of the points lie on the right of the bisector line, meaning that Roisman correlation underestimate drop maximum spreading. Also, data appear more disperse than for dataset A (Figure 2a). If data scattering can be explained by low accuracy in measurement of impacting drop diameter and velocity, the reason why most of the points in Figure C.5 lies at the right side of the bisector line has to be explained. A

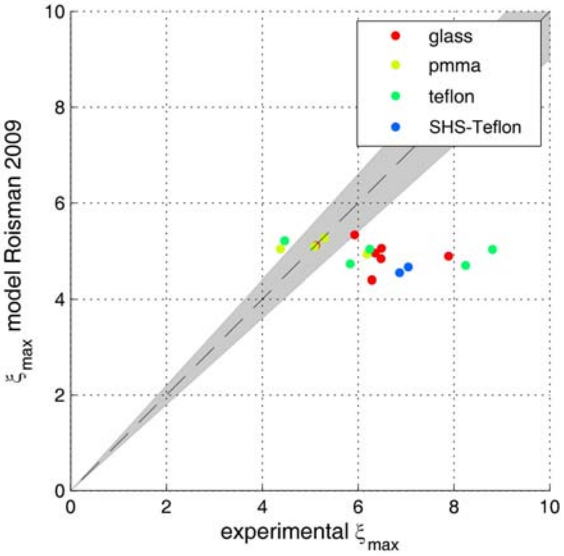

Figure C.5: Comparison between experimentally measured maximum spread factor and Roisman correlation [51] (dataset B). Shadowed areas identify deviations within ±10%.

possible reason is the increased air stream velocity (compared to air stream intensity of dataset A). For dataset B experiments, secondary air stream was activated (for database A experiments secondary air stream was off) to achieve higher drop acceleration and thus higher impact speed. Increased air stream intensity probably has an effect in "back-pushing" the drop on the surface during the spreading phase, thus enhancing drop spreading. As such, maximum spread factor is higher compared to case of drop impact in still air, for which Roisman correlation was derived.

Despite the increase of drop impact velocity, drop rebound time on SHS-Teflon does not change remarkably ($t_{rebound} = 5.1 \pm 1.1$ms), suggesting that rebound time only depends on drop size, as found by Clanet *et al.* [54] and confirmed by our previous experiments with $D_0 = 3$mm drops. For one impact only there is a sensible reduction of rebound time (3.39ms). The impression looking at the image sequence is that the final stages of recoiling (before rebound occurs) are accelerated by the presence of airflow, which cleans up the surface from water drops and thus anticipates water rebound. This phenomena is of course of clear interest for potential application of SHS to mitigate icing on aerodynamic surfaces: the presence of a boundary layer may anticipate drop shedding, allowing liquid water removal before freezing.

C.5.3 Dataset C

For dataset C, diameter was decreased, to have an average drop diameter of $D_0 = 1$mm. Repeatability of diameters is good, but it was low for velocities. Also, velocity measurements were a severe issue for this dataset, since velocity range was $7 < V < 11$m/s. The We numbers range ($600 < We < 1800$) s comparable with the We range of dataset B ($600 < We < 1300$).

Figure C.6 illustrates the relationship between experimental data and Roisman correlation. The correlation is not good, because many points are far from bisector line. Nevertheless, for dataset C points are scattered symmetrically with respect to bisector line. The situation is thus different from dataset B, where data were not only scattered, but also not centered

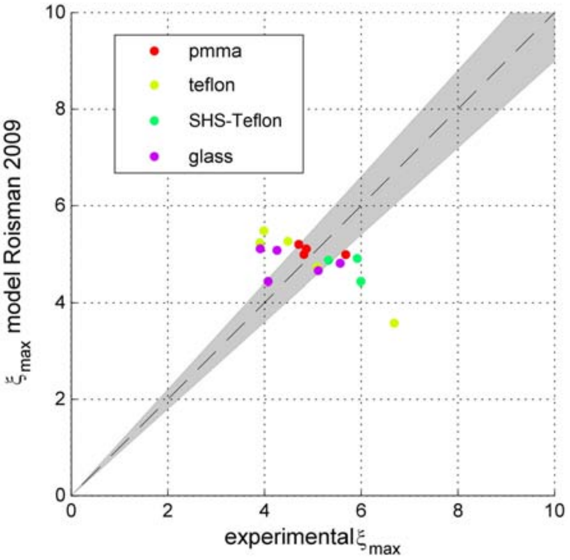

Figure C.6: Comparison between experimentally measured maximum spread factor and Roisman correlation [51] (Dataset C). Shadowed areas identify deviations within ±10%.

around the bisector line.

It is noticeable that, despite dataset B and C are characterized by similar We, results are really different. An explanation may be found again in the effect of the airflow. In dataset B, drops were bigger (1.5 times drops in dataset C considering diameter, i.e. $1.5^3 = 5$ times bigger considering mass) and more intensive air stream was necessary for accelerating drops up to 6m/s. For dataset C, drops are much smaller and can thus be accelerated with a reduced air stream intensity up to 11m/s. Therefore, aerodynamic forces in dataset C are lower and have no effect in enhancing the spreading, as it was for dataset B.

With regards to data dispersion, the reason is most likely the poor of accuracy for V measurements. Inaccurate measurement of velocity leads to a wrong estimation of We and Re number, that are used in Roisman correlation to estimate maximum spread factor, ξ_{max}. Drop rebound is observed only on SHS-Teflon. Experimental rebound time, $t_{rebound} = 3.1 \pm 1.1$ms, is close to the value calculated with relationship proposed by Clanet *et al.* (3.0ms for $D_0 = 0.9$mm and 3.5ms for $D_0 = 1$mm).

C.5.4 Dataset D

For dataset D, drops with an average diameter of $D_0 = 2.2$mm were generated, impact velocity was approximately $V \approx 6$m/s, and We numbers were in the range $900 < We < 1700$.

Results on maximum spreading are illustrated in Figure C.7. Data are, as for dataset C, rather scattered, but distribution is symmetrical to bisector line.

This result might appear surprising in light of what was observed for dataset B. For dataset B data were shifted to the right of the bisector line, probably due to aerodynamic forces that enhanced spreading. For dataset D higher air stream intensity was used (bigger drops than for dataset B were accelerated up to the same speed), but aerodynamic forces do not seem to play any role on drop maximum spreading. However, the distance between the nozzle and the surface was increased for dataset D, thus reducing the total pressure at the stagnation point (which approximately correspond

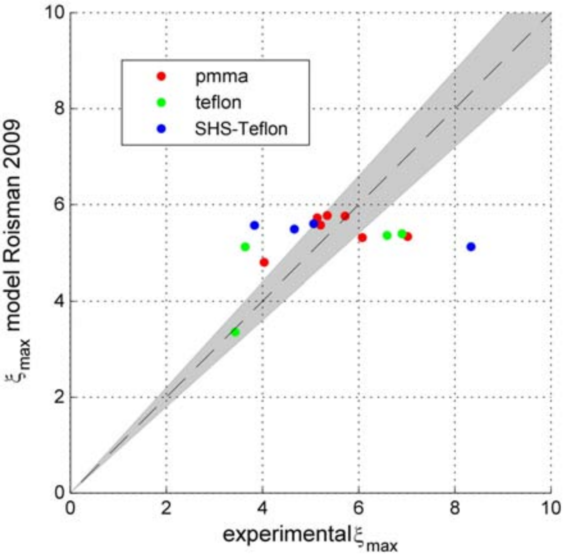

Figure C.7: Comparison between experimentally measured maximum spread factor and Roismanf correlation [51] (Dataset D). Shadowed areas identify deviations within ±10%.

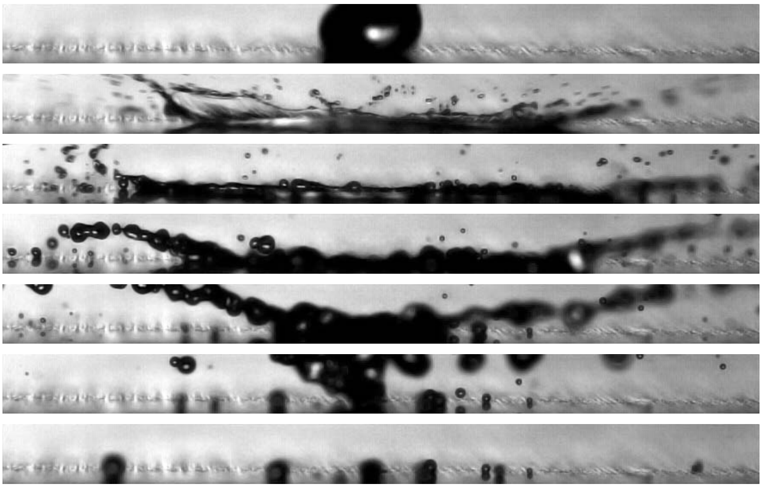

Figure C.8: Image sequence of water drop impact on SHS-Teflon, $V = 6.4$m/s, $D_0 = 2.45$mm, $We = 1390$, $t_{conv} = 0.38$ms (dataset D). Frame sequence time is: 0, 0.6, 1.4, 2.7, 3.9, 5.6, 16.5 [ms]. Drop spreading stops at $t = 2$ms.

to drop impact point). Increasing the nozzle/surface distance gave more problems in terms of drop impact locations (deviations of drop impact point from the focus plane), but was beneficial for reducing influence of aerodynamic forces during spreading.

An important factor in this dataset is the drop shape. Being drop bigger, at high velocities drop are no longer spherical, but more similar to ellipses. A qualitative observation was possible. Consider two drops with the same mass and elliptical shape, the first with vertical axis longer than the horizontal axis, and vice versa for the second drop; the first drop spreading will be higher than for the second drop. It was not possible to measure this effect, but it can help understanding data dispersion (together with inaccurate velocity measurement).

An unexpected results was obtained with rebound time. Experimentally measured times, $t_{rebound} = 6.3 \pm 0.9$ms) are considerably lower than predicted by Clanet *et al.* [54] (14ms for a $D_0 = 2.5$mm, that is the average

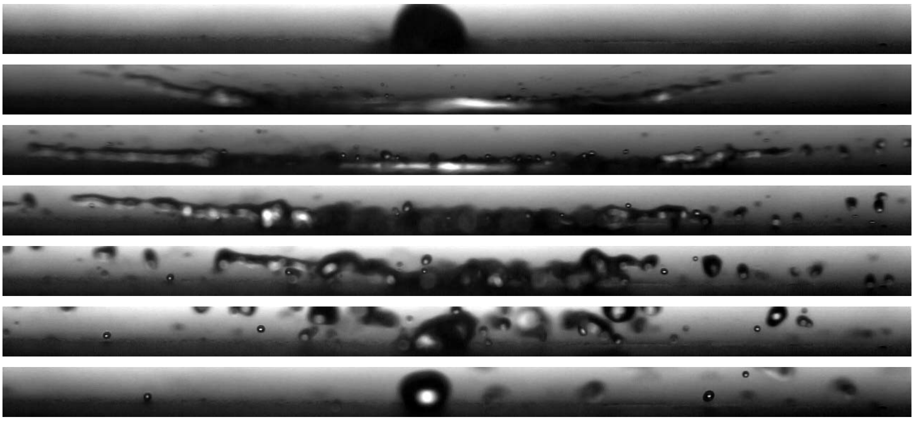

Figure C.9: Image sequence of water drop impact on SHS-Zonyl-a, $V = 7.3$m/s, $D_0 = 2.25$mm, $We = 1320$, $t_{conv} = 0.31$ms (dataset D). Frame sequence time is: 0, 0.6, 1.4, 2.7, 3.9, 5.6, 16.5 [ms].

drop diameter for impact on SHS-Teflon). Figure C.8 illustrates a frame sequence from a drop impact on SHS-Teflon. It can be observed that, when drop spreading stops (at $t \approx 2.0$ms), there is a contemporaneous recoil and lift of the drop rim, which anticipates the drop core lift from the surface. This phenomenon is new and has never been observed, neither for 3mm drops, nor in the other dataset of the present study (rim usually recoils, sliding on the surface, and subsequently drop rebounds). It is possible that aerodynamic forces, related to the presence of a boundary layer close to the air stream stagnation point, play a role in enhancing drop lift during recoiling phase. In Figure C.8 the image sequence of a drop impact on SHS-Zonyl-a is illustrated. Images show that there is practically no recoil of the drop. Secondary drops are ejected with high velocity from the crown in the initial stages or blown away by air stream, whereas the drop core remains at the impact point without rebounding. Once again the transition from Cassie-Baxter to Wenzel wetting state may be the cause for drop rebound inhibition.

C.6 Conclusions

In the present study, an innovative AirFlow Drop Generator (AFDG) was used to study effect of wettability on water drop impact at high impact energy, ip to $We = 1800$. Tests have shown the very good potentiality of the AirFlow Drop Generator for drop impact studies, which allows to extend the limitation of standard falling drop experiments.

Results on drop maximum spreading, ξ_{max}, demonstrated that there is no significant difference in spreading between surfaces with variable wettability, as was already shown in Chapter 5. Roisman correlation [51] for prediction of maximum spread factor, ξ_{max}, appears to have good correlation with experimental data in a wide range of We numbers (from 60 to 1800) and drop diameters (300μm$< D_0 <$ 2.5mm). Data scattering (as in dataset C and D) has to be probably attributed to the inaccuracy in measurement of drop impact conditions (D, V, drop eccentricity) for high speed drops, due to camera recording speed limitations. Only in one case, dataset B, poor correlation was found between experiments and Roisman correlation, likely due to aerodynamic effects. Clanet *et al.* correlation [54] for prediction of maximum spreading on SHS underestimates spreading in the entire investigated We range.

Clanet *et al.* correlation for drop rebound time on SHS was proofed to fit well with experimentally measured values in dataset A, B, C; data confirmed that drop rebound time scales only with drop dimension and not with impact velocity. Nevertheless, Clanet *et al.* correlation unexpectedly did not fit well with experimental rebound time measured for dataset D, for which experimental rebound time is half than predicted. Once again, it is possible that aerodynamic forces play a role, in this case by enhancing drop lift-up during the receding phase. This phenomena is of course of clear interest for potential application of SHS to mitigate icing on aerodynamic surfaces: the presence of a boundary layer may anticipate drop shedding, allowing liquid water removal before freezing.

Results on the two tested SHS, SHS-Teflon and SHS-Zonyl-a, are qualitatively different. A strong drop fragmentation on SHS-Zonyl-a was observed after impact, which makes it difficult, if not impossible, to determine the evolution of the contact diameter. Also, recoiling of the drop on SHS-Zonyl-a is poor or absent; the drop core does not rebound, but stays stuck at the impact point. A likely explanation is that, at high Weber numbers, transition from Cassie-Baxter to Wenzel state occurs and superhydrophobicity degrades. More tests are needed on SHS-Teflon and SHS-Zonyl-a to understand why differences exists and which other parameters, related to surface morphology, can explain different drop impact outcomes.

Few weak points of the drop generator have been identified and could be easily solved. For example, better repeatability of drop impact conditions would considerably facilitate data analysis and results interpretation. An automatic drop dispenser should be integrated to allow precise drop liquid dispensation.

With respect to video recording, more performing high speed camera, in terms of recording speed (frame rate), light sensitivity, and possibly higher resolution is required. Such a camera would allow more accurate measurements of impact conditions, drop deformation, and characteristic times.

Bibliography

[1] I. Paraschivoiu and F. Saeed. Aircraft Icing. `http://www.meca.polymtl.ca/ion/000-main.pdf` (last access: Dec. 2009).

[2] R.M. Rasmussen, C.G. Wade, R.K. Moore, A. Davis, and D. Fleming. A new Ground Deicing Hazard Associated with Freezing Drizzle Ingestion by Jet Engines during taxi. In *Proc. of 11th Conf. on Aeronautics and Aerospace*, 2004.

[3] A. Heinrich, R. Ross, G. Zumwalt, J. Provorse, V. Padmanabhan, J. Thompson, and J. Riley. *Aircraft Icing Handbook, vol. 1 of 3.* FAA Technical Center, 1991.

[4] A. Heinrich, R. Ross, G. Zumwalt, J. Provorse, V. Padmanabhan, J. Thompson, and J. Riley. *Aircraft Icing Handbook, vol. 3 of 3.* FAA Technical Center, 1991.

[5] K.M. Al-Khalil, T.G. Keith, K.J. De Witt Jr., J.K. Nathman, and D.A. Dietrich. Thermal Analysis of Engine Inlet Anti-Icing Systems. *American Institute of Aeronautics and Astronautics*, AAIA 89-0759:9, Jan. 1989. Presented at 27th Aerospace Sciences Meeting & Exhibit, Reno, Nevada, 1989.

[6] S.J.M. Cabler. *Aircraft Ice Protection 20-73A*. Federal Aviation Administration, Aug. 2006.

[7] I. Langmuir and K.B. Blodgett. A Mathematical Investigation ofWater Droplet Trajectories. Technical Report 5418, Army Air Forces, Feb. 1946.

[8] M. B. Bragg. A similarity analysis of the droplet trajectory equation. *AIAA Journal*, 20:1681–1686, Dec. 1982.

[9] B.L. Messinger. Equilibrium temperature of an unheated icing surface as a function of air speed. *Journal of the Aeronautical Sciences*, 20(1):29–42, 1953.

[10] C.D. MacArthur. Numerical simulation of airfoil ice accretion. *AAIA*, Aerospace Sciences Meeting, 21st, Reno, NV, 1983.

[11] K.M. Al-Khalil. New Concept in Runback Water Modeling of Anti-Iced Aircraft Surfaces. *J. Aircraft*, 30(1), 1993.

[12] K.M. Al-Khalil and T.G. Keith. Development of an improved model for runback water on aircraft surfaces. *J. Aircraft*, 31(2):271–278, 1994.

[13] P. Louchez, G. Fortin, G. Mingione, and V. Brandi. Beads and rivulets modelling in ice accretion on a wing. *AAIA*, 98(0489):10, Jan. 1998. 36th Aerospace Sciences Meeting & Exhibit, Reno, NV, 1998.

[14] G. Fortin, J.L. Laforte, and A. Beisswenger. Prediction of ice shapes on NACA0012 2D airfoil. *SAE Technical Papers 2003-01*, 2154, 2003.

[15] G. Fortin, A. Ilinca, J.L. Laforte, and V. Brandi. New roughness computation method and geometric accretion model for airfoil icing. *J. Aircraft*, 41(1):119–127, 2004.

[16] G. Croce, E. De Candido, W.G. Habashi, J. Munzar, M.S. Aube, G.S. Baruzzi, and C. Aliaga. FENSAP-ICE: Analytical Model for Spatial and Temporal Evolution of In-Flight Icing Roughness. *J. Aircraft*, 47(4):1283–1289, 2010.

[17] R.J. Kind, M.G. Potapczuk, A. Feo, C. Golia, and A.D. Shah. Experimental and computational simulation of in-flight icing phenomena. *Prog. Aerosp. Sci.*, 34(5):257–345(89), 1998.

[18] D.N. Anderson. Evaluation of constant-Weber-number scaling for icing tests. volume 96, Jan. 1996. Aerospace Sciences Meeting and Exhibit, 34 th, Reno, NV.

[19] A. Heinrich, R. Ross, G. Zumwalt, J. Provorse, V. Padmanabhan, J. Thompson, and J. Riley. *Aircraft Icing Handbook, vol. 2 of 3.* FAA Technical Center, 1991.

[20] D.N. Anderson and A.D. Reich. Tests of the performance of coatings for low ice adhesion. In *AIAA, Aerospace Sciences Meeting & Exhibit, 35 th, Reno, NV*, 1997.

[21] C. Laforte, J.L. Laforte, and J.C. Carrier. How a Solid Coating Can Reduce the Adhesion of Ice on a Structure. In *Proceedings of the International Workshop on Atmospheric Icing of Structures (IWAIS)*, volume 6, 2002.

[22] R. Menini and M. Farzaneh. Elaboration of Al2O3/PTFE icephobic coatings for protecting aluminum surfaces. *Surf. Coat. Tech.*, 203(14):1941–1946, 2009.

[23] S. Kimura, Y. Yamagishi, A. Sakabe, T. Adachi, and M. Shimanuki. A New Surface Coating for Prevention of Icing on Airfoils. In *SAE Aircraft and Engine Icing International Conference*, 2007.

[24] L. Cao, A. K. Jones, V. K. Sikka, J. Wu, and D. Gao. Anti-icing superhydrophobic coatings. *Langmuir*, 25(21):12444–12448, 2009.

[25] D.L. Loughborough and E.G. Haas. Reduction of the adhesion of ice to de-icer surfaces. *J. Aeronaut. Sci.*, 13(3), 1946.

[26] H.A. Porte and T.E. Nappier. Coating material for prevention of ice and snow accumulations: A literature survey. Technical report, Naval Civil Engineering Laboratory, Port Hueneme, CA, 1963.

[27] P.J. Hearst. Coating material for prevention of ice and snow accumulations: Further Investigations. Technical report, Naval Civil Engineering Laboratory, Port Hueneme, CA, 1964.

[28] Y. Boluk. Adhesion of freezing precipitates to aircraft surfaces. Technical Report TP 12860E, Transport Canada Publication, Nov. 1996.

[29] M.G. Ferrick et al. Evaluation of ice release coatings at cryogenic temperature for the space shuttle. *Cold Reg. Sci. Technol.*, 52(2):224–243, 2008.

[30] J.L. Laforte, M.A. Allaire, and J. Laflamme. State-of-the-art on power line de-icing. *Atmos. Res.*, 46(1-2):143–158, 1998.

[31] A. Nakajima, K. Hashimoto, and T. Watanabe. Recent studies on super-hydrophobic films. *Monats. Chem.*, 132(1):31–41, 2001.

[32] A.G. Kraj and E.L. Bibeau. Icing characteristics and mitigation strategies for wind turbines in cold climates: adhesion force and accumulation amount. In *World Renewable Energy Congress WREC*, Florence, Italy, Aug. 2006.

[33] J.F. Maissan, P. Eng, and Y. Whitehorse. Wind power development in sub-arctic conditions with severe rime icing. *The Northern Review*, 24:174–183, 2001.

[34] D. Quéré. Non-sticking drops. *Rep. Prog. Phys.*, 68(11):2495–2532, 2005.

[35] T. Young. An essay on the cohesion of fluids. *Phil. Trans. R. Soc. Lond.*, 95:65–87, 1805.

[36] R.N. Wenzel. Resistance of Solid Surfaces to Wetting by Water. *Ind. Eng. Chem.*, 28(8):988–994, 1936.

[37] A.B.D. Cassie and S. Baxter. Wettability of porous surfaces. *T. Faraday Soc.*, 40:546–551, 1944.

[38] E. Pierce, FJ Carmona, and A. Amirfazli. Understanding of sliding and contact angle results in tilted plate experiments. *Colloid Surface A*, 323(1-3):73–82, 2008.

[39] L. Gao and T.J. McCarthy. Teflon is hydrophilic. Comments on definitions of hydrophobic, shear versus tensile hydrophobicity, and wettability characterization. *Langmuir*, 24(17):9183–9188, 2008.

[40] A.J.B. Milne and A. Amirfazli. Wetting and Superhydrophobicity. *Langmuir*, 25(24):14155–14164, 2009.

[41] C. Antonini, F.J. Carmona, E. Pierce, M. Marengo, and A. Amirfazli. General Methodology for Evaluating the Adhesion Force of Drops and Bubbles on Solid Surfaces. *Langmuir*, 25(11):6143–6154, 2009.

[42] A.L.N. Moreira, A.S. Moita, and M.R. Panão. Advances and challenges in explaining fuel spray impingement: How much of single droplet impact research is useful? *Progress in Energy and Combustion Science*, 36(5):554–580, 2010.

[43] V. Bergeron, D. Bonn, J.Y. Martin, and L. Vovelle. Controlling droplet deposition with polymer additives. *Nature*, 405(6788):772–775, 2000.

[44] A.L. Yarin. Drop Impact Dynamics: Splashing, Spreading, Receding, Bouncing…. *Annu. Rev. Fluid Mech.*, 38(1):159–192, 2006.

[45] B.L. Scheller and D.W. Bousfield. Newtonian drop impact with a solid surface. *AIChE Journal*, 41(6), 1995.

[46] Š. Šikalo, M. Marengo, C. Tropea, and EN Ganić. Analysis of impact of droplets on horizontal surfaces. *Exp. Therm. Fluid Sci.*, 25(7):503–510, 2002.

[47] R. Rioboo, M. Marengo, and C. Tropea. Time evolution of liquid drop impact onto solid, dry surfaces. *Exp. Fluids*, 33(1):112–124, 2002.

[48] J. Fukai, Y. Shiiba, T. Yamamoto, O. Miyatake, D. Poulikakos, CM Megaridis, and Z. Zhao. Wetting effects on the spreading of a liquid droplet colliding with a flat surface: Experiment and modeling. *Phys. Fluids*, 7:236, 1995.

[49] M. Pasandideh-Fard, S. Chandra, and J. Mostaghimi. A three-dimensional model of droplet impact and solidification. *Int. J. Heat Mass Tran.*, 45(11):2229–2242, 2002.

[50] I.V. Roisman, E. Berberović, and C. Tropea. Inertia dominated drop collisions. I. On the universal flow in the lamella. *Phys. Fluids*, 21:052103, 2009.

[51] I.V. Roisman. Inertia dominated drop collisions. II. An analytical solution of the Navier–Stokes equations for a spreading viscous film. *Phys. Fluids*, 21:052104, 2009.

[52] T. Mao, D.C.S. Kuhn, and H. Tran. Spread and rebound of liquid droplets upon impact on flat surfaces. *AIChE Journal*, 43(9):2169–2179, 1997.

[53] D. Richard, C. Clanet, and D. Quéré. Surface phenomena: Contact time of a bouncing drop. *Nature*, 417(6891):811, 2002.

[54] C. Clanet, C. Béguin, D. Richard, and D. Quéré. Maximal deformation of an impacting drop. *J. Fluid Mech.*, 517:199–208, 2004.

[55] D. Bartolo, C. Josserand, and D. Bonn. Retraction dynamics of aqueous drops upon impact on non-wetting surfaces. *J. Fluid Mech.*, 545:329–338, 2005.

[56] A.L. Biance, F. Chevy, C. Clanet, G. Lagubeau, and D. Quéré. On the elasticity of an inertial liquid shock. *J. Fluid Mech.*, 554:47–66, 2006.

[57] R. Rioboo, M. Voué, A. Vaillant, and J. De Coninck. Drop Impact on Porous Superhydrophobic Polymer Surfaces. *Langmuir*, 24(24):14074–14077, 2008.

[58] G.S. Hartley and R.T. Brunskill. Reflection of water drop from surfaces. In *Surface Phenomena in Chemistry and Biology*, pages 214–223. Pergamon Press, 1958.

[59] X. Li, X. Ma, and Z. Lan. Dynamic Behavior of the Water Droplet Impact on a Textured Hydrophobic/Superhydrophobic Surface: The Effect of the Remaining Liquid Film Arising on the Pillars' Tops on the Contact Time. *Langmuir*, 26(7):4831–4838, 2010.

[60] M. Pasandideh-Fard, Y.M. Qiao, S. Chandra, and J. Mostaghimi. Capillary effects during droplet impact on a solid surface. *Phys. Fluids*, 8:650, 1996.

[61] H.Y. Kim and J.H. Chun. The recoiling of liquid droplets upon collision with solid surfaces. *Phys. Fluids*, 13:643–659, 2001.

[62] J.P. Delplanque and R.H. Rangel. An improved model for droplet solidification on a flat surface. *J. Mater. Sci.*, 32(6):1519–1530, 1997.

[63] P. Attané, F. Girard, and V. Morin. An energy balance approach of the dynamics of drop impact on a solid surface. *Phys. Fluids*, 19:012101, 2007.

[64] M. Marengo, I.V. Roisman, C. Antonini, and C. Tropea. Drop collisions with complex surfaces. *Curr. Opin. Colloid In.*, Accepted.

[65] C.D. Stow and M.G. Hadfield. An experimental investigation of fluid flow resulting from the impact of a water drop with an unyielding dry surface. *Proc. R. Soc. Lond. A*, 373:419, 1981.

[66] H. Marmanis and S. T. Thoroddsen. Scaling of the fingering pattern of an impacting drop. *Phys. Fluids*, 8(6):1344–1346, 1996.

[67] R. Bhola and S. Chandra. Parameters controlling solidification of molten wax droplets falling on a solid surface. *J. Mater. Sci.*, 34(19):4883–4894, 1999.

[68] R. Dhiman and S. Chandra. Freezing-induced splashing during impact of molten metal droplets with high Weber numbers. *Int. J. Heat Mass Tran.*, 48(25-26):5625–5638, 2005.

[69] A. Bisighini. *Single and Double drop impacts onto deep and thick liquid layers.* PhD thesis, University of Bergamo, 2009.

[70] R. Rioboo, M. Voué, H. Adão, J. Conti, A. Vaillant, D. Seveno, and J. De Coninck. Drop Impact on Soft Surfaces: Beyond the Static Contact Angles. *Langmuir*, 26(7):827–863, 2010.

[71] I.S. Bayer, A. Brown, A. Steele, and E. Loth. Transforming Anaerobic Adhesives into Highly Durable and Abrasion Resistant Superhydrophobic Organoclay Nanocomposite Films: A New Hybrid Spray Adhesive for Tough Superhydrophobicity. *Appl. Phys. Express*, 2(12):5003, 2009.

[72] D. Barona and A. Amirfazli. Producing a superhydrophobic paper and altering its repellency through ink-jet printing. *Lab Chip*, 11:936–940, 2011.

[73] R. Rioboo, C. Tropea, and M. Marengo. Outcomes from a drop impact on solid surfaces. *Atomization Spray*, 11(2):155–166, 2001.

[74] P. Joseph, C. Cottin-Bizonne, J.-M. Benoit, C. Ybert, C. Journet, P. Tabeling, and L. Bocquet. Slippage of water past superhydrophobic carbon nanotube forests in microchannels. *Phys. Rev. Lett.*, 97(15), 2006.

[75] G. McHale, M.I. Newton, and N.J. Shirtcliffe. Immersed superhydrophobic surfaces: Gas exchange, slip and drag reduction properties. *Soft Matter*, 6(4):714–719, 2010.

[76] H.Y. Kim and J.H. Chun. The recoiling of liquid droplets upon collision with solid surfaces. *Phys. Fluids*, 13:643, 2001.

[77] K. Range and F. Feuillebois. Influence of surface roughness on liquid drop impact. *J. Colloid Interf. Sci.*, 203(1):16–30, 1998.

[78] M. Reyssat, A. Pépin, F. Marty, Y. Chen, and D. Quéré. Bouncing transitions on microtextured materials. *Europhys. Lett.*, 74:306–312, 2006.

[79] D. Bartolo, F. Bouamrirene, A. Verneuil, A. Buguin, P. Silberzan, and S. Moulinet. Bouncing or sticky droplets: Impalement transitions on superhydrophobic micropatterned surfaces. *Europhys. Lett.*, 74(2):299–305, 2006.

[80] P. Brunet, F. Lapierre, V. Thomy, Y. Coffinier, and R. Boukherroub. Extreme resistance of superhydrophobic surfaces to impalement: Reversible electrowetting related to the impacting/bouncing drop test. *Langmuir*, 24(19):11203–11208, 2008.

[81] Y.C. Jung and B. Bhushan. Dynamic effects of bouncing water droplets on superhydrophobic surfaces. *Langmuir*, 24(12):6262–6269, 2008.

[82] T. Deng, K.K. Varanasi, M. Hsu, N. Bhate, C. Keimel, J. Stein, and M. Blohm. Nonwetting of impinging droplets on textured surfaces. *Appl. Phys. Lett.*, 94:133109, 2009.

[83] M. Innocenti. Superhydrophobic coating for mitigating icing of airfoils. Master's thesis, University of Bergamo, 2008.

[84] R.A. Brown, F.M. Orr Jr., and L. E. Scriven. Static drop on an inclined plate: analysis by the finite element method. *J. Colloid Interface Sci.*, 73:76–87, 1980.

[85] D. Quéré, M.J. Azzopardi, and L. Delattre. Drops at rest on a tilted plane. *Langmuir*, 14:2213–2216, 1998.

[86] E.B. Dussan V. and R. Tao-Ping Chow. On the ability of drops or bubbles to stick to non-horizontal surfaces of solids. *J. Fluid Mech.*, 137:1–29, 1983.

[87] M. Bouteau, S. Cantin, F. Benhabib, and F. Perrot. Sliding behavior of liquid droplets on tilted Langmuir-Blodgett surfaces. *J. Colloid Interface Sci.*, 317(1):247–254, 2008.

[88] C.W. Extrand and Y. Kumagai. Liquid drops on an inclined plane: the relation between contact angles, drop shape, and retentive force. *J. Colloid Interf. Sci.*, 170(2):515–521, 1995.

[89] A.I. ElSherbini and A.M. Jacobi. Liquid drops on vertical and inclined surfaces:: I. An experimental study of drop geometry. *J. Colloid Interface Sci.*, 273(2):556–565, 2004.

[90] A.I. ElSherbini and A.M. Jacobi. Liquid drops on vertical and inclined surfaces:: II. A method for approximating drop shapes. *J. Colloid Interface Sci.*, 273(2):566–575, 2004.

[91] A.D. Sommers and A.M. Jacobi. Creating micro-scale surface topology to achieve anisotropic wettability on an aluminum surface. *J. Micromech. Microeng.*, 16(8):1571–1578, 2006.

[92] B. Blackmore, D. Li, and J. Gao. Detachment of bubbles in slit microchannels by shearing flow. *J. Colloid Interface Sci.*, 241(2):514–520, 2001.

[93] B. Krasovitski and A. Marmur. Drops down the hill: theoretical study of limiting contact angles and the hysteresis range on a tilted plate. *Langmuir*, 21(9):3881–3885, 2005.

[94] A.D. Sommers and A.M. Jacobi. Wetting phenomena on micro-grooved aluminum surfaces and modeling of the critical droplet size. *J. Colloid Interface Sci.*, 328:402–411, 2008.

[95] P.S. Yadav, P. Bahadur, R. Tadmor, K. Chaurasia, and A. Leh. Drop Retention Force as a Function of Drop Size. *Langmuir*, 24(7):3181–3184, 2008.

[96] E.C. Kumbur, K.V. Sharp, and M.M. Mench. Liquid droplet behavior and instability in a polymer electrolyte fuel cell flow channel. *J. Power Sources*, 161(1):333–345, 2006.

[97] S. Lee and M.B. Bragg. Experimental investigation of simulated large-droplet ice shapes on airfoil aerodynamics. *J. Aircraft*, 36:844–850, 1999.

[98] M. MahéF, M. Vignes-Adler, A. Rousseau, C.G. Jacquin, and P.M. Adler. Adhesion of droplets on a solid Wall and detachment by a shear flow:: I. Pure systems. *J. Colloid Interface Sci.*, 126:314–328, 1988.

[99] A.I. ElSherbini and A.M. Jacobi. Retention forces and contact angles for critical liquid drops on non-horizontal surfaces. *J. Colloid Interface Sci.*, 299(2):841–849, 2006.

[100] J.W. Jennings Jr and N.R. Pallas. An efficient method for the determination of interfacial tensions from drop profiles. *Langmuir*, 4(4):959–967, 1988.

[101] B. Song and J. Springer. Determination of interfacial tension from the profile of a pendant drop using computer-aided image processing: 1. theoretical. *J. Colloid Interface Sci.*, 184(1):64–76, 1996.

[102] A. Amirfazli, J. Graham-Eagle, S. Pennell, and A.W. Neumann. Implementation and examination of a new drop shape analysis algorithm to measure contact angle and surface tension from the diameters of two sessile drops. *Colloid Surface A*, 161(1):63–74, 2000.

[103] W. Li and A. Amirfazli. A thermodynamic approach for determining the contact angle hysteresis for superhydrophobic surfaces. *J. Colloid Interface Sci.*, 292(1):195–201, 2005.

[104] H. Tavana, A. Amirfazli, and A.W. Neumann. Fabrication of superhydrophobic surfaces of n-hexatriacontane. *Langmuir*, 22(13):5556–5559, 2006.

[105] A. Bateni, S.S. Susnar, A. Amirfazli, and A.W. Neumann. A high-accuracy polynomial fitting approach to determine contact angles. *Colloid Surface A*, 219(1-3):215–231, 2003.